SUITABILITY OF LANDSAT IMAGERIES FOR GOLD PROSPECTIVITY IN RAFI LOCAL GOVERNMENT AREA OF NIGER STATE, NIGERIA

BY

ARANSIOLA, Adejoke Blessing
M.Tech/SET/2018/7827

A THESIS SUBMITTED TO THE POSTGRADUATE SCHOOL
FEDERAL UNIVERSITY OF TECHNOLOGY, MINNA, NIGERIA
IN PARTIAL FULFILMENT OF THE REQUIREMENTS FOR THE AWARD OF MASTER OF TECHNOLOGY (MTech) IN SURVEYING AND GEOINFORMATICS

JUNE, 2023

ABSTRACT

Gold prospecting is a significant but capital-intensive source of revenue for developing nations, hence, the need for a fast and less expensive approach for determination of high potential zones prior investment. Remote Sensing (RS) for the identification of hydrothermally altered rocks in examining the response of ratios of some band combinations, adoption of the relationship between lineament and gold mineralization and also, patterns of gold presence especially under simulated environmental condition within the study area has been a challenge. The study provided a means by which RS could be used as s suitable tool for mapping possible precursor of Gold (Au) mineralization in Rafi Local Government Area of Niger state. RS technique was adopted as means for delineating hydrothermal alteration zones for probable precursor of Au mineralization. Such characteristics include rock-outcrops, oxidation, silification, iron oxide and invariably hydrothermal alteration. In the overall, the percentage contribution of each contributory characteristic determined the spatial distribution of the mineral. The study utilised six spectral bands from LandSAT 8 OLI satellite image to compute Principal Component Analysis (PCA), hydrothermally altered rock, Lineament extraction, Sabin's ratio & Kaufmann's ratio and Multi-Criterial Analysis (MCA) for the regions of Iron Oxide, Oxidation and Silification within the study area using the ArcGIS, ENVI and PCI GEOMATICAL softwares. Image processing techniques; band compositing (True colour composite TCC (band 4,3,2) and False colour composite FCC (5,4,3 & 7,5,2), band rationing (Kaufmanns (7/5, 5/4, 6/7) and Sabins (4/2, 6/7, 6/5) ratio as well as Boolean rations (4/2,5/7,7/5,6/5 respectively)) and Principal Component Analysis PCA were applied for the extraction of spectral and spatial information related to lithology, structures and hydrothermal alteration. PCA eigenvalues of 83% for the ratio of Sabin's and 76% for Kaufmann were obtained. These served as a-priori weighting considerations based on the significance factor of the largest band contributor in both indices (Sabins and Kaufmann). Results obtained showed that the variable weight overlay (guided by PCA eigenvalues) was more consistent with the reality of the area than the equal weight overlay and the Multicriteria analysis region for hydrothermal alteration occupying 80% of the area. It was therefore concluded that integration of remote sensing techniques (using the adopted ratios) provided a tool for delineating economic mineralization of Au.

TABLE OF CONTENTS

LIST OF TABLES

LIST OF FIGURES

Figure **Page**

LIST OF ABBREVATIONS

ANN	Artificial Neural Network
ANS	Arabian-Nubian Shield
ASTER	Advanced Spaceborne Thermal Emission and Reflection Radiometer
Au	Gold
B	Blue
BIF	Banded Iron Formations
BR	Band ratio
BRGM	Bureau de Recherches Geologiques et Minieres
CC	Color Composite
Cu	Copper
DEM	Digital Elevation Models
DN	Digital Numbers
EM	Electromagnetic
EMR	Electromagnetic Radiation
EMV	Electromagnetic Wave
ENVI	Environment for Visualising Image
EO	Earth Observation
ERT	Electrical Resistivity Tomography
ETM	Enhanced Thematic Mapper

FCC	False colour composites
FDEM	Frequency-Domain Electromagnetic
FeS_2	Pyrite
FLAASH	Fast-Line of sight Atmospheric Analysis of Spectral Hypercube
G	Green
GEMTIP	Generalized Effective Medium Theory of Induced Polarization
GIS	Geographic Information System
GRAS	Geological Research Authority of Sudan
HPGMS	High-Precision Ground Magnetic Survey
IC	Inductive Coupling
ICA	Independent Component Analysis
IOCG	Iron–Oxide–Copper–Gold
IP	Induced Polarization
k-NN	k-nearest neighbour
LGA	Local Government Area
MIR	Mid Infrared
MLC	Maximum likelihood classification
MNF	Minimum Noise Fraction
MRS	Magnetic Resonance Sounding
MSS	Multispectral Scanner
MT	Magnetotelluric
N	North
NASA	National Aeronautics and Space Administration
NE	NorthEast
Ni	Nikel

NIR	Near Infrared
NW	NorthWest
OLI	Operational Land Imager
PC	Principal Component
PCA	Principal Components Analysis
R	Red
RFC	Random Forest Classifier
ROI	Region of Interest
RS	Remote sensing
S	South
SE	SouthEast
SIP	Spectral Induced Polarization
SVM	Support Vector Machine
SW	SouthWest
SWIR	Shortwave Infrared
TCC	True Colour Composite
TDEM	Time-Domain Electromagnetics
TEM	Transient Electromagnetic
TIRS	Thermal Infrared Sensor
TM	Thematic Mapper
USGS	United States Geological Survey
VMS	Volcanogenic Massive Sulphide
VNIR	Visible Near-infrared
Zn	Zinc

CHAPTER ONE

1.0 INTRODUCTION

1.1 Background to the Study

Remote sensing (RS) of the earth, or earth observation (EO), being the science of identifying features of the earth surface and their properties of biophysical and geophysical estimation using radiation from electromagnetic, being measured by spaceborne sensors (shuttles of space and satellites) or aircraft (airborne) or platforms (Agar and Coulter, 2007; Drury, 2001). Scientists of the Earth have focused on geology of the environment, exploration of hydro-carbon and mineral global experiences in using data remotely sensed (Omer and Zeinelabdein, 2018).

EO has played an important role in geological mapping, especially in areas with limited infrastructure and harsh environmental conditions. EO methods offer: the opportunity to analyse and map surface geology in a relatively short time and at reduced cost; provide additional (sometimes new) information for preliminary geological investigations; and give a synoptic view of a study area often difficult to obtain from field-based observation alone (Chernicoff and Nash, 2002; Kariuki *et al.,* 2004). Broad lithological information is deduced

from a variety of indicators observed in remotely sensed imagery, including landforms, structural features, soils, vegetation types and drainage patterns (Rajesh, 2004 and Agar and Coulter, 2007).

Mineral prospecting and several other mining activities are an important source of national income in most developing countries; with prospectors constantly in search for fast and cheap techniques that can aid the task (Aminzadeh and Samani, 2006). Usually, mineral exploration is capital intensive, and as such, prospectors are often not willing to invest until the presence and quantity of mineralization is empirically ascertained. The uncertainty of the presence and quantity of Gold (Au) minerals in Rafi Local Government Area of Niger state has led to the nefarious activities by illegal miners within the area. Such illegal mining works have continued to increase the rate of environmental degradation and loss of minerals (Sadiya *et al.*, 2015).

Conventional methods for mineral prospecting are costly and time consuming, therefore necessitating the utilization of a faster and cost-effective method. RS has since been utilized as a fast, cost-effective and very reliable tool for geologic mapping and mineral exploration (Goetz *et al.,* 1983). Since the initial stage of RS technology, RS images are applied to mineral exploration in either mapping of geological features, such as fractures and faults, which host ore deposits; and mapping hydrothermal alteration minerals using their spectral features (Sabins, 1999). Discrimination of hydrothermal alteration assemblages and their distribution is an important part in exploration of hydrothermal ore deposits and generation of the most appropriate ore deposit model (Thompson *et al*, 1999).

1.2 Statement of the Research Problem

Mining activities as well as prospecting of mineral and have been on the increase for the past twenty years. Prospectors on the search constantly for newer techniques of technology that can aid them in recognizing mineral reserves in a timeframe faster and at low costs (Zeinelabdein *et al*, 2020). Field data procurement and visual interpretation is labour intensive, time consuming and costly, the use of ground survey method is very limited and cannot be widely applied in other remote and large regions which requires plenty of time and financial backing (Aminzadeh and Samani, 2006).

RS for the identifying rocks that are altered hydrothermally in examining the response of ratios of some band combinations, acceptance of the relationship between lineament and gold mineralization and also, patterns of gold presence especially under simulated environmental condition within the study area has been a challenge and has not been well documented. Therefore, this study will complement the documentary of this.

1.3 Research Question

i. How effective will remote sensing be for mapping hydrothermally altered regions within the study area?

ii. How can the response of bands ratios be examined for hydrothermally altered rocks?

iii. How can the characteristics of sub-surface lineament affect Gold deposit?

iv. In what ways can Multi-criteria analysis under simulated environmental condition be identified within the hydrothermally alteration zones?

1.4 Aim and Objective of the Study:

The aim of this study is to examine the suitability of Landsat imageries with a view to identify Gold prospectivity in Rafi Local Government Area of Niger state, Nigeria. The specific objectives are to:

i. identify the hydrothermally altered regions within the study area using selected band combination.

ii. examine the response of ratios of certain band combinations for hydrothermally altered rocks within the study area.

iii. identify the characteristics of sub-surface lineament and Gold mineralization.

iv. Conduct simulation studies to investigate possible pattern of gold presence within the study area under simulated environmental conditions.

1.5 Scope of the Study

RS technique was used as a suitable tool for mapping possible precursor of Gold (Au) mineralization in the identification of hydrothermally altered rocks by examining the response of ratios of some band combinations using different band ratios on the ENVI and ArcGIS software, adoption of the relationship between lineament and gold mineralization and also, patterns of gold presence especially under simulated environmental condition within Rafi local government area of Niger state. Six spectral bands from LandSAT 8 OLI satellite image was used to detect the hydrothermally altered rock using the various band combination, Lineament extraction was done using the PCI Geomatical software, computation of Principal Component Analysis (PCA) on the ENVI software, Sabin's ratio & Kaufmann's ratio and Multi-Criterial Analysis (MCA) which pointed us to area with the presence of iron oxide, silification and oxidation within the study area.

1.6 Justification of the Study

Mining in developing countries like Nigeria, have exposed the environment to serious hazards by the generation and uncontrolled discharge of enormous amounts of toxic aqueous wastes containing toxic heavy metals, as well as various organic pollutants, which impact adversely on human health and the ecosystem (Nuhu, 2014).

Since mineral prospecting and mining activities have increased during the past two decades, prospectors are constantly on the search for newer technologies that can help them identify mineral reserves in a quicker timeframe and at reduced costs (Zeinelabdein *et al*, 2020).

Despite several research efforts on the global scene where RS is used for lithology mapping, much has not been done in utilizing RS for identification of mineral deposits in Nigeria. Mineral exploration is a capital-intensive venture that requires heavy investment if environmental sustainability is to be achieved.

The use of remote sensing data for detection and quantification of gold is of great benefit to the ascertaining risk assessment, financial viability and environmental impact of exploring the gold mineral.

Lithological classification is an important application in geological remote sensing, and the multispectral data Landsat 8 OLI have been said to be efficient for lithological discrimination (Ge *et al.*, 2018). As an economical and efficient technique, remote sensing has become a popular method for regional lithological mapping and also because information can be acquired at low cost through satellite imagery (Zhang and Li, 2014; Masoumi *et al.*, 2017a). Lithological mapping and recognizing hydrothermally altered minerals through remote sensing instruments have been widely and successfully used for the exploration of epithermal

gold, porphyry copper, massive sulfide, chromite, magnetite and uranium ore deposits (Babiker *et al.*, 2015).

Hazardous effect of illegal mining on areas where little or no pointer to the presence of the study mineral can be reduced if remote sensing technique is accommodated. In this study, RS data would be used to delineate hydrothermal alteration zones within Rafi LGA, with a view to identification of possible gold deposits within the study area.

1.7 Study Area

The study area is Rafi Local Government Area of Niger State, Nigeria (Figure 1.1). It's at the PATH 189 and ROW 53 and on Long 6º 27'31" and Lat 10º 0'41". The site is chosen primarily based totally on the artisanal mining activities on going within the location. Consequently, there are shallow pits and burrows, in which small gold-bearing stones (quartz) are being extracted and deserted after the precious stones were completely extracted.

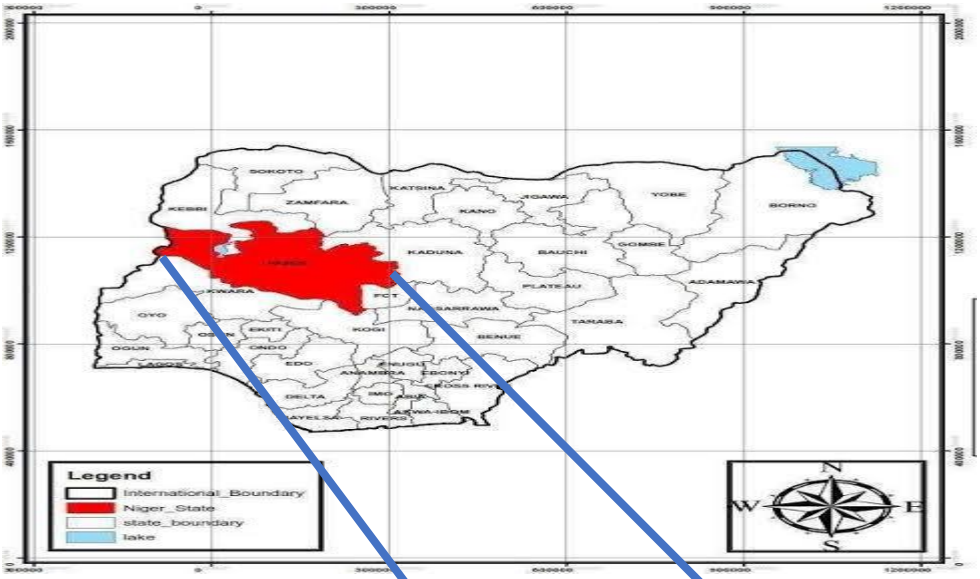

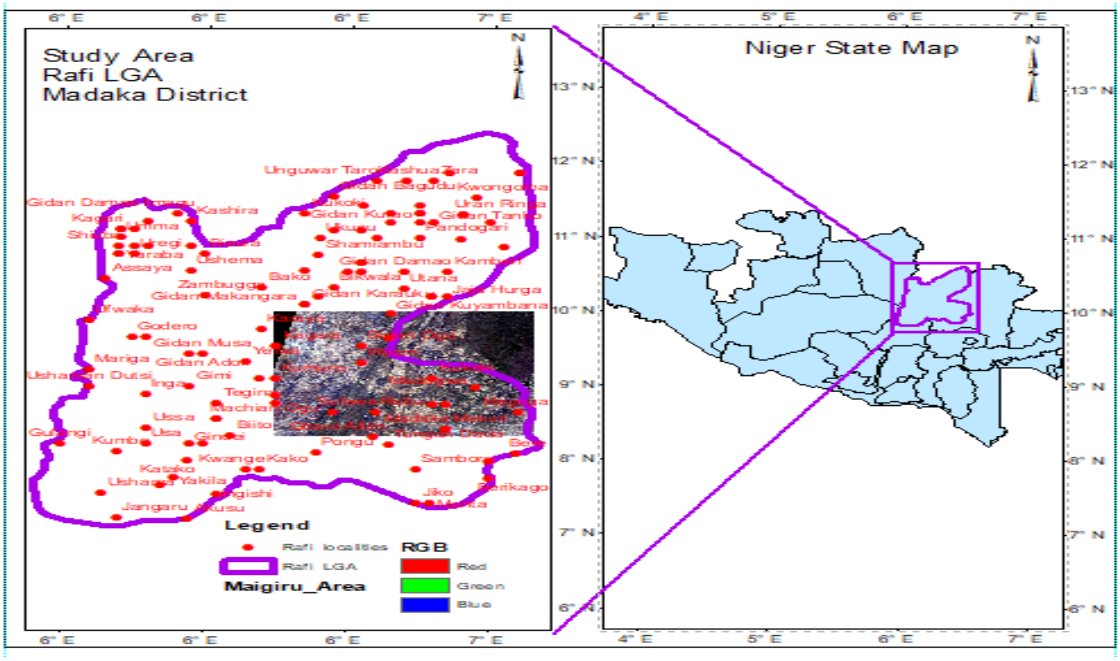

Figure 1.1: Map of the Study Area

1.8 Geology of the Study Area

About half of the landmass of Niger State is underlain by the Basement Complex rocks while the remaining half is occupied by the Cretaceous Sedimentary rocks of the Bida Basin (Figure 1.2). It lies within the north-central portion of the Nigerian Basement complex rock which is characterized by three lithofacies namely; the migmatite-gneiss complex, the low-grade schist belt and the older granites (Olasehinde, 1999). The geological map (Figure 1.2) revealed that the area is underlain by granite and gneiss which in most locations are undifferentiated granite-gneiss-complex.

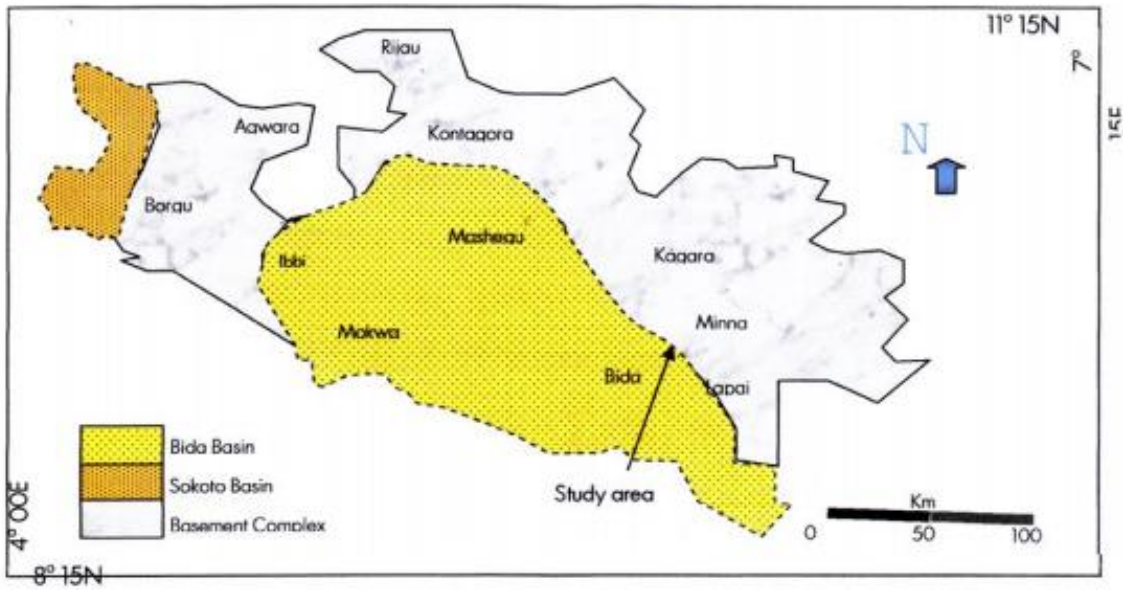

Figure 1.2: Geology of Niger state (Amadi, 2012).

CHAPTER TWO

2.0 LITERATURE REVIEW

2.1 Developments in Lithology and Prospectivity Mapping using RS

In recent years remote sensing has been used significantly in many applications such as geological mapping, agriculture mapping, hydrogeological research and prospecting for mineral deposits. The growing standard of living of the underdeveloped nations involves the search for extra resources to satisfy the needs of the populace. Therefore, new exploration strategies ought to be applied to find out previously unknown reserves. Remote Sensing can

map and examine rocks over masses of square miles in one imagery (Ghazali *et al.*,2015). RS-based geological mapping may indicate particular areas of interest that can then be investigated in detail on the ground. Improved geological understanding leads to looking for new resources in previously overlooked areas (Ghazali *et al.,2015*).

Gold (AU) is a rare element in crustal rocks due to its generally chalcophile properties; it is increasingly enriched in mantle rocks and particularly the metallic core. In nature, gold is often alloyed with silver or copper, although tellurides and selenides are common components in some systems. Gold may substitute into the sulfides pyrite and arsenopyrite, where it is termed refractory, complicating mineral processing. It follows that gold becomes concentrated as magmas fractionally crystallize reporting to sulfide segregations that scavenge gold from the silicate residue (Herrington and Stanley, 2015).

The 79th element on the periodic table of elements occurs in significant amount in three main types of deposit which include

1. hydrothermal quartz vein and related deposit in metamorphic and igneous rock,
2. in volcanic-exhalative sulphide deposit and
3. in consolidated to unconsolidated placer deposit.

It is metallic, and its colour varies from rich yellow to whitish yellow with increasing silver and also in blue and green in transmitted light. It has its peak reflectance at 700nm which is equal to 83.6% and also a member of copper group. Other members include copper, lead, maldonite and silver. Although, Gold cannot be detected directly by any remote sensing method, the presence of minerals such as iron oxides and clay minerals whose diagnostic spectral signatures (in the visible/shortwave infrared portion of the electromagnetic spectrum) could be used as indicators for identifications of hydrothermal alteration zones

which are associated with Gold occurrences. Though Gold cannot be identified directly from satellite images, but the tonal variation indicates matching of hydrothermal alteration zones with the locations of known base metals (Cu, Zn, and Ni), thus manifesting the signatures for gold mineralization in the area (Kotnise and Chennabasappa, 2015).

AU has been extracted from North Eastern parts of Africa for more than 5000 years, and this may be the first place where the metal was extracted (Ghazali *et al.,2015*). The Arabian-Nubian Shield (ANS) is an exposure of Precambrian crystalline rocks on the flanks of the Red Sea. The crystalline rocks are mostly Neoproterozoic in age. ANS includes the nations of Israel, Jordan. Egypt, Saudi Arabia, Sudan, Eritrea, Ethiopia, Yemen, and Somalia. Arabian Nubian Shield Consists of juvenile continental crest that formed between 900 550 Ma, when intra oceanic arc welded together along ophiolite decorated arc. Primary Au mineralization probably developed in association with the growth of intra oceanic arc and evolution of back arc (Ghazali *et al., 2015*). Multiple episodes of deformation have obscured the primary metallogenic setting, but at least some of the deposits preserve evidence that they originate as sea floor massive sulphide deposits. Recent endeavors by the Geological Research Authority of Sudan led to the discovery of a score of occurrences with gold and massive sulphide mineralizations (Ghazali *et al., 2015*).

2.1.1 Importance of remote sensing in mineralization

Remote sensing strategies in mineral exploration research may be used for extracting the subsequent records such as, mapping of rock (types, exposures, geomorphology and structural features), source rock for mineralization, contacts among rock types, shear zones and the crucial faults/fractures, lineament intersections, Extension of present mineralized belts/ formations, Anomalies and systems related to mineral deposits, Mapping of alteration

zones as indicator of mineralization, Base function records inclusive of road/rail network, drainage and water bodies (Krishnamurthy and Sreenivasan, 2005).

2.1.2 Gold mineralization

Gold mineralization takes place along the shape of epithermal veins and veinlets, that's related to zones that are hydrothermally altered. Thus, the identity of zones that are hydrothermally altered is one of the major signs for focus on innovative potential zones of epithermal gold mineralization (Bolouki *et al.,* 2020). Recently, the identification of alteration mineral zones using remote sensing sensors is effectively and extensively used for prospecting porphyry copper, epithermal gold, uranium and massive sulfide deposits in metallogenic provinces around the world (Noori *et al.,* 2019; Pour *et al.,* 2019a).

2.1.3 Mapping areas of high-potential mineralization

The most important mineralogical difference between the altered and unaltered rocks is the abundance of alteration minerals such as alunite, montmorillonite and kaolinite in the altered rocks. Moreover, the difference between the mineralized and the non-mineralized altered rocks is the presence of abundant secondary iron minerals such as goethite, hematite, limonite and jarosite in association with other alteration minerals (Gabr *et al.,* 2010).

In the altered rocks, the change in abundance of any of the above-mentioned alteration minerals would lead to a slight change in the reflectance value that depends on that mineral's spectral characteristics. Sabins (1997) showed the curves of the average spectra form their measurements for both altered and unaltered rocks (Figure 2.1). Sabins (1997) observed that the spectral reflectance of both the altered and unaltered rock are characterized by lower reflectance in the TM band 7 than band 5 while in the visible portion of the spectrum, the altered rocks have higher red reflectance due to the iron enrichment of the rock (Figure 2.1).

The iron oxide-rich parts of the alteration are considered to be the main target for gold exploration.

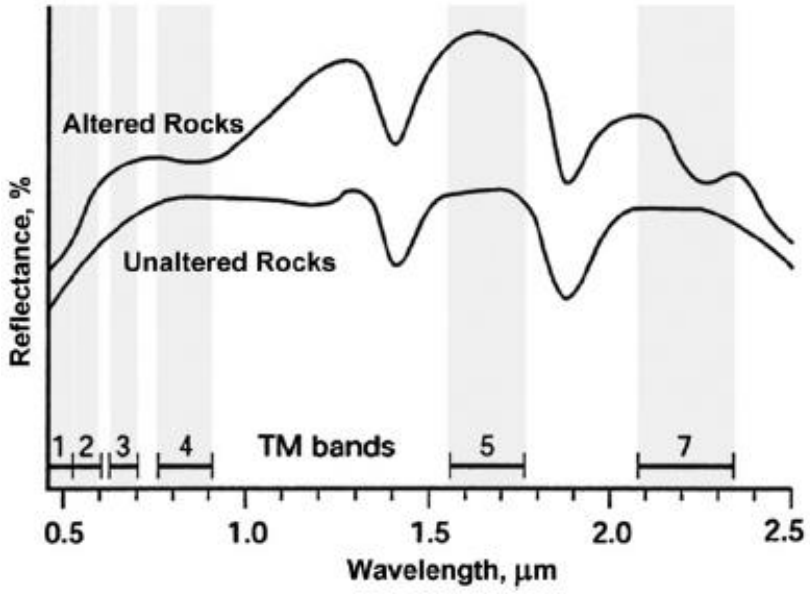

Figure 2.1. Average spectra for both altered and unaltered rocks. Numbers 1–5 and 7 represent the width of each Landsat Thematic Mapper band. (Source: Sabins, 1997).

2.1.4 Lithology

Lithology studies physical properties like colour, texture, composition, or grain size of visible outcrop unit, core or hand samples.

2.1.4.1 *Prospectivity mapping*

Preliminary stages of mineral investigation have continually protected boring and different unfavorable and luxurious exploration strategies to measure ore-deposits underground (Chakraborty *et al.,* 2020). The importance and application of remotes sensing lies in studying spatial items without real bodily interaction, in a quicker and non-unfavorable way. Existence of mineral is spatially measurable via way of means of geophysical, geological and

geochemical styles consequently fashioning remote sensing a number one device for its prospecting (Sabins, 1999).

However, in many environments the ore and mineral deposits with economic value are often covered by vegetation, which poses a challenge for the utility of remote sensing as an exploration tool. Hence, current day exploration will require new and more effective remote sensing-based approaches to support on-going mineral vectoring efforts in areas with less surface rock exposure **(**Chakraborty *et al.,* 2020). In particular, hyperspectral remote sensing, covering Visible Near-infrared (VNIR) and Shortwave Infrared (SWIR), can offer extra capability to explore subtle spectral changes of plants induced by underground metal mineralization (Chakraborty *et al.*, 2020).

2.1.4.2 *Methods of prospectivity mapping*

The following methods are used in prospectivity mapping

i. **Remote Sensing**

In the nineties, the Geological Research Authority of Sudan (GRAS, 1989) in cooperation with BRGM (Bureau de Recherches Geologiques et Minieres) utilized satellite data of Landsat TM using spectral ratio technique to map possible mineralized zones in the Red Sea Hills of Sudan. The outcome of the study mapped a gossan type gold mineralization. Band ratio technique was applied to Arbaat area and a signature of alteration zone was detected. The alteration zones are commonly associated with mineralization. A filed check confirmed

the existence of stock work of gold bearing quartz in the alteration zone. Another type of gold mineralization that was discovered using remote sensing is the gold associated with metachert in the Atmur Desert (GRAS, 1989).

As knowledge of geology and mineralization of the Red Sea hills improved, it became increasingly apparent that mineral deposits are located along linear structures trending NE-SW of their study area and are associated with acid volcanicity (Ghazali *et al.,2015*). In crustal processes, gold is generally soluble as either chloride or sulfur complexes depending on fluid parameters. Gold contents in hydrothermal fluids are generally low and a world-class gold deposit demands the migration of world-class volumes of fluids through an ore-bearing system to produce it. At surface, gold is largely concentrated physically by residual, fluvial, and eolian processes, except in extreme weathering conditions (Herrington and Stanley, 2015). Hydrothermal alterations and weathering processes of the sulphide mineralization produce spectral anomalies that extend beyond the ore body itself. To this end satellite images provide a superb synoptic view of the structural features and the spectral anomalies. Special interest was focused on ratio image processing techniques, whereby false colour composite images were produced using combination of bands in Red, Green and Blue, that rendered maps of alteration zones. Ground-truthing of the outlined areas disclosed the existence of stockworks that contain gold and sulphide mineralization (Ghazali *et al.,2015*).

The most common type of alteration is the breakdown of feldspars and ferromagnesian minerals to a variety of clays and other hydroxyl bearing minerals. Such minerals can be detected by remote sensing techniques since the ShortWave infrared (SWIR) range of their spectra exhibit absorption (Drury 1993). Besides, a considerable number of ore occurrences contain sulphide minerals particularly pyrite (FeS_2) which undergo breakdown to sulphuric acid and a number of ferric hydroxides and complex sulphates which are both strongly

coloured and possess crystal field absorption in the visible and near infrared range (VNIR) (Sabins, 1987; Drury, 1993). This suite of alteration features proved to be extremely useful in delineating a variety of hydrothermal ore deposits (Drury, 1993). It has been well established that ferric iron exhibits pronounced absorption features at around 0.82 μm and 0.35μm, whereas ferrous iron has absorption at 1.0, 4.8-2.0 and 0.55-0.45. Hydroxyl – bearing minerals like clays have a major absorption feature around 1.9, 2.35 and 2.5 (Gupta, 1991). Detection of the above-mentioned minerals has been used as prospecting guide for ore deposits. Ratio images are known for enhancement of spectral contrasts among the bands considered in the rationing and have successfully been used in mapping alteration zones (Segal, 1983).

Conventional methods like color composites, several band rationing techniques, are applied to the original unregistered raw data. The resulting images are considered to be the potential alteration maps. The band ratio images are known for enhancement of spectral contrasts among the bands considered in the ratio operation and have successfully been used in mapping of alteration zones (Segal 1983). From the theoretical knowledge of mineral's spectral properties, it is well recognized that the Landsat TM bands ratios of 3/1, 5/7, 5/4 are analyzed for iron oxides, hydroxyl bearing minerals, ferrous oxides, respectively. Based on the above considerations the spectral features of ferric and hydroxyl – bearing mineral, in which hydrothermally altered rocks are often rich, are used to produce a false colour composite image using combinations of bands 5/7, 5/4 and 3/1 in R, G and B respectively. The obtained image mapped the alteration zone in reddish yellow. Another composite ratio image was produced using bands 5/7, 3/1 and 4/3 in R, G and B respectively. Although this combination of ratio image appears to be fairly different from the previous one, the final result remains the same thus lending support to the previous conclusion (Ghazali *et al.,* 2015).

Kotnise and Chennabasappa (2015) applied colour composite, band rationing, principal components analysis (PCA), and spatial filtering enhancement techniques for their image processing. The production of color composite images is based on known spectral properties of rocks and alteration minerals in relation to the selected spectral bands. For instance, LandSat TM band 7 is used primarily for mineral and rock discrimination, whereas bands 4 and 5 are primarily used for vegetation monitoring. Spectral analysis exploits spectral properties of rocks in order to interpret lithological variations in rock alterations that are expressed as variations in colour intensity values within colour composite images. Colour composite images displayed as red, green, and blue (RGB), respectively, show rocks of similar composition in colors that tend to have same resemblance. They used Spatial filtering for extraction of features like geologic lineaments. These filters enhance visual interpretation of remotely sensed lineament maps and to get smoothness in the images.

Multi spectral remote sensing (Landsat+ and ASTER) was used for image enhancement and interpretation in the identification, detection, and in delineation of lithological rock units, hydrothermal alterations, and geologic structures associated with auriferous sulphide deposits in the southern extension of Kolar Schist belt by Perry and Vincent (2009). Kotnise and Chennabasappa (2015) also used Landsat images to indicate the influence of Structural controls in gold mineralization.

Chernicoff and Nash (2002) combined a 1-4-7 composite of Landsat Thematic Mapper (TM) bands with aeromagnetic data for analysing geological structures in the northern Precordillera region of Argentina. The information derived from the Landsat (TM) imagery conformed to published maps and also revealed a new set of previously unknown structures. The resulting structures were superimposed on an aeromagnetic image, which enabled the precise delineation of lithomagnetic domain boundaries and magnetic pattern breaks

(inferred faults). The combination of these datasets led to the definition of a major structural system which controls the economic potential of gold targets in their study area.

For many years EO for geological mapping was focused on the use of spectral information to detect alteration zones (Pour and Hashim, 2012a; 2012b) and for lithological mapping (Hewson *et al.*, 2005) without exploiting spatial information. It has been acknowledged that the incorporation of spatial information improves spectral classification (Blaschke, 2010), more so in geology due to its ability to infer geological transitions. Traditional EO lithological boundary detection is often subjective, with distinct variation occurring between expert analyses.

Saliti *et al*, (2011) investigated the automatic detection of lithological boundaries based on the pattern rotational variant template edge matching algorithm of ASTER imagery in the South West of Iran. The accuracy of the detected lithological boundaries was spatially assessed by five experts against two reference sources: a published geological map produced by Iranian oil operation companies (scale 1:100 000) and boundaries interpreted from a pair of stereo aerial photographs (scale 1:50 000). Although the results could not be quantified (due to no ground truth data of mineral composition), a comparison of the boundary detection with those of reference sources showed a spatial correspondence between rotational variant template edge matching technique and reference boundaries. It was noted that in heterogeneous areas this method did not correlate with the reference boundaries.

ii. **Hyperspectral remote sensing for mineral exploration**

Hyperspectral remote sensing employs from 100 to 200 contiguous spectral bands to record a complete and contiguous spectrum for each image pixel. For many geological materials (rocks, soils and minerals) and some vegetation types, these spectral curves are diagnostic of

the molecular structure and chemical composition of that material. This leads to the possibility of not just discriminating the material but actually identifying it and putting a name to the major mineral components present in every pixel of an image. Many a times a single pixel has mixture of minerals. Such mixing produces composite spectra unlike anything in one's database of spectral signatures of materials. Computer algorithms are available to de-convolve, or separate, the mixed signature, determine the relative proportions of the several materials within the field of views and identify their spectra against a database of known materials.

Hyperspectral sensing thus allows "Mineral Mapping", i.e., identification and mapping of rock, regolith and alteration mineralogy using the principle of spectroscopy (Figure 2.2). Thus a "Mineral Map" can now be made to help exploration units to narrow down on zone of mineral alteration around mineral deposits and detect previously unrecognized mineral patterns across mineral belts (Huntington, 1998).

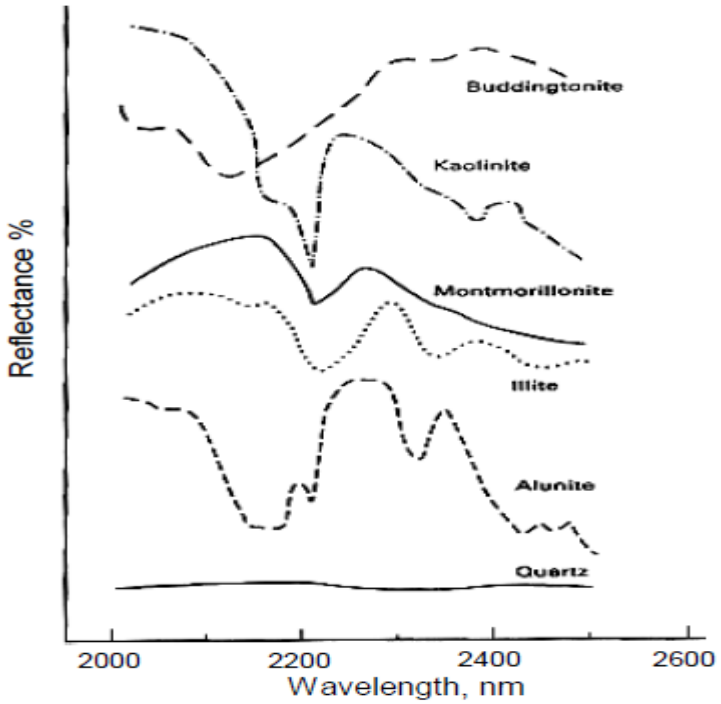

Figure 2.2. Spectral reflectance curves for some alteration minerals. Minor absorption features help distinguishes minerals (Source: Sabins, 1987).

Two major application areas of hyperspectral data to mineral exploration are: First, Lithologic and mineral mapping, i.e., direct sensing of bedrock and minerals and second, Geobotanical mapping, i.e., exploration in vegetated environments which has the potential of identifying the areal distribution of specific element associated spectral changes in vegetation which are related to soil geochemistry or lithology. Geobotanical anomalies associated with ore bodies may also be expressed as abrupt changes from one plant community to another or as specific indicator plant species. Hyperspectral remote sensing data are well suited to mapping bedrock and identifying the presence and abundance of specific diagnostic minerals at specific scales (Rivard *et al*., 2002).

The minerals that have been successfully identified to date with hyperspectral remote sensing are: OH-bearing minerals, carbonates, sulphates, olivines, pyro-xenes, iron oxides and hydroxides. The identification of minerals and the mapping of their distribution provide the necessary leads for exploration of related mineral deposits (Rivard *et al*., 2002). The advantage of hyperspectral remote sensing to mineral exploration is the ability to identify the presence, distribution and abundances of specific diagnostic minerals that will help direct mineral exploration at considerable cost savings.

The use of airborne hyperspectral imaging spectrometers such as HyMAP (Cocks *et al.*, 1998) or HySpex (Baastad *et al.*, 2005) is a common approach in exploration campaigns recently (Van der meer *et al.*, 2012). These airborne sensors combine a good signal-to-noise ratio and a good spectral and spatial resolution. However, the usage of these systems in large and remote areas involves high costs due to the difficult logistics that is involved in airborne hyperspectral campaigns.

Therefore, the usage of multispectral imagers, such as the Operational Land Imager aboard Landsat-8 (Irons *et al.,* 2012) and Sentinel-2 (Drusch *et al.,* 2012) in combination with hyperspectral spaceborne instruments such as Hyperion (Ungar *et al.,* 2003) and EnMAP (Kaufmann *et al.,* 2006), will increase in geological mapping and exploration campaigns to reduce airborne related costs to a minimum possible extent.

This is due to the open data policy that accompanies these spaceborne missions as in the case of the National Aeronautics and Space Administration's (NASA's) EO-1 satellite, or NASA's Landsat programme. The future European Sentinel-2 and the future German EnMAP missions will supply data with a similar data usage policy to the geoscientific community worldwide.

iii. **Geophysical methods**

Geophysical tools, including different techniques such as magnetic, self-potential (SP), induced polarization (IP) and resistivity, are important techniques in mineral exploration for ores located in basement rocks. Integrated geophysical methods were used for mineral exploration (Macnae 1979, Smith 2002). The IP technique was used for mineral exploration, as well as for hydrological and environmental geology studies (Kiberu 2002; Sternberg and Oehler 1990). Also, the self-potential (SP) method has a wide range of applications in engineering and geotechnical investigations (Corwin 1984, Markiewicz *et al* 1984), in geothermal exploration (Corwin and Hoover 1979, Anderson 1984) and in the exploration for minerals, particularly metallic sulfides (Corry 1981, Yungul 1950). In addition, the magnetic technique was used by Ramadan and Sultan (2004) for identifying massive sulfide zones.

Exploration geophysics plays a major role in unlocking mineral reserves. It is well recognized that many easily discovered large mineral deposits with a strong geophysical signature have

already been identified. Future discoveries present significant challenges, being located undercover, in remote areas, and with less prominent geophysical signals.

Fu *et al.*, (2020) discuss an application of various deep-penetrating geophysical techniques to the exploration of ore deposits. In particular, they consider an important role of geophysical surveys in studying the banded iron formations (BIF). It is well known that the large-scale BIF-type iron mines represent one of the most important iron ore resources in the world. They constitute 70% of the world's high-grade iron ore reserves, and BIF type iron mines produce over 90% of the world's iron ores. They are found all over the world, but mainly in Russia, Australia, Brazil, Canada, China, Africa, India, and the United States.

Fu *et al.*, (2020) present the results of integrated geophysical surveys in the Anshan-Benxi area of the North China Craton, where several major BIF-type iron deposits are located.

Fu *et al*, (2020) used deep-penetrating geophysical methods, including the high-precision ground magnetic survey (HPGMS), transient electromagnetic (TEM), and magnetotelluric (MT) methods. The results show that an optimal combination of these geophysical methods makes it possible to accurately determine the anomalous spatial locations and morphologies of the concealed iron ore bodies.

Alfouzan *et al*, (2020) present the results of the Saudi Arabian Glass Earth Pilot Project which was a part of the geophysical exploration program to explore the upper crust of the Kingdom for minerals, groundwater, and geothermal resources. The project began with a large-scale airborne geophysical survey over approximately 8000 sq. km of green-field area, including electromagnetic (EM), magnetics, and gravity methods (Zhdanov *et al*, 2018). Based on the results of the airborne survey, several prospective mineralization targets were identified for follow-up exploration. A spectral induced polarization (SIP) survey was completed over one of the prospective targets. The field data were collected with a distributed array system,

which had the potential for a strong inductive coupling (IC) effect. Alfouzan *et al.*, (2020) developed a method to fully include all 3D IC effects in the inversion of induced polarization (IP) data. The field SIP data were inverted using the generalized effective-medium theory of induced polarization (GEMTIP) in conjunction with integral equation-based modeling and inversion methods. The results of this inversion were interpreted and used to design a drill hole set up in the survey area, which intersected significant mineralization associated with gold, silver, and other base metals.

Zhang *et al*, (2020) applied controlled-source first-arrival tomography to study the P wave velocity structure of the Zhuxi ore deposit, located in Jiangxi province, South China. Their velocity model identified the proven orebodies, mainly related to magmatic hydrothermal activities during the Yanshanian period. These were visible as high-velocity zones, corresponding to widespread copper–iron and a few tungsten–molybdenum orebodies. These results helped to further evaluation of the total reserves, suggesting that seismic tomography could be a useful tool for mineral exploration.

Raju and Kumar (2020) demonstrated how airborne and ground magnetic survey data could be effectively used for studying the Iron–Oxide–Copper–Gold (IOCG) deposits in Gadarwara, showed that such deposits could be inferred from the predictive magnetic exploration models combined with geological observations and petrophysical data.

Ihbach *et al*. (2020) examined the water potential of aquifers within in the phosphatic series in Morocco, using a combination of several geophysical methods: magnetic resonance sounding (MRS), electrical resistivity tomography (ERT), time-domain electromagnetics (TDEM), and frequency-domain electromagnetics (FDEM). Ihbach *et al*. (2020) demonstrated the efficiency of the MRS method for prospecting groundwater resources, and evaluated the importance in the geological context of Youssoufia open-pit mining in

Morocco. The ERT method was used to delineate the conductive horizons attributed to the groundwater aquifers. The TDEM and FDEM data were used for mapping and delimiting the aquifer potential recharge zones in the phosphate series. In summary, the authors confirmed the effectiveness of the developed approach to geophysical prospecting for groundwater resources in phosphate deposits.

2.2 Remote Sensing and Electromagnetic Spectrum in Mineral Prospecting Studies

The use of remote sensing for discrimination of the different geological materials on the surface of the earth is based on the way the Electromagnetic Radiation (EMR) interacts with the different features on the earth. An electromagnetic (EM) field is a physical field produced by charged objects and theoretically extends to infinity. It acts by the Lorenz force on the charged objects found in it.

An electromagnetic field is a combination of an electric and a magnetic field, with the electric field being produced by stationary charges and magnetic charges in motion (electric currents). In the past, theories of electric and magnetic fields were considered separately, and later it was understood that electric and magnetic fields were only two parts of one larger whole of the electromagnetic field.

From the standpoint of classical theory, the EM field can be considered as a smooth continuous field propagating in the form of waves, while from the point of view of quantum mechanics it can be viewed as being made up of individual corpuscle photons. Accordingly, the EM field can be seen as: continuous structure or discrete structure (Dervic *et al.*, 2019).

Electromagnetic radiation is a self-propagating wave in space or through matter, and it has both electrical and magnetic components that oscillate in phase normally (at an angle of 90 °) to each other and in the direction of the propagation of the wave or energy. Otherwise, the

term "radiation" means energy in the form of waves or sub-atomic particles in motion emitted by atoms or other bodies, when it changes from a higher energy state to a lower energy state (Dervic *et al.*, 2019).

No known medium is opaque to all wavelengths of the electromagnetic spectrum (Figure 2.3), which extends from radio waves, whose wavelengths are measured in kilometers, through the infrared, visible, and ultraviolet spectral regions, to x-rays and gamma rays, of wavelengths down to 10, −13 m. Similarly, no material medium is transparent to the whole electromagnetic spectrum. A medium which absorbs a relatively wide range of wavelengths is said to exhibit general absorption, while a medium which absorbs only restricted wavelength regions of no great range exhibits selective absorption for those particular spectral regions. For example, the substance pitch shows general absorption for the visible region of the spectrum, but is relatively transparent to infrared radiation of long wavelength. Ordinary window glass is transparent to visible light, but shows general absorption for ultraviolet radiation of wavelengths below about 310 nanometers, while colored glasses show selective absorption for specific regions of the visible spectrum. The color of objects which are not self-luminous and which are seen by light reflected or transmitted by the object is usually the result of selective absorption of portions of the visible spectrum (Figure 2.3). Many colorless substances, such as benzene and similar hydrocarbons, selectively absorb within the ultraviolet region of the spectrum, as well as in the infrared (West, 2014).

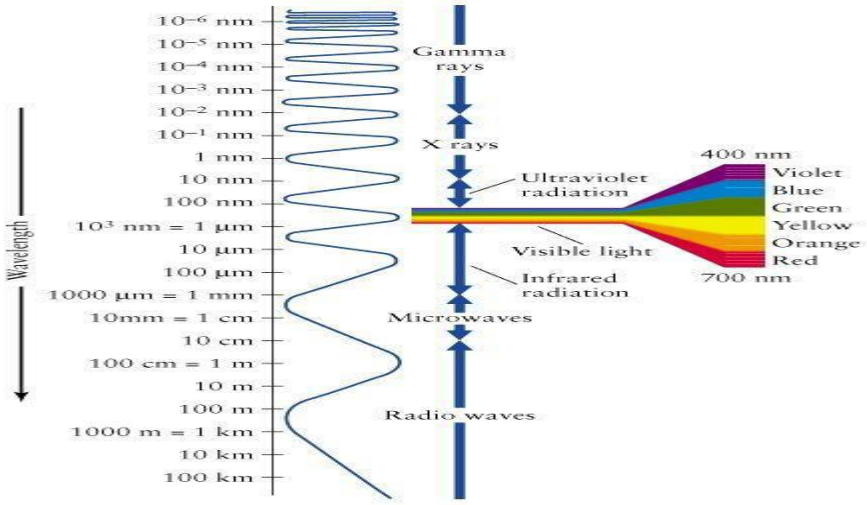

Figure 2.3: The electromagnetic spectrum (Source: Dervic *et al.*, 2019).

2.2.1 Laws of absorption

The capability of a medium to take in radiation relies upon on some of factors, in particular the digital and nuclear charter of the atoms and molecules of the medium, the wavelength of the radiation, the thickness of the soaking up layer, and the variables which decide the country of the medium, of which the maximum crucial are the temperature and the attention of the soaking up agent. In unique cases, absorption can be encouraged via way of means of electric powered or magnetic fields. The country of polarization of the radiation affects the absorption of media containing sure orientated structures, consisting of crystals of apart from cubic symmetry (West, 2014).

2.2.2 Lambert's law

Lambert's law, also called Bouguer's law or the Lambert-Bouguer law, expresses the effect of the thickness of the absorbing medium on the absorption. If a homogeneous medium is thought of as being constituted of layers of uniform thickness set normally to the beam, each layer absorbs the same fraction of radiation incident on it. If *I* is the intensity to which a

monochromatic parallel beam is attenuated after traversing a thickness *d* of the medium, and I_0 is the intensity of the beam at the surface of incidence (corrected for loss by reflection from this surface), the variation of intensity throughout the medium is expressed by Equation 2.1,

$$I = I_O e^{-\alpha d} \quad (2.1)$$

in which α is a constant for the medium called the absorption coefficient. This exponential relation can be expressed in an equivalent logarithmic form as in Equation (2.2),

$$log_{10}(I_O/I) = (\alpha/2.303)\mathrm{d} = \mathrm{kd} \quad (2.2)$$

where $k = \alpha/2.303$ is called the extinction coefficient for radiation of the wavelength considered. The quantity $\log_{10}(I_0/I)$ is often called the optical density, or the absorbance of the medium. Equation 2.2 shows that as monochromatic radiation penetrates the medium, the logarithm of the intensity decreases in direct proportion to the thickness of the layer traversed. If experimental values for the intensity of the light emerging from layers of the medium of different thicknesses are available (corrected for reflection losses at all reflecting surfaces), the value of the extinction coefficient can be readily computed from the slope of the straight line representing the logarithms of the emergent intensities as functions of the thickness of the layer. Equations 2.1 and 2.2 show that the absorption and extinction coefficients have the dimensions of reciprocal length. The extinction coefficient is equal to the reciprocal of the thickness of the absorbing layer required to reduce the intensity to one-tenth of its incident value. Similarly, the absorption coefficient is the reciprocal of the thickness required to reduce the intensity to $1/e$ of the incident value, where *e* is the base of the natural logarithms, 2.718 (West, 2014).

2.2.3 Absorption measurement

The measurement of the absorption of homogeneous media is usually accomplished by absolute or comparative measurements of the intensities of the incident and transmitted

beams, with corrections for any loss of radiant energy caused by processes other than absorption. The most important of these losses is by reflection at the various surfaces of the absorbing layer and of vessels which may contain the medium, if the medium is liquid or gaseous. Such losses are usually automatically compensated for by the method of measurement employed. Losses by reflection not compensated for in this manner may be computed from Fresnel's laws of reflection (West, 2014).

2.2.4 Scattering

Absorption of electromagnetic radiation should be distinguished from the phenomenon of scattering, which occurs during the passage of radiation through inhomogeneous media. Radiant energy which traverses media constituted of small regions of refractive index different from that of the rest of the medium is diverted laterally from the direction of the incident beam. The diverted radiation gives rise to the hazy or opalescent appearance characteristic of such media, exemplified by smoke, mist, and opal. If the centers of inhomogeneity are sufficiently dilute, the intensity of a parallel beam is diminished in its passage through the medium because of the sidewise scattering, according to a law of the same form as the Lambert-Bouguer law for absorption, given in Equation (2.3),

$$I = I_0 e^{-\tau d} \tag{2.3}$$

Rocks consisting of assemblages of minerals comprise of various proportions of different elements, held together as molecules by different types of bonds (Drury, 1987). When EMR interacts with these materials, three types of transitions can occur viz., electronic, vibrational and rotational. The transitions are conditioned by such features as the types of bonds, the co-ordination state of atoms within the molecules of the minerals of which the rock is made of, the valency of the atoms (Drury, 1987). The energy detected by the remote sensing systems over the spectrum of EMR is therefore a function of how energy is partitioned between its

source and the materials with which it interacts on its way to the detector. The energy of any particular wavelength of radiation may be

1. transmitted through the material,
2. absorbed within it,
3. reflected by its surface, scattered by its constituent particles or re-radiated at another wavelength after absorption.

Any material therefore has a characteristic spectrum, depending on its chemical and molecular composition. However, since the Earth's surface comprises a host of combinations of different organic and inorganic compounds, the actual spectrum observed may have wide range of components (Drury, 1987).

Availability of satellite remote sensing data in digital form makes it amenable for applying of various digital enhancements through the digital image processing techniques, which further help in bringing out valuable information on litho contacts, structural features and various anomalies associated with the occurrence of mineral deposits (RRSSC, 2004).

Type of Remote Sensing data required for mineral exploration will depend on various factors like the scale of mapping, the type of terrain under investigation, the target minerals and the stage of mineral exploration.

Mineral exploration strategy will depend on, firstly, what kind of geological/ lithological terrain we are exploring, which necessitates the need for geological mapping as an initial step. Secondly, the strategy will also depend on what kind of minerals are likely to be found in the terrain, which necessitates the need for knowledge of rock and mineral association (Krishnamurthy and Sreenivasan, 2005).

2.2.5 Mapping hydrothermal alterations

Generally, in geological region the alteration zones are the indicator for the presence of ore body and give the nearest location for the gold deposit. Most of the alteration types associated with gold deposits is sericitization, oxidation, silicification, carbonitization, and ammoniation (Nouri, 2015).

Hydrothermal alteration is proximal to many precious and base metal deposits, such as, in Archean greenstone belts, volcanogenic massive sulphide (VMS) deposits, porphyries as well as intrusion-related and orogenic gold mineralisation. These deposits are the result of hydrothermal to magmato-hydrothermal systems encompassed by thin (centimetres) to extensive (hundreds of kilometres) alteration halos (Cooke *et al* 2014). Halos are important indicators to mineral exploration companies, which are continually searching for reliable and easy-to-use approaches for finding mineralisation sites.

Alteration is an open system process that results in chemical and mineralogical changes in a rock. A similar definition applies to metamorphism. However, the chemical changes induced by metamorphism are generally less intense than those observed within altered rocks. Distinction between these processes is subtle where deposits are formed by metamorphic fluids, such as orogenic gold deposits (Phillips and Powell, 2010). Weathering is another process that induces extreme chemical and mineralogical changes, but in contrast to hydrothermal alteration, it is restricted to superficial rocks and involves low-temperature fluids.

Hydrothermal alteration is also generally distinguished from changes induced in rocks by magmatic fluids (e.g., fenitisation (Morgan, 1989)). However, again the distinction is subtle, as magmatic fluids are involved in several mineralising processes, such as porphyries, syenite-associated deposits, and some VMS (Sillitoe, 2010).

The products of alteration provide insights into the characteristics of hydrothermal systems, while also being useful vectors toward mineralization. Metals tend to concentrate in the most intensely altered rocks; sites where the greatest amount of fluids (high fluid/rock ratio) having peculiar characteristics (such as highest temperature, lowest pH) interacted with crustal rocks. However, to be useful for exploration, alteration must be recognised, typified, but, most importantly, quantified (Mathieu, 2018).

The ability to discriminate between hydrothermally altered and unaltered rocks are considerable in mineral exploration studies (Pour and Hashim, 2014). In the region of solar reflected light, many minerals demonstrate diagnostic absorption features due to vibrational overtones, electronic transition, charge transfer and conduction processes (Cloutis, 1996).

Different hydrothermal processes have certain mineral associations, such as iron-bearing minerals (e.g., goethite and hematite) and hydroxyl bearing minerals (e.g., kaolinite and alunite), which have significant spectral characteristics that allow their identification using optical remote sensing data through the use of different image processing techniques (Sabins, 1999; Crósta *et al*., 2003).

2.2.6 Relationship between spectrum portion and hydrothermal alteration

Hydrothermally altered rocks are regularly indicated via way of means of clay, iron oxide, sulfate minerals and carbonate which make diagnostic absorption signatures during the scene and close to infrared (VNIR) and shortwave infrared (SWIR) areas (Pour and Hashim, 2014). The shortwave infrared radiation is the best spectral region of the electromagnetic spectrum for sensing various aspects of hydrothermal alteration zones. Hydroxyl-bearing minerals present diagnostic spectral absorption features in the shortwave infrared radiation region, and thus this wavelength region is the best to explore and map hydrothermal alteration zones (Pour and Hashim, 2014). The importance of recognizing the spatial patterns of alteration

minerals makes remote sensing one of the standard procedures in exploration geology. It is realized now that certain minerals associated with hydrothermal processes show diagnostic spectral features that allow their remote detection and identification (Modabberi, 2017).

2.2.6.1 *Sulphidation*

Sulphidation makes sulphides from fluids generally carrying S and metals. If these elements combine with the Fe of the host rock, then only S and the metal gains are measured (Table 2.1). Lithological controls are expected in Fe-enriched contexts (e.g., Fe-formations of Meliadine, an orogenic gold district) (Lawley *et al.*, 2015).

2.2.6.2 *Silification*

Silicification is expressed in the field as quartz veins and stockwork or as "silica flooding" (i.e., pervasive silicification). Silicification is common, as Si is an abundant and soluble element (Table 2.1). An addition of Si to a rock produces either quartz (Equation 2.4) or other minerals in; for example, iron formations (Equation 2.5) (Colvine, 1988). However, silicification and quartz proportions correlate poorly, because magmatic, detritic, and metamorphic quartz are abundant, and because quartz is a sub-product of several alteration reactions (Equations 2.6–2.9) (Colvine, 1988). It is thus best to use mass balance calculations instead of petrological observations to quantify silicification.

$$H_4SiO_4 \text{ <==> } SiO_2 + 2H_2O \quad (2.4)$$

$7Fe_3O4$ +	$24SiO_2$	+	$3H_2O$	=>	$3Fe_7Si_8O_{22}(OH_2)$ +	$5O_2$
Magnetite	quartz		fluid		grunerite	fluid

(2.5)

2.2.6.3 *Carbonatisation*

Carbonatisation produces carbonates and corresponds to a CO2 gain (Table 2.1). To remain in a rock, C must combine with Ca, Mg, and/or Fe, which are either brought by the fluid or

are taken from the constituent minerals of the fresh rock. In the latter case, maximum carbonate proportion is dependent on the composition of the precursor. Furthermore, if C combines with the Ca of plagioclase, then paragonite and quartz by-products form, while the destabilisation of other minerals—alkali feldspar and clinopyroxene—may form muscovite and chlorite (Mathieu, 2016). Thus, quantifying the intensity of carbonatisation and distinguishing phyllosilicate by-products from those related to sericitisation and chloritisation processes is not straightforward. Characterisation of the carbonate phases is also pertinent, as Ca- and Fe-Mg-carbonates are observed in weakly and intensely altered rocks, respectively (Equation 2.6, modified from Colvine (Colvine, 1988)).

$3(Mg,Fe)_5Al_2Si_3O_{10}(OH)_8 + 15CaCO_3 + K^+ + 15CO_2 =>$

$KAl_3Si_3O_{10}(OH)_2$+15Ca(Mg,Fe)$(CO_3)_2$+ 3SiO2 + 11H2O + 5O2

chlorite + calcite + fluid => white mica + ankerite + dolomite + quartz + fluid (2.6)

2.2.6.4 *Sericitisation*

Sericitisation is an acidic alteration that produces white mica-mostly thin muscovite (sericitic texture). A commonly held belief is that sericitisation is systematically accompanied by a K-gain (Equation 2.7). However, sericitisation destabilises feldspar and may induce K-loss (Equation 2.8 (Leitch and Lentz (1994); Barrett and MacLean, (1994)). Depending on the precursor, by-products such as albite and quartz may be produced (Equation (2.9) (Colvine, 1988) and plagioclase destruction may produce paragonite. Sericitisation generally results in Ca- and Na-losses, accompanied by a K-gain or loss (Table 2.1).

$3NaAlSi_3O_8 + K^+ + 2H^+ <==> KAl_3Si_3O_{10}(OH)_2 + 3Na^+ + 6SiO_2$

Albite fluid muscovite fluid quartz (2.7)

$3KAlSi_3O_8 + 2H^+ <==> KAl_3Si_3O_{10}(OH)_2 + 2K^+ + 6SiO_2$

Orthoclase fluid muscovite fluid quartz (2.8)

$4(Na,K)AlSi_3O_8 + 2H^+ <==> NaAlSi_3O_8 + KAl_3Si_3O_{10}(OH)_2 + 6SiO_2 + 2Na^+$

Alkali feldspar fluid albite muscovite quartz fluid (2.9)

2.2.6.5 *Chloritisation*

Chloritisation corresponds to gains of Fe and Mg and produces chlorite (Table 2.1). As with carbonatisation, Fe- and Mg-gains induce mineralogical changes as these elements combine with Si—transported or not by the fluid—and Al (an immobile element) to form chlorite. This process is well documented in VMS systems, where chloritisation destabilises the muscovite produced by a preceding sericitisation process, induces K-loss, and increases the acidity of the fluid (Equation 2.10) (Large, 2001). In addition, a zonation is generally observed, with Mg-chlorite being more distal from the core of the system than Fe-chlorite (Embley, 1988). Chloritised rocks display Fe- and/or Mg-gains and Ca-, Na-, and/or K-losses.

$2KAl_3Si_3O_{10}(OH)_2 + 3H_4SiO_4 + 9Fe^{2+} + 6Mg^{2+} + 18H_2O = 3Mg_2Fe_3Al_2Si_3O_{10}(OH)_8 + 2K^+ + 28H^+$

muscovite fluid chlorite fluid (2.10)

Table 2.1. Alteration types and associated chemical changes and alteration minerals.

	Mass Changes	Examples of Assemblages
Sulphidation	+S, +metals	Any minerals + sulphides
Silicification	+ Si	Any minerals + quartz

Carbonatization	+C, (+Ca)	Carbonate ± quartz – white mica-chlorite (Gifkins, 2005) Talc + chlorite + carbonate (Kishida and Kerrich, 1987)
Sericitisation	+K or -K, -Na, -Ca, +H	White mica + quartz + pyrite
Chloritization	+Fe, +Mg, +H -Na, -Ca, -K	Chlorite + pyrite + white mica ± quartz (Gifkins, 2005)
Propylitization	+H, +C	Epidote + chlorite + albite ± carbonate (Witt, 1992)
k-feldspar alteration	+K, -Na	k-feldspar + biotite + quartz (Witt, 1992)
Albitization	+Na, -K	Albite+hornblende±biotite-quartz (Witt,1992)

Source: (Gifkins, 2005)

It is equally important to know mineral genesis, i.e., the nature of mineralisation or its origin. Whether the mineral deposit is Primary (In Igneous rocks), Secondary (in sedimentary and metamorphic rocks) or Tertiary (transported - Placer deposits) and also, it is required to know the processes responsible for mineral formation, i.e., whether the deposit has formed due to Sedimentary, Metamorphic, Igneous, Hydrothermal or Syngenetic/epigenetic processes (Krishnamurthy and Sreenivasan, 2005). Another important aspect to look for during mineral exploration is the 'controls on mineralisation'. Most of the mineral deposits have structural (e.g faults, joint sets, folds, cracks or fractures) control, e.g. gold, copper, etc., whereas some minerals like bauxite have geomorphological (caused by relief) control. Primary mineralization in Nigeria is mostly lithologically and structurally controlled (Ajakaiye *et al*., 1991). Structures include faults, shear zones (lineaments), pegmatites, quartz and quartzite veins (Ejepu *et al* 2018).

The mineralisation related anomalies are the most important parameter, which has to be looked for while extracting information from satellite imageries for mineral exploration.

Some of the important mineralisation related anomalies that can be interpreted from satellite data as identified by Krishnamurthy and Sreenivasan, (2005) are;

1. Gossan zones,
2. Alteration zones (gold, copper, etc. mineralisation),
3. Highly fractured zones and carbonate rocks in metamorphic regime (hydrothermal mineralisation).
4. Quartz veins (hydrothermal mineralisation such as gold),
5. Carbonatite bodies (hydrothermal mineralisation) (Krishnamurthy and Sreenivasan, 2005).
6. Shear zones and lineament intersection zones in highly deformed rocks specially in mineralized areas,
7. Pegmatite bodies (micas & base metals),
8. Basic dykes, silicified rocks and ultrabasic bodies (base metals),
9. Old mine workings (metallic deposits), Circular anomalies (indicating Kimberlite pipes for diamonds),
10. Drainage and vegetation anomalies,
11. Rock out crops, intrusive bodies and reactive rocks and

2.2.6.6 *Shear zone*

Crustal scale shear zones are fundamental discontinuities that often are the sites of continental accretion, collision extension and intraplate deformation. Such zones may accommodate deformation via simultaneous components of pure and simple shear. The distribution of strain in shear zones may vary spatially and also temporally and pure and simple shear deformation may be partitioned within the shear zone. Once formed shear zones are often zones of

weakness and may further deform by reactivation leading to complex polyphaser deformation histories.

The shear joints are filled with clay material and infilled few millimeters to few centimeters and the fractured zones are observed few centimeters to few meters with slicken sided planes (Rana *et al*, 2016).

2.2.6.7 *Gossan*

Gossan as defined by Jambor and Blowes (1994) is the name given to a large mass of residual Fe oxyhydroxide material formed by the oxidation of Fe-bearing sulfide ore deposits. Gossans are oxidized caps that form due to sulfide oxidation, dissolution, and precipitation of secondary minerals. Gossans are a type of iron-rich regolith that occur directly above a sulphide-rich orebody and can vary in thickness depending on the geometry of the orebody and degree of weathering. These iron oxide-rich gossan caps are formed from the oxidative weathering of primary metal sulphides (e.g. pyrite, chalcopyrite, pyrrhotite and arsenopyrite) by meteoric waters percolating through the near-surface environment (Haldar, 2018; Yesares *et al*., 2015). Meteoric waters are able to oxidize and leach soluble elements (e.g. Fe and S) from the orebody and reprecipitate some of them as secondary iron-bearing oxyhydroxides, oxides and oxy-sulphates (Velasco *et al*., 2013). These insoluble and iron-rich secondary minerals (e.g. goethite α-FeO(OH), hematite Fe2O3, jarosite KFe3(SO4)2(OH)6, melanterite FeSO4·7H2O and vivianite Fe3(PO4)2·8H2O) represent the dominant mineralogy within gossans and can exhibit a wide range of textures (Taylor,2011). Because gossans are found directly overlying sub-surface sulphide-bearing orebodies (Haldar, 2018; Velasco *et al*., 2013), they represent highly prospective exploration targets. The tracing of gossans as an exploration technique has been used since antiquity (e.g. the Romans in the Iberian Pyrite Belt; see Cruz *et al*., 2018) and is still highly relied upon in modern exploration. In fact, the

recent discovery of primary gold mineralization in the Amani area of SW Tanzania was aided by the occurrence of gossan outcrops along regional NW-SE trending shear zones (Dunn *et al.*, 2019).

The gossan mineralogy comprises goethite, hematite, malachite, azurite, siderite and quartz assemblages, with supergene gold particles up to 6 mm and with an average gold concentration of 95 wt %. Intersections of dipslip normal faults (NW-SE and N-S trends) are favorable sites for gossans to develop from their study area (Dunn and Von der Heyden, 2021).

According to Rekhibi *et al.*, 2015, gathering and analyzing all the criteria in the study area and studying the probability maps which the authors had produced, It is clear that gold and silver are present in outcrops bearing iron and quartize veins, alteration zones, dykes, and faults in area located north and east of Arkenu. Table 2.2 shows the mineral related anomaly, physical characteristics, chemical characteristics and the discriminative portion of Electro-magnectic spectrum. The presence of Gold mineralization in this area, maybe because of its concentration during regional transformation in quartize or its movement to the nearby veins and alteration zones (Fripp, 1979).

Table 2.2: The mineral related anomaly

S/N	Mineral Related Anomaly	Physical Characteristics	Chemical Characteristics	Discriminative Portion of EM spectrum
1	Gossan zones	Large mass of residual Fe. Intersection of dipslip normal fault are favourable sites for gossan.	Oxidation of Fe-bearing sulphide ore deposit Sulphide oxidation, dissolution and precipitation of secondary minerals	VNIR and SWIR (Band 2, band 4, band 5 and band 6) (Sherman and Waite 1985, Hunt and Ashley 1979, Hunt 1977)
2	Alteration zone	Metal concentrates in most intensely altered rocks(high fluid – rock ratio) High temperature Lowest PH	- Sericitisation - Oxidation - Sulphidation - Propylitization - Silification - Carbonitisation - Ammoniation (Nouri, 2015)	
3	Hydrothermal mineralization zone	Proximal to many precious and base metal deposit Distinguished from changes induced in rock by magmatic fluid Indicated by iron oxide, clay, carbonate, sulphate minerals	Archean greenstone belt Volcanogenic massive sulphide (VMS). Feritization Porphyries (Sillitoe, 2010)	Visible and near infrared (VNIR) and Shortwave infrared Region (Pour and Hashim, 2014).

4	Lineament intersection zones and Shear zone	Appear as straight lines or edges that may constitute tonal difference on the image		Landsat 8 band 8. (5,8,2 composite) better perception of contrast and land feature Edge enhancement and filtering technique.

Source: (Nouri, 2015)

2.2.7 Image spectral analysis

There are number of image analysis algorithms that have been developed to analyse the extensive information contained in hyperspectral imagery. Spectral analysis methods usually compare pixel spectra with a reference spectrum (often called a *target*). Reference spectra can be derived from a variety of sources, including spectral libraries, which are collections of reflectance spectra measured from materials of known composition, usually in the field or laboratory (Shippert, 2002). The spectral libraries for different minerals of interest can be generated from field measurements, to facilitate analysis of hyperspectral imagery from those sites. Several spectral libraries generated by USGS, JPL and many others are also available integrated with different image processing packages such as ERDAS IMAGINE, ENVI e.t.c (Shippert, 2002). Besides, remote sensing of heavy metal contamination relies on spectroscopic test results (Song *et al.,* 2015). The spectroscopic test provides valuable information on the spectral responses associated with heavy metal contamination, and thus, the test results give a band combination and spectral signatures useful for remote sensing approaches.

The visible-near infrared-shortwave infrared (VNIR-SWIR) spectral ranges (350 to 2500 nm) have been used to study the physicochemical properties of mineral objects and the associated environmental changes (Shin *et al.*, 2015; Shin *et al.*, 2016; Jeong *et al.*, 2016; Mohamed *et al.*, 2017). Lithological/Mineral identification capabilities are linked to available spectral information; e.g. capabilities increase from Landsat/Sentinel-2 to ASTER to hyperspectral imagery (Figure 2.4) (Mike, 2005).

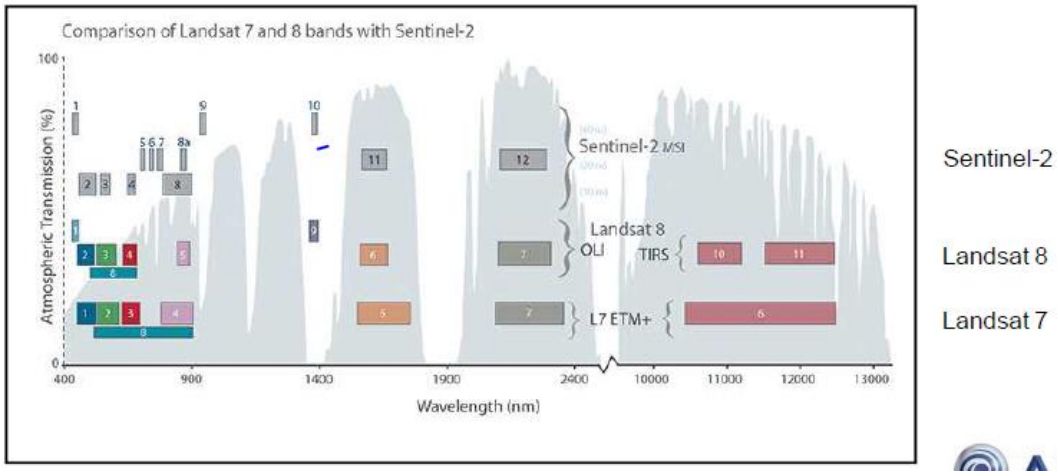

Figure 2.4: Comparison of Landsat and Sentinel sensors.
Source: (Mike, 2005).

2.3 Satellite Imageries for Lithology Mapping

Table 2.3 summarizes the history of the Landsat series of satellites (NASA, 2011). Over the years, Landsat enhanced the number of spectral bands and spatial resolution.

Table 2.3 Landsat systems, operational dates and sensors.

Landsat satellite	Launch	Decommissioned	Sensors	
Landsat-1	July 23, 1972	January 6, 1978	MSS (4 bands)	RBV (3 bands)
Landsat-2	January 22, 1975	February 5, 1982	MSS (4 bands)	RBV (3 bands)
Landsat-3	March 5, 1978	March 31, 1983	MSS (5 bands)	RBV (pan only)
Landsat-4	July 16, 1982	June, 2001	(TM (7 bands)	MSS (4 bands)
Landsat-5	March 1, 1984	2013	TM (7 bands)	MSS (4 bands)
Landsat-6	October 5, 1993	Failed to achieve orbit	ETM (8 bands)	
Landsat-7	April 15, 1999	Operational	ETM+ (8 bands)	
Landsat-8	February 11, 2013	Operational	OLI (9 bands)	TIRS (2 bands)

Source: (Markham and Helder, 2012)

These four Landsat instruments generations (MSS, TM, ETM+ and OLI (and TIRS) have different band designations. Landsat Multispectral Scanner (MSS) imagery consist in four spectral bands with 60 meters spatial resolution. Each image covers approximately an area of 170 km (north-south) by 185 km (east-west). Specific band designations differ from Landsat 1-3 to Landsat 4-5 (USGS, 2015d). Landsat Thematic Mapper (TM) images are composed by seven spectral bands with a spatial resolution of 30 meters for Bands 1 to 5 and 7 and for Band 6 (thermal infrared) is 120 meters, but is resampled to 30-meter pixels. Approximate scene size is 170 km (north-south) by 183 km (east-west) (USGS, 2015d).

Landsat Enhanced Thematic Mapper Plus (ETM+) imagery consists of eight spectral bands with a spatial resolution of 30 meters for Bands 1 to 7 and the Band 8 (panchromatic) resolution is 15 meters. Scene size is approximately 170 km (northsouth) by 183 km (east-west) (USGS, 2015d). On May, 2013 Landsat 8 Operational Land Imager (OLI) became available as well as Thermal Infrared Sensor (TIRS) imagery. This data consists of nine

spectral bands (Table 2.4) with a spatial resolution of 30 meters for Bands 1 to 7 and 9, and 15 meters resolution for Band 8 (panchromatic). New band 1 (ultra-blue) is useful for coastal and aerosol studies and new band 9 is useful for cirrus cloud detection. Bands 2-4 are visible bands whereas band 5 corresponds to near infrared (NIR). In addition, Band 6 and 7 correspond to shortwave infrared (SWIR) spectrum. Thermal bands 10 and 11 are useful in providing more accurate surface temperatures and are collected at 100 meters resolution. Approximate capture scene size is 170 km (north-south) by 183 km (east-west).

Table 2.4: Landsat 8 Operational Land Imager (OLI) and Thermal Infrared Sensor (TIRS) bands characteristics

Bands	Wavelength (micrometers)	Ground Sampling Distance (meter per pixel)
Band 1 – Coastal aerosol	0.43 - 0.45	30
Band 2 – Blue	0.45 - 0.51	30
Band 3 – Green	0.53 - 0.59	30
Band 4 – visible Red	0.64 - 0.67	30
Band 5 – Near Infrared (NIR)	0.85 - 0.88	30
Band 6 – SWIR 1	1.57 - 1.65	30
Band 7 – SWIR 2	2.11 - 2.29	30
Band 8 – Panchromatic	0.50 - 0.68	15
Band 9 – Cirrus	1.36 - 1.38	30
Band 10 – Thermal Infrared (TIRS) 1	10.60 - 11.19	100 * (30)
Band 11 – Thermal Infrared (TIRS) 2	11.50 - 12.51	100 * (30)

Source: (USGS, 2015d)

The Landsat 8 OLI image which has 9 spectral bands: 4 in the Visible (VIS) (0.43–0.67 mm), 1band of the Near Infrared (NIR) (0.85–0.88 mm), 2 bands of the Shortwave Infrared (SWIR) (1.57–2.29 mm), 1band of cirrus (1.36–1.38 mm) and a final band in the Panchromatic band

(0.50–0.68 mm) was used for the purpose of this research. The first 8bands have spatial resolution of 30m while the panchromatic band has a resolution of 15m. The Panchromatic band is usually used to resample the other bands to 15m. Out of these 9 bands, only 5 bands (3, 4, 5, 6, 7) were used in this study. Selection of the date of image acquisition was carefully considered to ensure "cloud-free" and "water-free" images. Gathering data in visible, SWIR regions have a particular interest for geological application (Rajesh, 2004; Mwaniki *et al.*, 2015; USGS, 2015a, b):

i. Band 7 (SWIR: 2.11-2.29 µm) – Coincides with absorption band caused by hydrous minerals (clay mica, some oxides, and sulfates) making them appear darker. Normally used in lithological mapping
ii. Band 6 (SWIR: 1.57-1.65 µm) – soil and rock discrimination: this band is sensitive to moisture variation in vegetation and soils; it is sensitive to presence of ferric iron or hematite rocks.
iii. Band 4 (Visible: 0.64-0.67µm) – discrimination of soil from vegetation: This band is good for discriminating soil and vegetation and delineating soil cover.

Given the presence of the blue band in Landsat data, Landsat images are more suitable for discrimination of iron oxide/hydroxide minerals, such as hematite, goethite and jarosite (Yousefi, 2018). The blue band of Landsat Thematic Mapper (TM), Enhanced Thematic Mapper Plus (ETM +) and Operational Land Imager (OLI) sensors is located in the absorption part of spectra for iron oxides, while the red band is associated with iron oxides' reflectance. Landsat images have been used for geological purposes by Elsayed Zeinelabdein and El-Nadi (Zeinelabdein *et al*, 2020). Landsat TM with seven spectral bands have been used for regional scales of geological mapping (Kargi, 2007). Landsat TM/ETM + image has

been used for detecting alteration mineral assemblages associated with epithermal gold and porphyry copper mineralization and lithological mapping applications. Shortwave infrared bands (bands 5 and 7) of TM/ETM + have been used as a tool to identify hydroxyl- bearing minerals in the reconnaissance stages of copper/gold exploration (Abdelsalam, 2000).

2.4 Lineament

Earth surface and subsurface fractures represented by lineaments play essential role in natural resources exploration and susceptibility hazard mapping of earthquakes/landslides (Rowland and Sibson, 2004; Masoud and Koike, 2006).

Lineament have been defined as natural crustal structures that may represent a zone of structural weakness (Walker, 2006). Lineaments may represent faults that control basin development and the distribution of reservoirs (Warner, 1997). Lineaments are linear features which provide information about the underlying geological structure (Andi *et al.,* 2017). Thus, accurate geological features mapping is a critical task for oil exploration, groundwater storage and understanding the mechanisms of environmental disasters (Maged and Mazlan 2010). Lineaments appear as linear tonal anomalies, linear vegetation anomalies or straight stream courses. Sudden and sharp shift or deviation of streams from their normal courses or displacement in the litho-units often indicates the lineaments/faults. Alignment of many water bodies in a straight line also may be because structural control (Krishnamurthy and Sreenivasan, 2005). Studies of linear geologic features (lineaments) of both local and regional significance, have been progressing rapidly (Abdullah *et al.,* 2010 a & b). Regional lineaments are commonly interpreted as surface expressions of geologic weak zones at tectonic boundaries of basins and plates, as well as of faults and rock fractures (Milbury *et al.,* 2007; Austin and Blenkinsop, 2008).

Many methods of automatic and semi-automatic extraction of lineaments from grid data such as satellite images and digital elevation models (DEMs) are mostly based on edge-detection techniques using spatial and morphological filters (Tripathi *et al.,* 2000; Soto-Pinto *et al.,* 2013).

Various methods are used for lineament extraction; image enhancement and manual digitizing techniques and automatic extraction using software and algorithms (Hashim, 2013; Rahnama and Gloaguen 2014; Scheiber *et al.,* 2015). Remote sensing and GIS approaches are increasingly used in mapping geological structures (Ahmad *et al.,* 2015; Cracknell, 2014; Meera *et al.,* 2014) and hydrogeological investigations.

The detection of lineament can be done using satellite imagery. There are two general methods of extracting lineaments from satellite imagery; the first involves manual digitizing of visually identified lineaments after image processing and the second is automated lineament extraction where the satellite image is subjected to automated processing by specifying different parameters such as curve length, linking distance, kernel size (Hung *et al.,* 2005; Andi *et al.,* 2017).

Frequency and connectivity of the lineaments are strongly affected by the scale of the source grid data and detection parameters when filters are applied (Argialas and Mavrantza, 2004). In Suzen and Toprak (2010), different lineament extraction technique including singleband (histogram equalization and stretching), multiband enhancement (principal component analysis) and spatial domain filtering (Prewitt and Sobel filters) were tested and also which they developed a new algorithm which consist of a combination of large smoothing filters and gradient filters in order to get rid of artificial lineaments and was realized that the combination of spatial domain filters is the most cost-time efficient algorithm in lineament

analyses. Also, in their work it was said that the first step in the evaluation of lineament is to recognize the drainage system of the region which will illustrate the major characteristics of topography, morphology and also to emphasis the impact of the faulting on the final geometry of the area.

The use of convectional edge detection filter techniques of lineament recognition has recently been criticized (Moreels and Smrekar, 2003) in which many linear features would be introduced that do not correspond to any geological element which increased the difficulty of lineament pattern interpretation. Satellite images and aerial photographs are extensively used to extract lineaments for different purposes. Since satellite images are obtained from varying wavelength intervals of the electromagnetic spectrum, they are considered to be a better tool to discriminate the lineaments and to produce better information than conventional aerial photographs (Casas *et. al*., 2000).

Satellite images representing reflectance and backscattering characteristics of the earth surface in response to electromagnetic waves at various wavelengths are generally used for lineament extraction. However, artificial linear features unrelated to fractures, such as boundaries of land use and land cover, also tend to be detected in satellite images. Precise DEM data can be used to avoid such misdetection. Results can be made more effective by the combined use of grid data from multiple sources that encompass wide compositional variations of subsurface geophysical attributes (e.g., gravity and magnetic) and depth variation represented by topography, especially when integrated at various scales. This can improve understanding of the relationship between tectonic trends and anomalies that develop at varying depths and geological discontinuities (Masoud and Koike, 2011a, 2011b).

In Taoufik *et al.,* 2016, road network, trails and the electric grid were digitized from the topographic map and the true color composite. They were superposed on the different photo-interpreted images to avoid their extraction as linear structures. False Color Composites (FCC) were realized to bring out more lineament's details. The quality of the extracted lineaments depends also on the spatial resolution of data used (Hung *et al.,* 2005). In this regard, band 8 was used in the RGB combination (5,8,2) which allowed a better perception of contrast and the distinction of land features. The overlaying of detected lineaments and the hydrographic network, digitized from the topographic map and Google Earth images, illustrates their spatial and directional relation (Taoufik *et al.,* 2016).

The concordance of some straight watercourses and lineaments show that they represent faults. Straight alignments of affluent will not occur unless they are following a faulted area (Sarala, 2012). Faults and tectonic movements reveal layers of tertiary marl, karstified limestone laying on soft sediments (Anonyme, 2002). In many landscapes, surface evidence of deformation can provide a tantalizing glimpse of the structures beneath the surface. For example, (Berberian, 1995) used the surface geometries and shapes of folds to infer the presence of master blind thrust faults at depth. (Cinque *et al.,* 1993) used geomorphological domains in addition to subsurface datasets to infer the geodynamic evolution of the Southern Apennines. Similarly, (Shephard-Thorn *et al.,* 1972) described the influence of the reactivation of basement faults on the structures of SE England.

These three diverse studies highlight the importance of surface observations and the tectonic inheritance concept in subsurface geology.

Burberry *et al.* (2018) used the shape of the land surface, as gleaned from satellite data and field-derived joint patterns, to understand the reactivation history of basement-involved faults in SE Nebraska and NE Kansas. Studies of specific structures (Gates and Costa, 1998;

Molliex *et al.*, 2010; Said *et al.*, 2011; Burberry and Mcmechan, 2012) indicate that subsequent structures, facies changes, and economic deposits may be affected by the motion of the pre-existing fault or faults. natural drainage systems display patterns of tributaries, run for long distances and are related in some fashion to the underlying geology.

According to Arlegui and Soriano (1998), normal faults are linear structures, and in the identification of lineament in their study in 1996 shows that the presence of fractures favored the development of different landforms (karst depressions, linear drainage network, straight scarps) in which lineament can be recognized. In their work because of the high number of lineaments found an automatic scanning program to determine different parameters of each one of the lines was used. It was concluded that most lineament in their zone of study correspond to normal faults and belong to one of the three distinct categories (single fault, several faults, several parallel faults) and also that lineament density has good correlation with shallow structure, gentle folding and sub surface information.

The surface features making up a lineament may be geomorphological, i.e. caused by relief or tonal, i.e. caused by contrast differences. Straight stream valleys and aligned segments of a valley are typical geomorphological expressions of lineaments (Hung *et al*, 2005). A tonal lineament may be a straight boundary between areas of contrasting tone. Differences in vegetation, moisture content, and soil or rock composition account for most tonal contrast (O'Leary *et al.*, 1976). In general, linear features are formed by edges, which are marked by subtle brightness differences in the image and may be difficult to recognize. On the earth, lineaments could be

1. straight stream and valley,
2. aligned surface depressions,

3. soil tonal changes,
4. alignments in vegetation
5. vegetation type and height changes
6. abrupt topographic changes.

All of these phenomena might be the result of structural phenomena such as faults, joint sets, folds, cracks or fractures. The old age of many geological lineaments means that younger sediments commonly cover them. When reactivation of these structures occurs, this results in arrays of brittle structures exposed on the surface topography. Similarly, the surface expression of a deep-seated lineament may be manifested as a broad zone of discrete lineaments (Richards, 2000).

Lineaments usually appear as straight lines or "edges" on the images which in all cases contributed by the tonal differences within the surface material. The knowledge and the experience of the user is the key point in the identification of the lineaments particularly to connect broken segments into a longer lineament (Wang *et al.,* 1990). From previous studies, one can conclude that lineaments usually occur as edges with tonal differences in satellite images and that most of the detection approaches are based on edge enhancement and filtering techniques (Mostafa and Bishta 2005; Fagbohun *et al.*, 2017; Pour and Hashim, 2014).

In order to map structurally significant lineaments, it is necessary first, by careful and critical analysis of the image, to identify and screen features not caused by faulting (Sabins, 1997). Hung *et al,* (2005) in their analysis shows that by overlaying the fault map of their study area on average length of lineament map, most of the faults are located very close to locations with high values of lineament density. The directions of the faults are corresponding with the directions of the high-density patterns.

In the extraction of lineament by Mathew and Ariffin (2018), lineaments are aftermaths effects of tectonic plays on geological terrane, fewer counts of lineaments almost always suggest less effects of tectonic activity on surrounding rocks. The results of lineament analysis gave a proper interpretation of the main structural geology and tectonic forces and suggest the area is profoundly affected by several structural trends N-S, NW-SE and E-W directions.

Lineaments reveal the architecture of the underlying rocks, which formed as a result of various tectonic (deformational) processes throughout the geological history of a region (Ramli *et al.*, 2010). In Javhar *et al.* (2019) it was noted that rivers sometime follow the geological structural elements but mostly are the result of erosion processes, which are not necessarily related to deformation. Therefore, it is important to evaluate the contribution of drainage-controlled extracted lineaments in the rose diagram directions of the lineaments.

In general, automatic lineament extraction methods are based on edge detection techniques that enhance the pixels at the edges on an image. This is followed by edge linking along pixels displaying similarities such as same edge geometry were used to find the best fit of a known shape. The Hough transform method is a very robust technique for identifying and linking edge pixels that corresponds to linear features (Cross, 1988). In Suzen and Toprak (2010), different lineament extraction technique including singleband (histogram equalization and stretching), multiband enhancement (principal component analysis) and spatial domain filtering (Prewitt and Sobel filters) were tested and also which they developed a new algorithm which consist of a combination of large smoothing filters and gradient filters in order to get rid of artificial lineaments and was realized that the combination of spatial domain filters is the most cost-time efficient algorithm in lineament analyses.

2.5 Previous Studies on Remote Sensing for Prospectivity Mapping

Optical imagery acquired by spaceborne and airborne sensors has been widely applied to mineral and lithological exploration for decades. For instance, the United States Geological Survey (USGS) used ASTER (Advanced Spaceborne Thermal Emission and Reflection Radiometer) data to map the hydrothermally altered rocks in the central and southern parts of the Basin and Range province of the United States (Mars, 2013). Due to its lower cost and higher accessibility than hyperspectral data, multispectral imagery, such as Landsat-5 TM, Landsat-7 ETM+ (enhanced thematic mapper plus), Landsat-8 OLI (operational land imager), and ASTER, is broadly utilized to extract lithologic, mineral, and structural information in metallogenic provinces (Pournamdari *et al.,* 2014; Asl *et al,* 2015; Masoumi *et al.,* 2017b). As one of the world's earliest and longest continuously acquired collection of spaceborne moderate-resolution land remote sensing data, the Landsat series has been applied in geology for decades (Francis and Rothery 1987; Demirkesen, 2009; Asl *et al,* 2015), for applications such as hydrothermal alteration (ferric iron and hydroxides) extraction, lithological discrimination, and geotectonic interpretation. With a higher spectral resolution in the shortwave infrared (SWIR) and thermal infrared (TIR) range than other multispectral data, ASTER provides a higher potential to undertake semi-quantitative mineral mapping.

It has become the most popular imagery in geological exploration, especially in hydrothermal alteration and lithological unit discrimination, since the Terra satellite was launched in 1999 (Pournamdari, *et al,* 2014; Tangestani, 2011). For example, Son *et al*. (2014) utilized ASTER data to map distribution patterns of hydrothermal alteration and igneous rocks in the southwestern Gobi in Mongolia.

Ninomiya and Fu (2016), applied ASTER TIR (thermal infrared) images to map regional lithological rocks in the Tibetan Plateau. However, with Landsat 7 being damaged in 2003 and Landsat 5 retiring in 2013, only Landsat 8, launched in 2013, remains within the Landsat mission for routine operation. Moreover, due to an anomalously high SWIR detector temperature, ASTER SWIR data have been unavailable since April 2008.

Thereafter, the Sentinel-2 mission, launched by the European Space Agency (ESA), acts as important data continuity and enhancement for the Earth observation. The Sentinel-2 Multi-Spectral Imager (MSI) consists of identical Senitnel-2A and Sentinel-2B, which were launched on 23 June 2015 and 7 March 2017, respectively. With a short revisit time (every 5 days with two satellites), the Sentinel-2 missions aimed at global monitoring for environment and security, such as forest monitoring, land cover change detection, and natural disaster management (Pesaresi *et al*, 2016; Navarro *et al*, 2017). In addition, the high-resolution Sentinel-2 multispectral data were confirmed to have potential for mineral mapping in geological investigations in the last several years, especially for the iron absorption feature, due to the similar or even higher spectral setting than Landsat series and SPOT in the VNIR region (Van der Meer *et al*, 2014; Christian *et al*, 2014; Van der Werff, and Van der Meer, 2015). However, there is rare research exploring the capability of Sentinel-2 data for complex lithological classification.

Although it is not new to use remote sensing technique for lithological classification in geological investigation (Masoumi *et al*, 2017a; Yu *et al*, 2012; Li *et al*, 2011), many studies are limited, due to the coarse spatial/spectral resolutions of multispectral data, causing difficulties in accurately classifying rock units (Yu *et al*, 2012). As a solution, multiple ancillary data with texture information, such as airborne geophysical data (Metelka, 2018),

DEM (De Boissieu, 2018), and geomorphic feature (Masoumi *et al*, 2017a), can be integrated with multispectral imagery for improved lithological classifications (Yu *et al,* 2012).

In (Ge *et al,* 2018), lithological classification was performed in the Shibanjing ophiolite complex in the Beishan orogenic belt in Inner Mongolia, China. The research aimed at investigating the potential of the Sentinel-2A and the integrations of multispectral imagery for lithological classification in the Shibanjing ophiolite complex. Specifically, (i) five typical machine learning methods, including artificial neural network (ANN), k-nearest neighbor (k-NN), maximum likelihood classification (MLC), random forest classifier (RFC), and support vector machine (SVM), were compared to select the optimal classifier for lithological classification using the data combination of Sentinel-2A and DEM (Sentinel-2A + DEM); (ii) three data combinations, OLI + DEM, ASTER + DEM, and Sentinel-2A + DEM, were employed to classify lithological units, which aimed to evaluate the capability of Sentinel-2A for lithological mapping; and (iii) two data combinations, OLI + ASTER + DEM and Sentinel-2A + ASTER + DEM, were utilized to compare the capability of different combinations of multispectral bands for lithological classification.

2.6 Principal Component Analysis

There are a significant number of image processing methods that have been developed during the past decades for detecting anomalous areas, such as hydrothermal alteration zones, using satellite images. Among these methods, dimensionality reduction or transformation techniques are known to be a robust type of methods, which are helpful, as they reduce the extent of a study area at the initial stage of mineral exploration. Principal component analysis (PCA), independent component analysis (ICA), and minimum noise fraction (MNF) are the dimensionality reduction techniques known as multivariate statistical methods that convert a

set of observed and correlated input variables into uncorrelated or independent components (Shirmard *et al*, 2020).

Principal Component Analysis (PCA) is a statistical method widely used in geological studies (Zhang, *et al.,* 2007; Gabr, *et al.*, 2010; Pour and Hashim, 2011a&b, 2012a&b; Amer *et al.*, 2012; Adiri *et al.*, 2016). It has the advantage of compressing the information contained in initial bands into new bands called Principal Components (PCs) (Gabr *et al.,* 2010; Adiri *et al.,* 2016). Consequently, this transformation eliminates the redundancy of data, isolates noise, and then enhances the targeted information in the image (Amer *et al.*, 2012).

The Principal Components Analysis (PCA) as a technique used to enhance and separate certain spectral signatures from the background (Gabr *et al.*, 2010, Moradi *et al*., 2015). PCA consists of a linear transformation applied on highly correlated multidimensional data like multispectral imagery which has a similar visual appearance for different bands, causing data redundancy (high correlation of spectral bands) (Loughlin, 1991). Thus, PCA analysis consists of a multivariate statistical technique that selects uncorrelated linear combinations (eigenvector loadings) of variables in such a way that each successively extracted linear combination, or Principal Component (PC) has a lower variance (Singh and Harrison, 1985). The number of output PCs is the same as the number of the input spectral bands.

The first Principal Component, PC1, contains most of the data variability, and highlights features common to all input bands and often display important structural information. PC1 corresponds to a vector in the direction of the maximum variance of pixels in the scene. The second PC, PC2, contains the second most data variability. It is orthogonal to PC1 in *n* directional space and highlights the spectral differences between visible and the infrared spectral bands. Third PC, PC3 includes the third most variability and is orthogonal to the other two PCs. The other PCs have less variability (Gabr *et al.*, 2010; Moradi *et al*., 2015).

This analysis has been successfully applied in Landsat images showing that the first three principal components may contain over 90 percentage of the information in the original seven bands (Fundamentals of Remote Sensing, 2012). These calculations have been widely used in remote sensing to classify the land surface (Jia and Richards, 1999) and detect changes (Eastman and Filk, 1993).

The PCs analysis can be used in a standard or selective method (Rajesh, 2004; Van der Meer et al., 2012). In a standard analysis, all the available spectral bands are used in the input for the PC calculation; in a selective analysis a PCA at selected input bands are applied. For enhancement of hydrothermal alteration zones, the bands with spectral characteristics of the dominant altered minerals in visible, NIR and SWIR regions of spectrum were selected (Rajesh, 2004; Van der Meer *et al*, 2012).

The feature-oriented PCs method (Loughlin, 1991) was used in order to enhance iron oxide and hydroxyl bearing areas. In this selective method, bands with spectral signatures for iron and hydroxyl bearing minerals was only used (Crosta and Rabelo, 1993; Rajesh, 2004; Van der Meer *et al.,* 2012). Iron oxides are a constituent of alteration zones associated with hydrothermal sulfide deposits and can be highlighted by band 4 / band 2 ratio (Sabins, 1999; Pour and Hashim, 2015). Hydroxyl bearing minerals are the most widespread product of alteration and correspond to a diversity of clays and sheet silicates, which contain Al-OH and MgOH bearing minerals and hydroxides in alteration zones. The band ratio 6/7 will highlight areas of altered zones comprising dominantly hydroxyl-bearing minerals (Sabins, 1999).

2.7 Extraction of Band Ratio

Digital image processing of remotely sensed data, especially by applying various enhancements through different image processing techniques like band combinations, filtering, ratioing, etc. can bring out additional information on geology, structures and alteration zones, which are important for mineral exploration (RRSSC, 2004). Band ratioing is a technique where digital numbers (brightness values) of one band are divided by that of another band. This corresponds to the peaks of high and low reflectance curve (Goetz *et al.*, 1983, Pour and Hashim, 2015). The digital enhancements involve a series of steps wherein the satellite data is processed through various algorithms to bring out better contrast and interpretability for extracting meaningful information from the images.

Band combination is the simplest type of digital image processing technique, wherein the satellite data obtained in different spectral bands is combined and displayed in the RGB plane. The selection of the best band combination out of the 'n' number of band combinations possible for a satellite data depends on the application and the features of interest. In most cases the, the best colour composite for mineral exploration is found to be with one of the band as SWIR or Mid Infra-Red (MIR). The enhanced color composite with a band combination of NIR, SWIR and Green (RGB:452 for IRS-1C/1D/P6 data) is found to bring out the contrast between lithounits, pediment zones, structural details and the circular anomalies more prominently.

Various contrast stretches such as linear, root, histogram equalization, etc. help in bringing out better contrast between different features in the image, which enhances the interpretability of the image (Jenson, 2000). Identical surface materials can give different brightness values because of the topographic slope and aspect, shadows, or seasonal changes

in sunlight illumination angle and intensity. These variances affect the viewer's interpretations and may lead to misguided results. Therefore, the band ratio operation could be able to transform the data without reducing the effects of such environmental condition. In addition, ratio operation may also provide unique information that is not available in any single band which is very useful for disintegrating the surface materials (Jensen, 1996). The band ratio images are known for enhancement of spectral contrasts among the bands considered in the ratio operation and have successfully been used in mapping of alteration zones (Segal, 1983). Various arithmetic combinations of the image bands are more useful for geological applications. The most useful of these combinations is the band ratio, which is simply dividing the digital number of a pixel in one band by that in another band. The ratios of different bands are useful in highlighting various features from the image. For example, the ratio of the two Mid Infrared (MIR) bands (band 5 and band 7 of Landsat TM) can bring out the hydrothermal altered zones; the ratio of Near Infrared (NIR) band and Red band can bring out vegetation anomalies.

The digitally enhanced color composites generated through the digital enhancement techniques discussed above are used for mapping of rock types, exposures, geomorohology and structural features, to delineate mineralized zones or source rock for mineralisation, extension of mineralized belts/formations, shear zones and the important faults, fractured zones, lineament intersections, anomalies and structures associated with mineral deposits, contacts between different rock types, mapping of alteration zones as indicator of mineralisation and various other mineralisation related anomalies using the various satellite image interpretation keys (Krishnamurthy and Sreenivasan, 2005). When using colour composites, the bands are selected based on spectral reflectance and the absorption features of the minerals or mineral assemblage to being mapped (Mateus and Frutuoso, 2015). Band

ratio technique was applied by Ghazali *et al.* (2015) to Arbaat area and a signature of alteration zone was detected.

Some authors refer the following band ratios for geological use, usually used to enhance lithological features (Sabins, 1999; Rajesh, 2004; Han and Nelson, 2015; Mwaniki *et al.*, 2015). Pour *et al*. (2019b) refer to a band ratio for identification of hydrothermal alteration minerals. The RGB image (4/2, 6/7, 5) was created to allow the identification of lithology, altered rocks and vegetation. With the same purpose, Kaufmann ratio (7/5; 5/4; 6/7) was also used (Ali and Pour, 2014).

Minerals such as alunite, and clay minerals such as illite, kaolinite and montmorillonite have distinctive absorption (low reflectance) features as ~2200nm and low absorption at ~1600 nm (Sabins,1999); iron oxides and sulphate minerals commonly have a strong reflectance near red and low blue reflectance (Figure 2.5) (Hans and Nelson, 2015). The ratio of Landsat 8 band 6 (1570 nm – 1650 nm) over band 7 (2110 – 2290) can be applied to distinguishes altered rocks containing clays and alunite from unaltered rocks. Areas with abundant iron minerals are shown with the ratio image of Landsat 8 OLI band 4 (640-670 nm) over band 2 (450-510 nm). (Sabins, 1999; Van der Meer *et al.*, 2012; Han and Nelson, 2015).

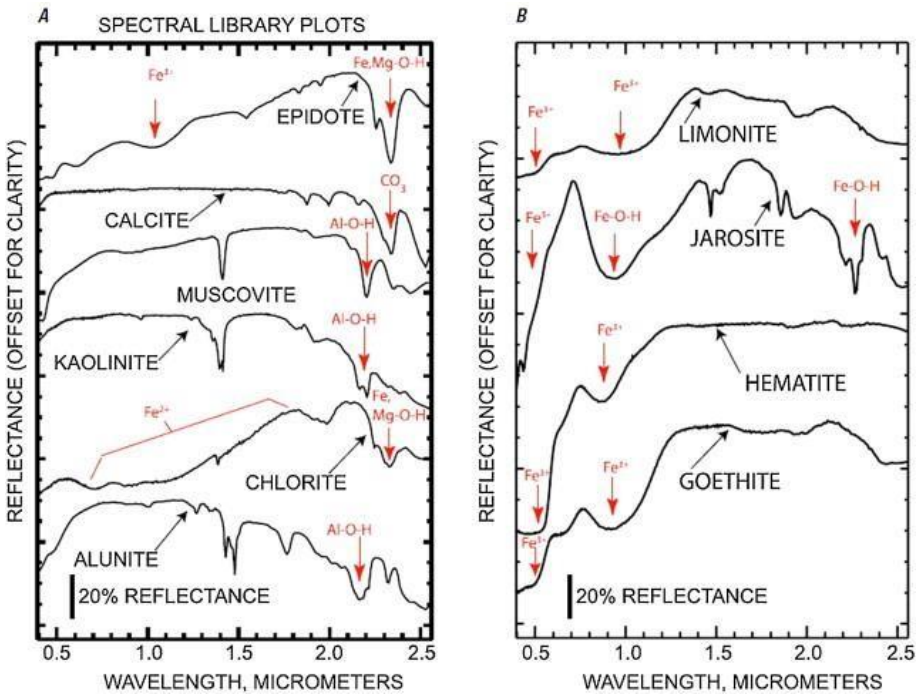

Figure 2.5: (A) Laboratory spectra of alunite, chlorite, kaolinite, muscovite, calcite, and epidote. (B) Laboratory spectra of limonite, jarosite, hematite and goethite (Clark et al., 1993).

Using the theoretical knowledge about the spectral properties of most rocks and minerals, TM bands 3/1 and 5/7 were selected for iron oxides and hydroxyl bearing mineral respectively. Whereas band ratio 5/4 has been computed to enhance possible ferrous oxides. Based on the above considerations the spectral features of ferric and hydroxyl – bearing mineral, in which hydrothermally altered rocks are often rich, are used to produce a false colour composite image using combinations of bands 5/7, 5/4 and 3/1 in R, G and B respectively. The obtained image has mapped the alteration zone in reddish yellow. This alteration can easily be observed in the lower right corner and right central part of the image. Another composite ratio image was produced using bands 5/7, 3/1 and 4/3 in R, G and B respectively. Although this combination of ratio image appears to be fairly different from the previous one, the final result remains the same thus lending support to the previous conclusion. Groundtruthing of the outlined areas of wall rock alterations has disclosed the

existence of a quartz stockwork that contains gold and base metal sulphide mineralization. Band ratio technique was applied and a signature of alteration zone in Yellowish color was detected. The gossan type of gold mineralization was successfully mapped in the Red Sea Hills of Sudan making use of Satellite imagery.

For identification of hydrothermal alteration minerals using Landsat-8 data, two band ratios have been developed based on laboratory spectra of alteration minerals. Mapping iron oxides will be carried out using bands 2 and 4 because iron oxide/hydroxide minerals such as hematite, jarosite and limonite have high reflectance within 0.63 to 0.69 μm (the equivalent to ETM+ band 3) and high absorption within 0.45 to 0.52 μm (the equivalent to ETM+ band 1). The analysis to map clay and carbonate minerals must incorporate bands 6 and 7 attributed to high reflectance in the range of 1.55 to 1.75 μm and high absorption in 2.08 to 2.35 μm that correspond with ETM+ bands 5 and 7, respectively.

2.8 Matrix Format of the Landsat Imagery

A Landsat image can be expressed in matrix format (Equation 2.11) in the following way:

$$X_{n,b} = \begin{pmatrix} \chi_{1,1} & \cdots & \chi_{1,n} \\ \vdots & \ddots & \vdots \\ \chi_{6,1} & \cdots & \chi_{6,n} \end{pmatrix} \qquad 2.11$$

where n represents the number of the pixels and b the number of bands (Estornell *et al*, 2013). Considering each band as a vector, the above matrix can be simplified as follows in equation 2.12:

$$X_k = \begin{pmatrix} \chi_1 \\ \chi_2 \\ \vdots \\ \chi_6 \end{pmatrix} \qquad 2.12$$

where k is the number of bands.

To reduce the dimensionality of the original bands the eigenvalues of the covariance matrix must be calculated (Estornell *et al*, 2013). This matrix can be calculated as follows in Equation 2.13:

$$C_{b,b} = \begin{pmatrix} \sigma 1,1 & \cdots & \sigma 1,6 \\ \vdots & \ddots & \vdots \\ \sigma 6,1 & \cdots & \sigma 6,6 \end{pmatrix} \quad 2.13$$

where σij (Equation 2.14) is the covariance of each pair of different bands.

$$\sigma_{i,j} = \frac{1}{N-1} \sum_{P=1}^{N} DN\mathrm{p,i} - \mu\mathrm{i}\ )\ (DN\mathrm{p,j} - \mu\mathrm{j}) \quad 2.14$$

where DNp,i is a digital number of a pixel p in the band i, DNp.j is a digital number of a pixel p in the band j, μ_i and μ_j are the averages of the DN for the bands i and j, respectively. From the variance-covariance matrix, the eigenvalues (λ) are calculated as the roots of the characteristic equation (Equation 2.15),

$$\det (C - \lambda I) = 0 \quad 2.15$$

where C is the covariance matrix of the bands and I is the diagonal identity matrix.

2.9 Principal Component Matrix Format of the Landsat Imagery

The eigenvalues indicate the original information that they retain. From these values the percentage of original variance explained by each principal component can be obtained calculating the ratio of each eigenvalue in relation to the sum of all them (Chuvieco, 2010). Those components which contain minimum variance and thus minimum information can be discarded. In remote sensing two bands located very close in the electromagnetic spectrum will have a high correlation (Estornell *et al*, 2013).

The principal components can be expressed (Equation 2.16) in matrix form:

$$Y6 = \begin{pmatrix} y_1 \\ y_2 \\ \vdots \\ y_6 \end{pmatrix} = \begin{pmatrix} W_{1,1} & \cdots & W_{1,6} \\ \vdots & \ddots & \vdots \\ W_{6,1} & \cdots & W_{6,6} \end{pmatrix} \begin{pmatrix} x_1 \\ x_2 \\ \vdots \\ x_6 \end{pmatrix} \quad 2.16$$

where Y is the vector of the principal components, W the transformation matrix, and X the vector of the original data. The coefficients of the transformation matrix W are the eigenvectors that diagonalizes the covariance matrix of the original bands. These values provide information on the relationship of the bands with each principal component. From these values it is possible to link a main component with a real variable. The eigenvectors can be calculated from the vector - matrix equation for each eigenvalue _k,

$$(C - \lambda_k I)w_k = 0 \quad 2.17$$

where C is the covariance matrix, λ_k is the k eigenvalues (six in our example), I is the diagonal identity matrix, and w_k is the k eigenvectors.

CHAPTER THREE

3.0 MATERIALS AND METHODS

3.1 Materials

3.1.1 Landsat data

The Landsat 8 OLI imagery of PATH 189 and ROW 53 was downloaded from the USGS site with "LC08_L1TP_189053_20180305_20180319_01_T1" production ID.

Table 3.1: Details of the metadata

Geographical area	Satellite mission	Date	Parameters
Madaka	Landsat 8OLI	05/03/2018	Path 189, Row 53

3.1.2 Geographic information system (GIS) software

GIS software was used for preprocessing, enhancement, to classify remote sense imagery and to extract spatial information. This is an effective tool for integration and for analysis of large amount of georeferenced spatial data with different formats and attributes. ArcMap 10.2 from ESRI, ENVI (Environment for Visualising Image) 5.3, PCI Geomatical 2015, were used (commercial software and open source software, respectively). Rajesh (2004) defines four steps to map mineral potential occurrence areas using GIS:

i. Build a database containing spatial digital data;

ii. Extract predictive evidence for a particular mineral deposit type;

iii. Calculate weights for each predictive evidence map;

iv. Combine the maps to predict mineral potential.

3.2 Methods

Several digital image processing methods were simultaneously utilized in order to achieve the research aim. The various methods and the basic rationale behind their utilization are presented in Figure 3.1 below;

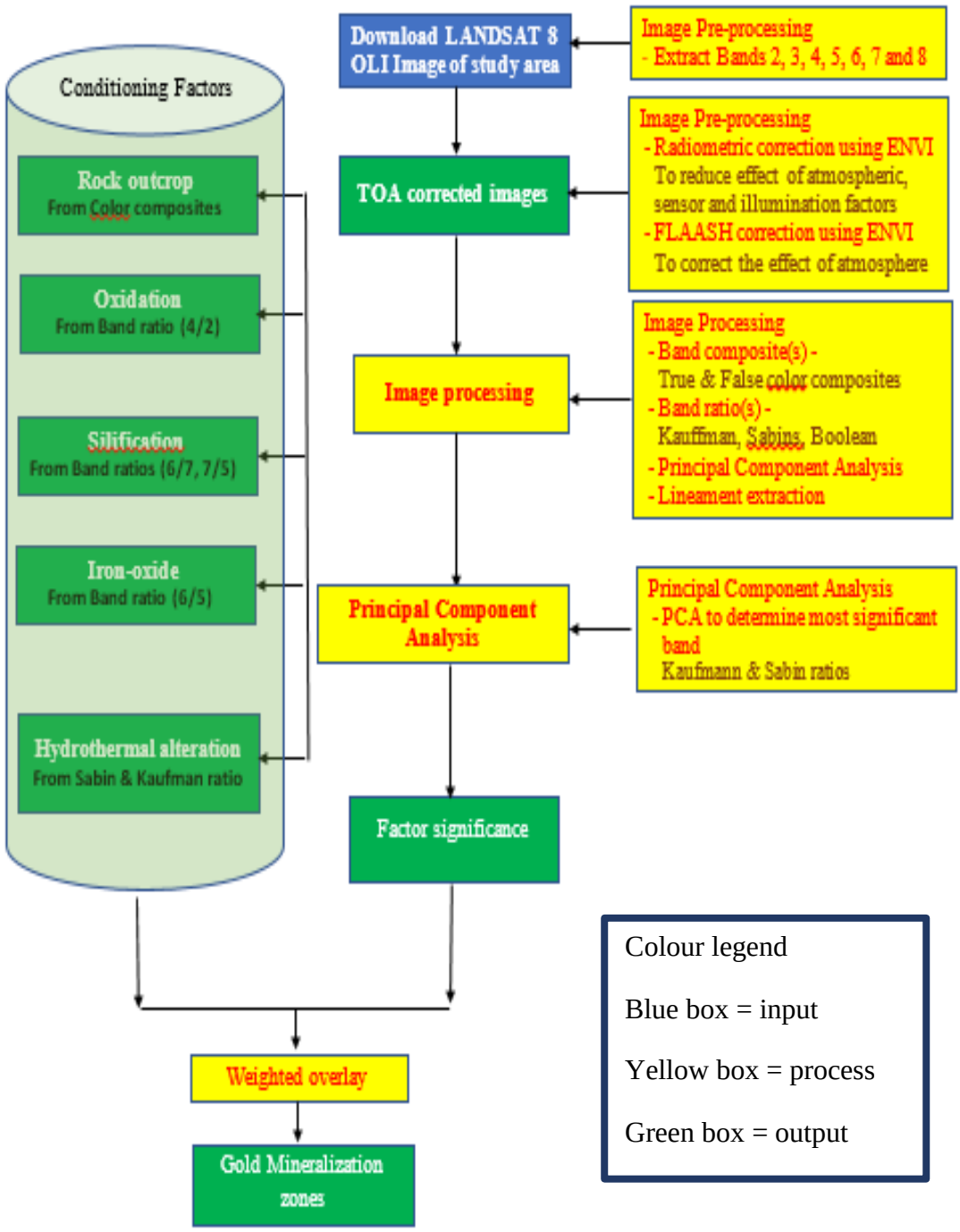

Figure 3.1: Workflow of methodology

3.2.1 Image pre-processing (Top of atmosphere correction TOA)

As already stated, for mineral exploration mapping, the most appropriated bands are located in the visible, NIR and SWIR regions. In this work, bands 2 to 7 from Landsat 8 OLI and the panchromatic (band 8) were used. This panchromatic band has a higher spatial resolution when compared with the multispectral bands, and was used for sharpening the image using it as a greyscale base image. The raw images were quantized and calibrated scaled Digital Numbers (DN). Radiometric calibration and the FLAASH (Fast-Line of sight Atmospheric Analysis of Spectral Hypercube) in Figure 3.2, corrections were applied to the imagery.

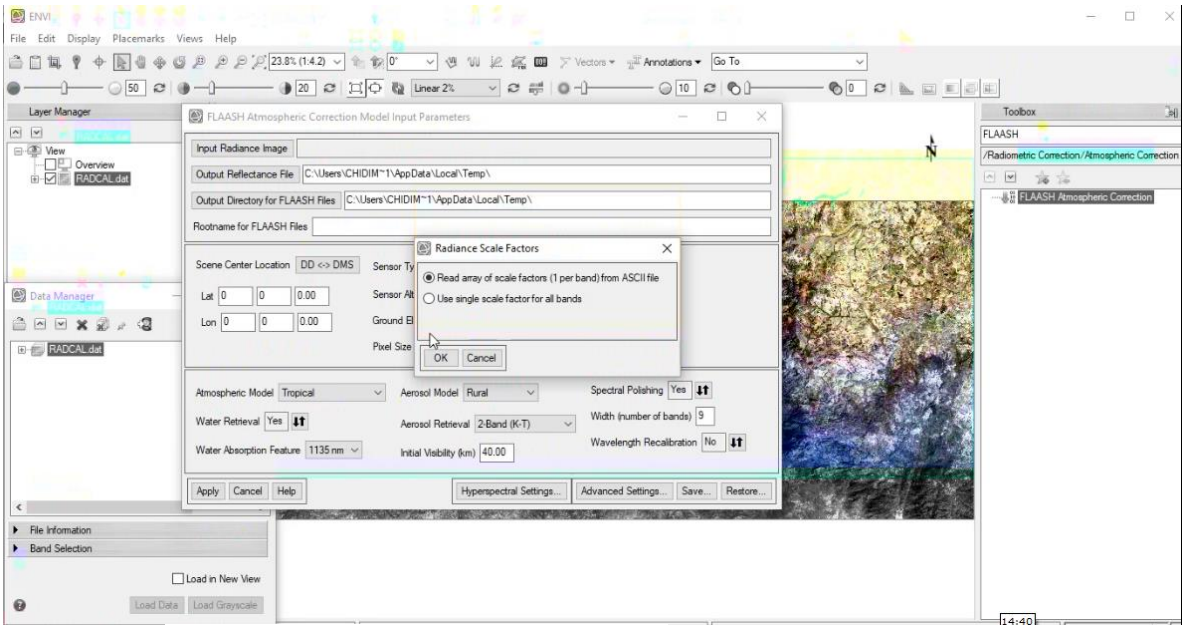

Figure 3.2: FLAASH correction

Usually, image enhancement is required for a better interpretation of the study area. This operation consists in a stretch imagery contrast to improve the information content of the image. According to Rajesh, (2004); Hung *et al.* (2005); Sukumarb *et al.* (2014), spatial filtering techniques provides better visualization, highlighting or suppressing some features of the image that allows to extract oriented features. This was used to filter the imageries

used in this research work based on spatial frequency, so rapid variations in brightness levels can indicate roughness and low spatial frequency smother areas.

Image sub-setting

After the image was downloaded and all the layers staked, in other to get our Region Of Interest (ROI), the entire image was subset by creating a shape file for the ROI on the Envi environment as in the figure 3.3.

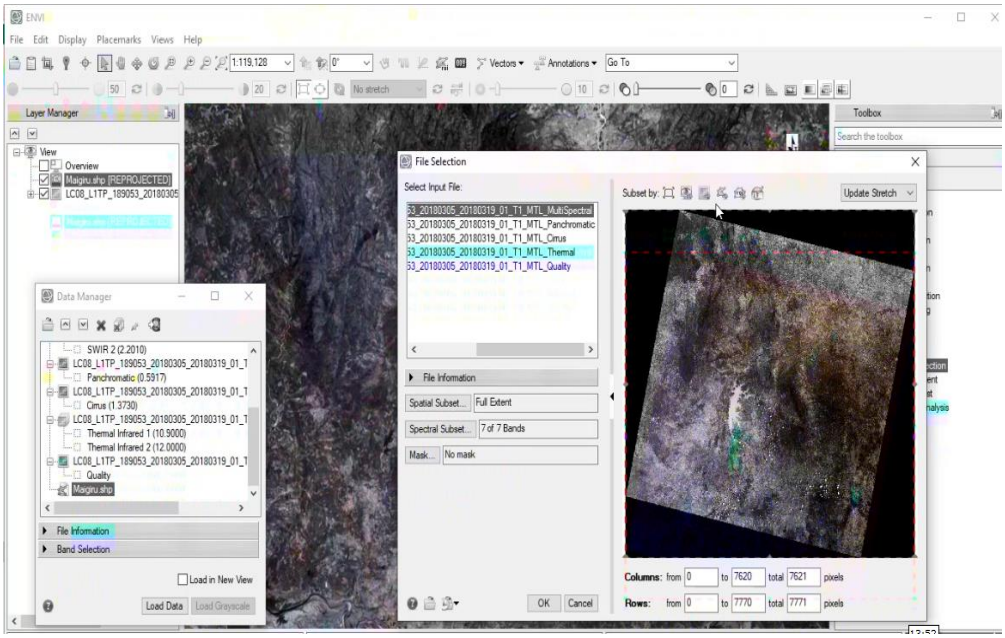

Figure 3.3: ROI subset

The data collected (geological data (lithology and structural), satellite data, topographical data (DEM) and mineral occurrence data) used in this study were spatially analyzed in way to generate a final target exploration map.

3.2.2 Image processing methods

The Image processing methods in this study was used to transform the multispectral satellite data into images that enhance geological features in contrast with the background. In this

study, enhancements techniques, such as Band composite (figure 3.4) carried out on the Envi environment, Band Rationing (figure 3.5), Principal Component Analysis (PCA) (Figure 3.6) and Lineament extraction (figure 3.7) were applied which allowed the extraction of spatial and spectral information related to lithology, structures, hydrothermal alteration, and others. These techniques allow to create a mineral potential map of gold mineralization occurrence and delineate mineral exploration targets for further work. Target delineation involves the analysis and integration of various thematic geological data.

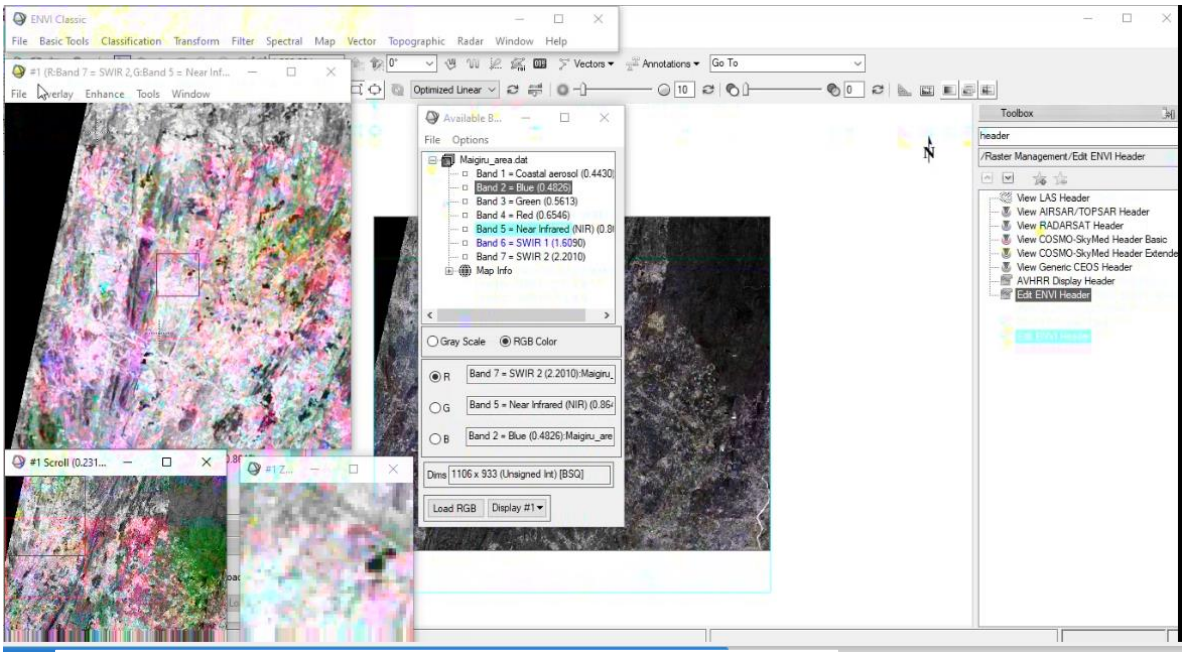

Figure 3.4: Band composting operation

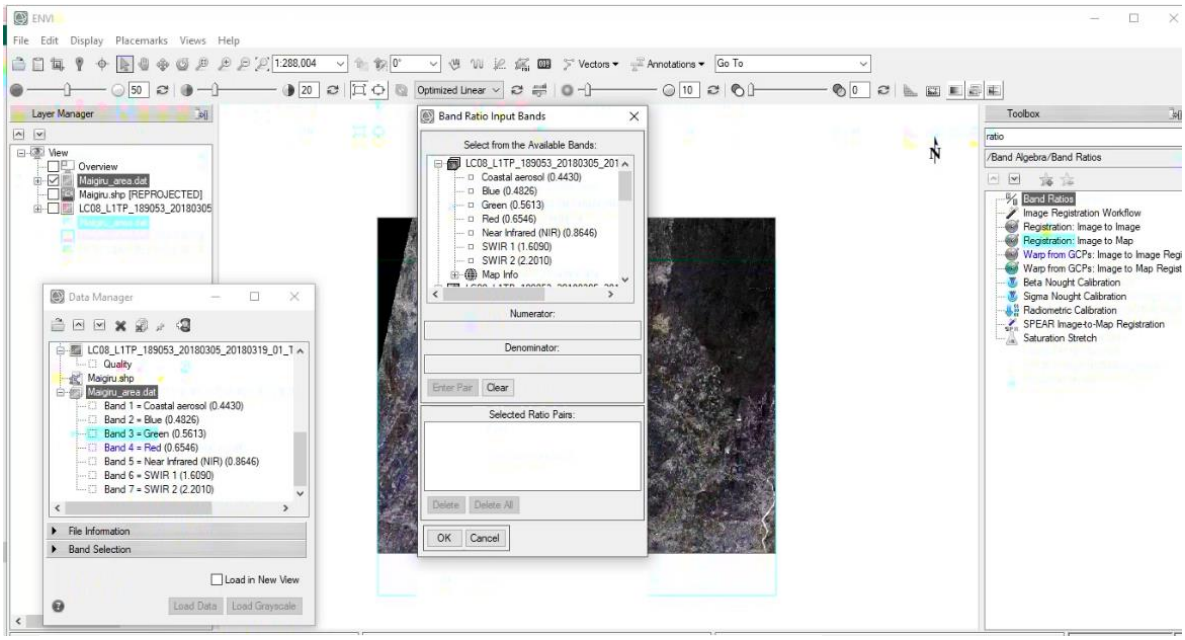

Figure 3.5: Band ratio operation

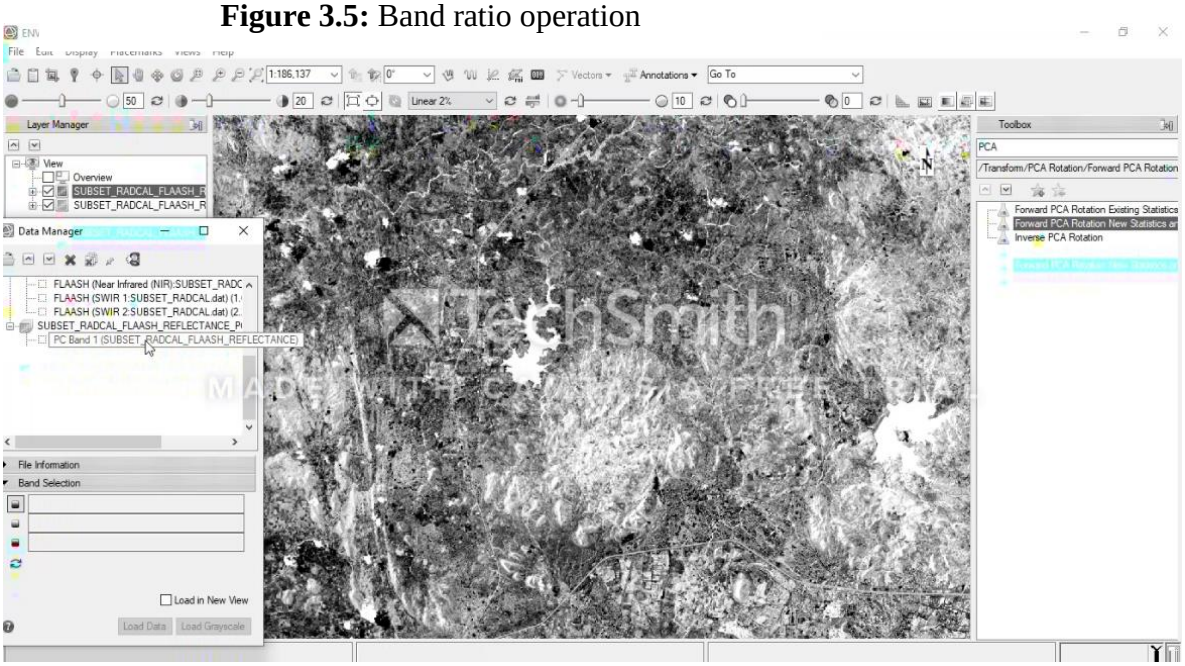

Figure 3.6: PCA operation

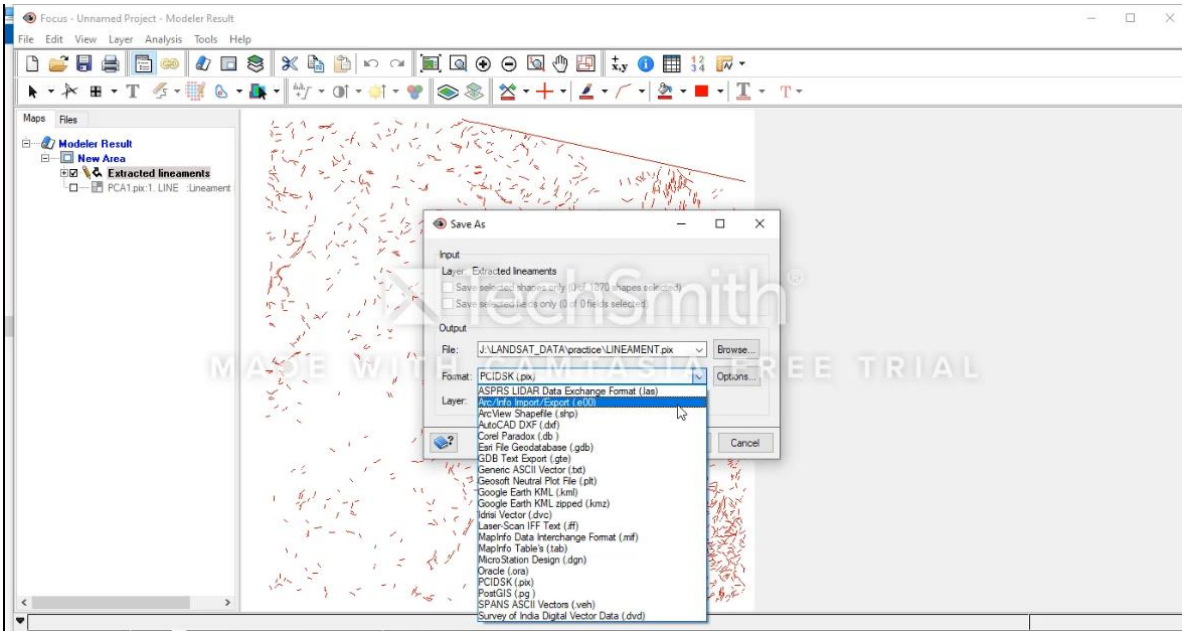

Figure 3.7: Lineament extraction operation

3.2.2.1 *Single band combinations*

The Landsat imagery used in this research is composed by grey-scale images correspondents to spectral bands. When a composite of three bands (red, green, and blue) is created a colourful multispectral image will result, which can be true colour or false colour (in this case, a NIR band is used instead of blue band). There are different band combinations possibilities whereby some of them enhance relevant features for mineral exploration.

A composite with the visible bands of the spectrum, that correspond to red, green and blue, called a true colour composite was used to generate a true colour composite image as in Figure 3.8, this was done on the ENVI environment. When a composite is created with non-visible bands it is called a false colour composite image (Mateus and Frutuoso, 2015). In the creation of the false colour image, the combination of three bands (visible bands and infrared bands or only infrared bands) in red, green and blue produced an image that enhance some characteristics depending the selected spectral bands. The bands are assigned based on

spectral properties of the rocks and alteration minerals which correspond to the work of Mateus and Frutuoso, 2015. Some band composites are useful in a first approach for mineral and rock discrimination and interpret possible alterations based in colour intensity variations, as RGB (7, 5, 2) or the RGB (5,6, 7).

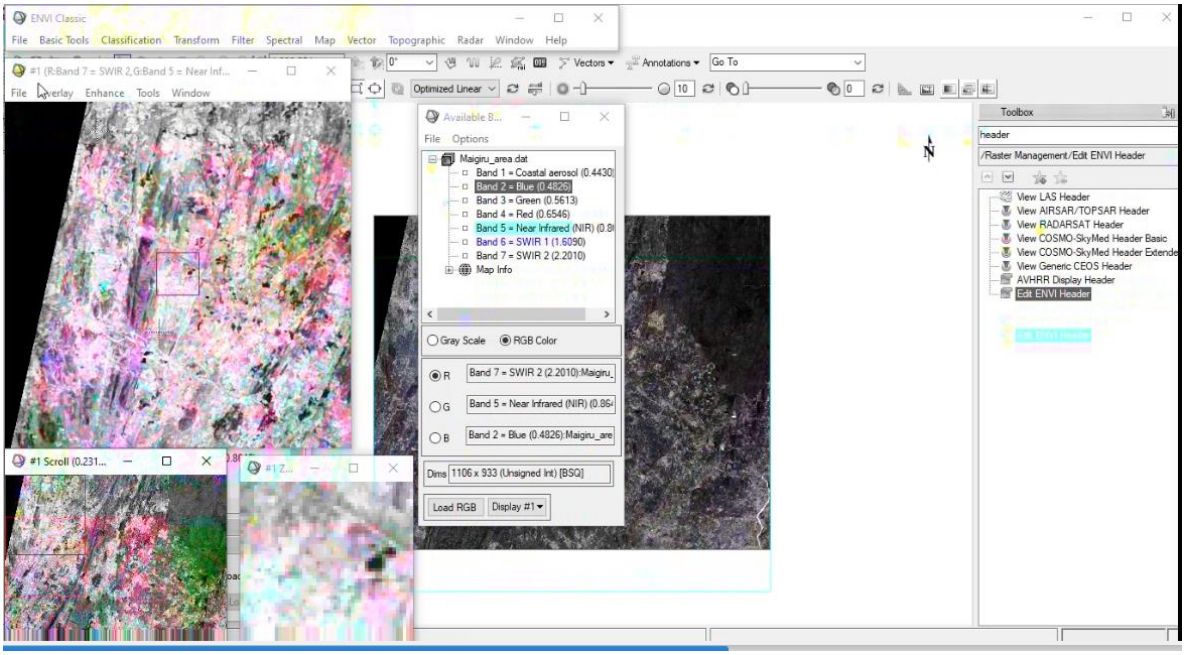

Figure 3.8: Band compositing operation

3.2.2.2 *Colour composite (CC)*

The Colour composites are various colour combinations that were done to enhance specific features in the image. A natural or true colour composite (TCC) of the image displayed a combination of the visible red, green and blue bands to the corresponding red, green and blue channels on the computer display. A TCC shows all features of an image in their true and natural colours. In most cases, due to spatial resolution, it is often very difficult to discriminate most features in TCC, hence a false colour composite was imposed to aid visual discrimination. The False colour composites (FCC) generated allowed us to visualize the wavelengths the human eye does not see (near the infrared range). False colour images are a

representation of a multispectral image created using ranges other than visible red, green and blue (RGB) components.

3.2.2.3 *Band ratio (BR)*

This technique was used to improve the contrast and enhance compositional information while suppressing useless information, like earth's surface and shadowing caused by topography surface shadow, allowing highlight some features that cannot be seen in raw data. Band ratios are very useful for highlighting certain features or materials that cannot be seen in the raw bands. It was based on highlighting the spectral differences that are unique to the materials being mapped.

Different band ratios were tested in this work Figure 3.9, in order to enhancing hydrothermally altered rocks and lithological units. The selection of bands were related to the spectral reflectance and position of the absorption bands of the mineral or assemblage of minerals to be mapped.

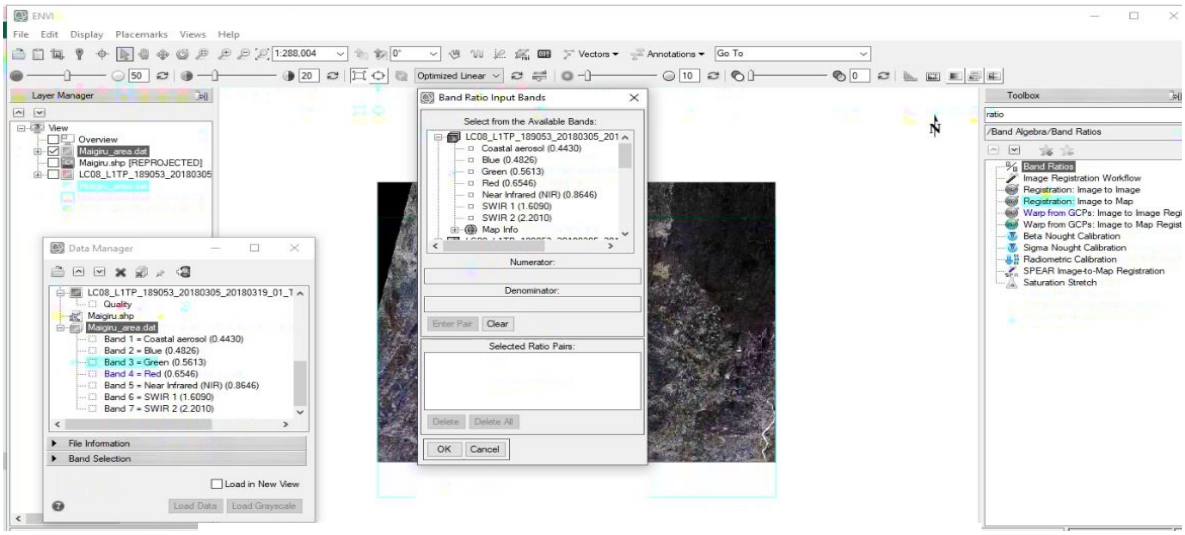

Figure 3.9: Band Ratio operation

Based on the spectral reflectance curve for hydrothermally altered rocks, BR was used to emphasize possible anomaly within the target thus leading to the identification of the specific

mineral features which was in accordance with San *et al.*, 2004; Nouri *et al*, 2012. Furthermore, BR was used to reduce the effect of topography, hence enhancing the difference between spectral responses of each band. The BRs and red–green–blue (RGB) color composite (CC) created with the Landsat 8 OLI images serve as basis for mineral detection (Mars and Rowan, 2010). The various BR used to execute this research is depicted in Table 3.3

Table 3.3: A serial arrangement of the Band Ratio used for Au

CC	BR	Interpretation		Reference
		Color	Mineral depicted	
TCC	4,3,2	Green	Vegetation	Welch and Ehlers 1987
		Brown	Soil / Rock outcrops	
		Blue	Water	Han and Nelson, 2015
FCC	5,6,7	Light blue	Outcrop	Zoheir *et al*, 2012a
		Black	Water	
		Orange	Vegetated Areas	
Boolean	4/2	Bright tone	Iron-oxide: Showing evidence of oxidation this tending towards hydrothermal alteration	Zoheir *et al*, 2012b
Boolean	6/7	Bright tone	Allunite and hydrothermal clay i.e hydroxl bearing rocks. Further showing evidence of hydrothermal alteration	Han and Nelson, 2015
Boolean	7/5	Bright tone	clay minerals (illite, kaolinite and montmorillonite). More evidence of hydrothermal alteration	Han and Nelson, 2015
Boolean	6/5	Bright tone	Ferrous minerals. Also serving as evidence of hydrothermal alteration	Mwaniki *et al*., 2015
Sabin's ratio	(4/2, 6/5)	6/7, Light green Light blue- yellow	Altered rocks Outcrop	Sabins, 1999
Kaufmann's ratio	(7/5, 6/7)	5/4, Red Dark green	Could be Hydrothermal alteration Metal sediments	Mia and Fujimitsu, 2012

Source: (Aransiola and Odumosu, 2021)

3.2.2.4 *Extraction of sub-lineament map*

For the purpose of this study, the LINE module of PCI GEOMATICAL was used on the first PC (Figure 3.7) band after the image was atmospherically and radiometrically corrected to generate a lineament map. The SRTM data of the study area was layer stacked with the lineament map uploaded in the ARCGIS environment to check for any correlation between the two maps.

3.2.3 Principal component analysis

The principal component (PC) analysis was carried out in the ArcMap environment first, on the entire Row and Path before sub-setting, which displayed the result in a grayscale thereafter, the ratios needed for alteration minerals were uploaded. In the activated classification tab on the ArcMap environment was displayed the principal component where the number of bands was inputted by adding them up one by one with the raster bands and the output location was saved at the output data file tab.

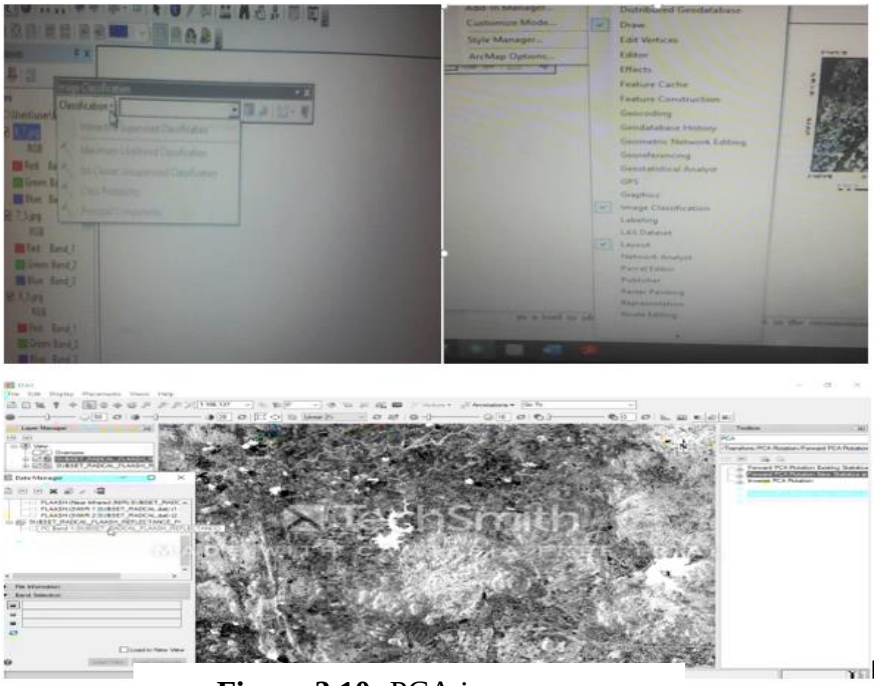

Figure 3.10: PCA in progress

PCS was performed on the Sabin's and Kaufmann's ratio in order to serve as an apriori weighting statistics based on the significance factor of the largest band contributor in both indices. Principle Component Analysis (PCA), de-correlates the data within each spectral band, such that the most common characteristics of all bands are placed in the highest category and lesser common characteristics are placed in lower categories, until all variance is explained (Odumosu *et al*, 2022). It is invaluable for exploration of data and landscape characteristics, simultaneously drawing attention to the most noteworthy and best-hidden features in a scene. Equation (3.1) is an expression of the mathematical formulation that implements PCA.

$$S = \sum i \sum j (Z_{ij} - X_i P_j)2 \quad (3.1)$$

Where: z_{ij} = original data, index i stands for the variable number and j for the observation number. p_j = the principal component which is used with a set of coefficients xi to approximate the jth observation of the ith variable z_{ij} as $x_i p_j$. The values of the $x_{i'}$s and the p_j are to be chosen so as to minimize the sum of the squared deviations between the actual data.

3.2.4 Multi-criterial analysis

Two weighted overlay operation scenarios were performed within ArcMAP 10.2 using the conditioning factors for oxidation, silification, iron oxide and hydrothermal alteration. For oxidation, Tarnish in gold results from a reaction to oxygen with the air which can be well observed in bands 4 and 2 (4/2). For silification, when rock have contact with groundwater, the extra dissolved silicon dioxide in the groundwater will deposit in the rock pores and result in an increase in the rock's silicon amount. This explains the close association of silification

and gold mineralization. Being a metallic luster, the condition for silification responded in bands (6/7) and (7/5).

For iron oxide, is a reddish-brown solid that can be identified in bands 6 and 5. The Boolean maps were also re-classified based on the variation in the grey scale values using the re-class tool in ArcGIS. The nearest neighbor classification method was used for the classification with the areas corresponding to suspected gold mineralization taken as the high gold mineralization zones as shown in Table 3.4.

Table 3.4: Weighting criteria for weighted overlay analysis

S/No	Conditioning factor	Scenario 1	Scenario 2	Remarks
		Assigned weight (%)		
1	TCC (Rock outcrop)	10	6	
2	FCC (Rock outcrop)	10	6	
3	Oxidation	20	12	
4	Boolean (6/7) silification	10	6	
5	Boolean (7/5) silification	10	6	
6	Iron oxide	20	12	
7	Sabins (hydrothermal alteration)	10	32	Has highest PCA
8	Kaufmann (hydrothermal alteration)	10	20	
		100	100	

CHAPTER FOUR

4.0 RESULTS AND DISCUSSION

4.1 Presentation of Results

The results obtained are presented in the order of various zones/regions identified within he study area. The results are presented as follows;

4.1.1 Regions of Hydrothermal Alterations

The regions with the hydrothermal alterations as derived from various ratios are presented below Figure 4.1; (a) shows the ratio of band 4/2, (b), the ratio of band 6/5, (c), ratio 7/5, (d), displays the ratio of 6/7 and (e), band ratio of 7/6. All in dark and bright pixels.

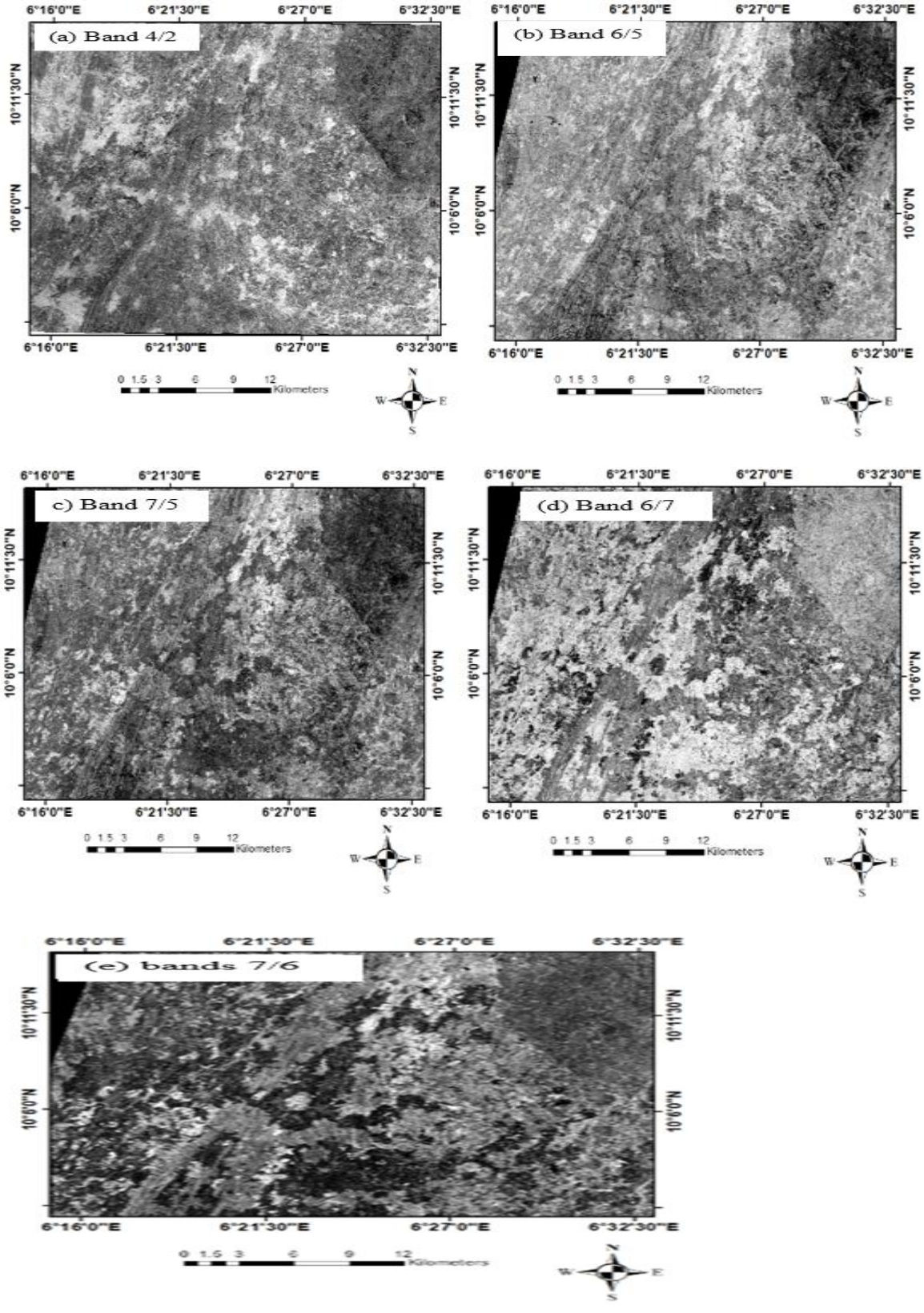

Figure 4.1: Hydrothermal Alteration Mappings: (a) band ratio 4/2 (b)band ratio 6/5 (c) band ratio 7/5 (d) band ratio 6/7 (e) band ratio 7/6

This corresponds directly to minerals associated with this alteration and represents surface expression for auriferous deposits. Thus, it was applied the ratio of Landsat 8 OLI band 4 over band 2, to highlight areas with abundant iron oxides bearing minerals, as brighter pixels (Figure 4.1 (a)). Ratio of Band 6 over band 5 discriminate ferrous minerals in bright tone (Figure 4.1 (b)). Clay minerals, as illite, kaolinite, and montmorillonite are discriminated with the ratio image of band 7 over band 5 as bright pixels (Figure 4.1 (c)). The ratio image of band 6 over band 7 distinguish altered rocks containing clays and alunite from unaltered rocks, where pixels are bright (Figure 4.1 (d)). The spectral value in the image can determine the iron oxide value in wetlands (Demattê *et al*., 2017). Iron oxide research using remote sensing is mostly carried out in dryland with low vegetation cover and mining areas (Arisanty *et al*., 2021).

4.1.2 Band combination response for hydrothermally altered rocks

The natural representation of the study area as it is when in Red Green Blue (RGB) is displayed in the Figure 4.3 below, in the visible spectrum region of the Landsat imagery used. Figure 4.4 expresses the false colour combination of bands 5,4,3, Figure 4.5, shows the RGB combination for bands 7,5,2, figure 4.6, illustrates the Sabins ratios (4/2, 6/7, 6/5), Figure 4.7 demonstrates Kaufmann ratio (7/5, 5/4, 6/7) respectively and Figure 4.8 shows the summary of the band combinations.

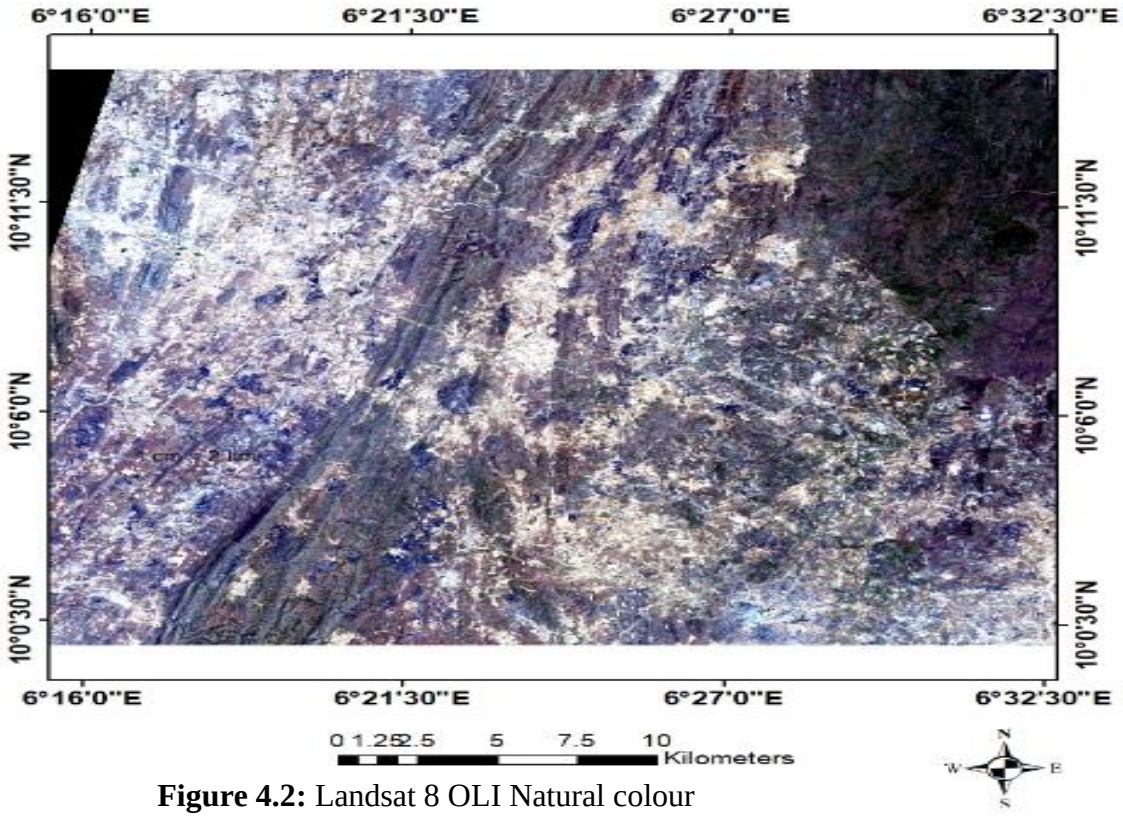

Figure 4.2: Landsat 8 OLI Natural colour

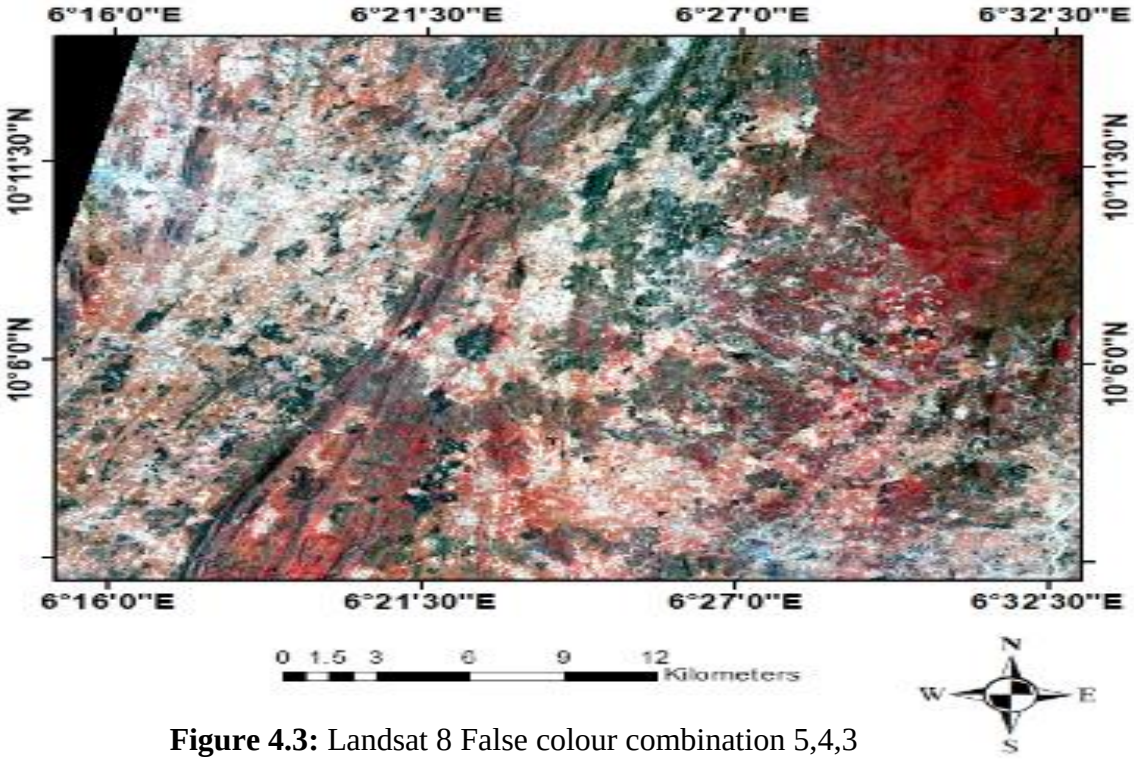

Figure 4.3: Landsat 8 False colour combination 5,4,3

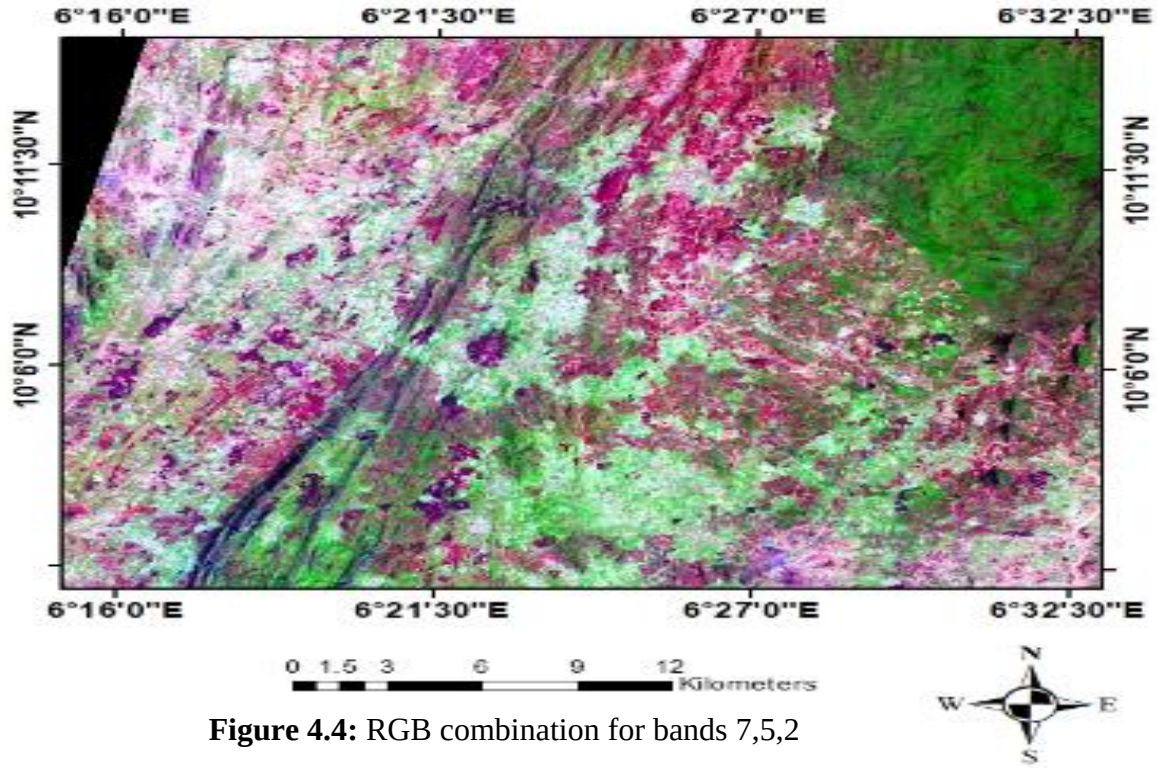

Figure 4.4: RGB combination for bands 7,5,2

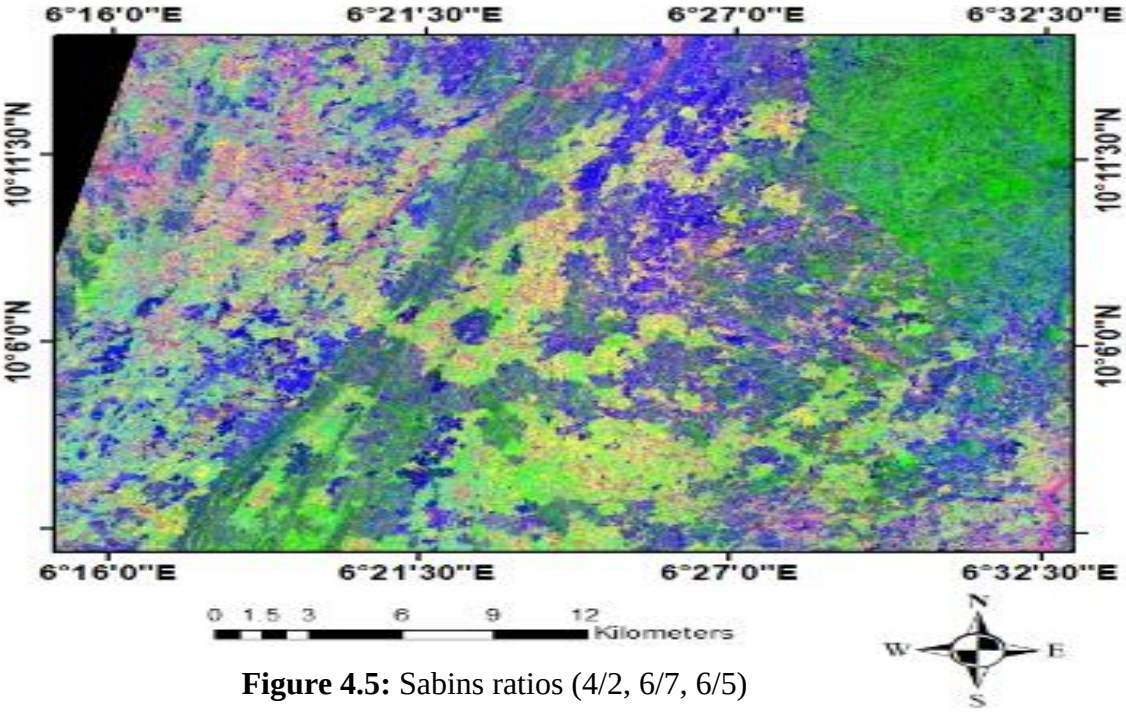

Figure 4.5: Sabins ratios (4/2, 6/7, 6/5)

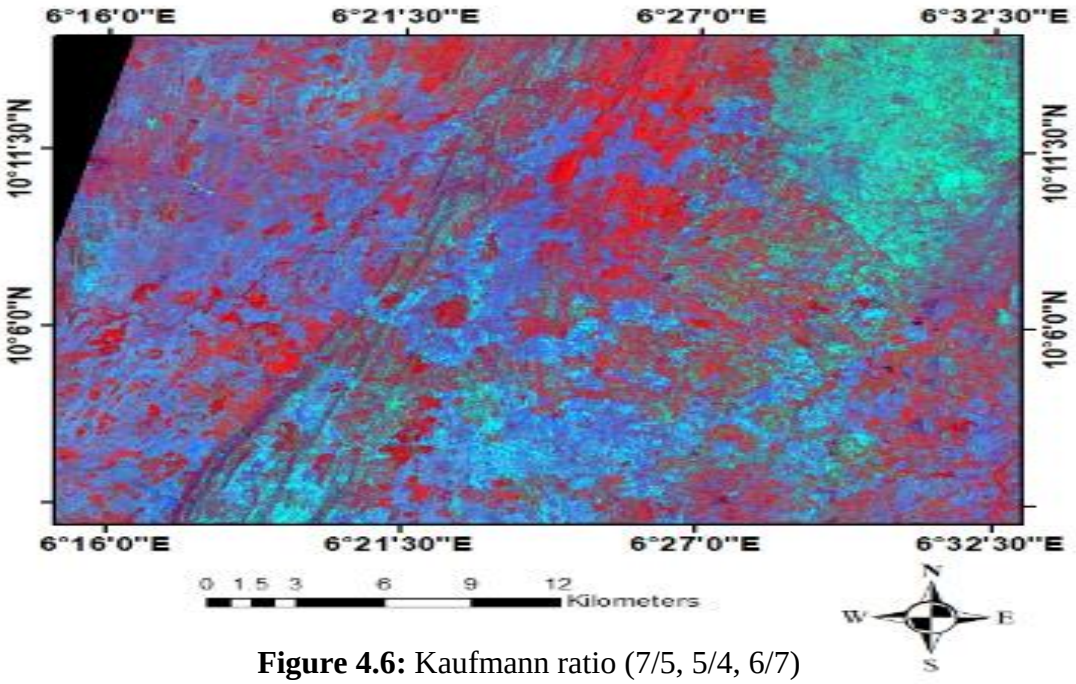

Figure 4.6: Kaufmann ratio (7/5, 5/4, 6/7)

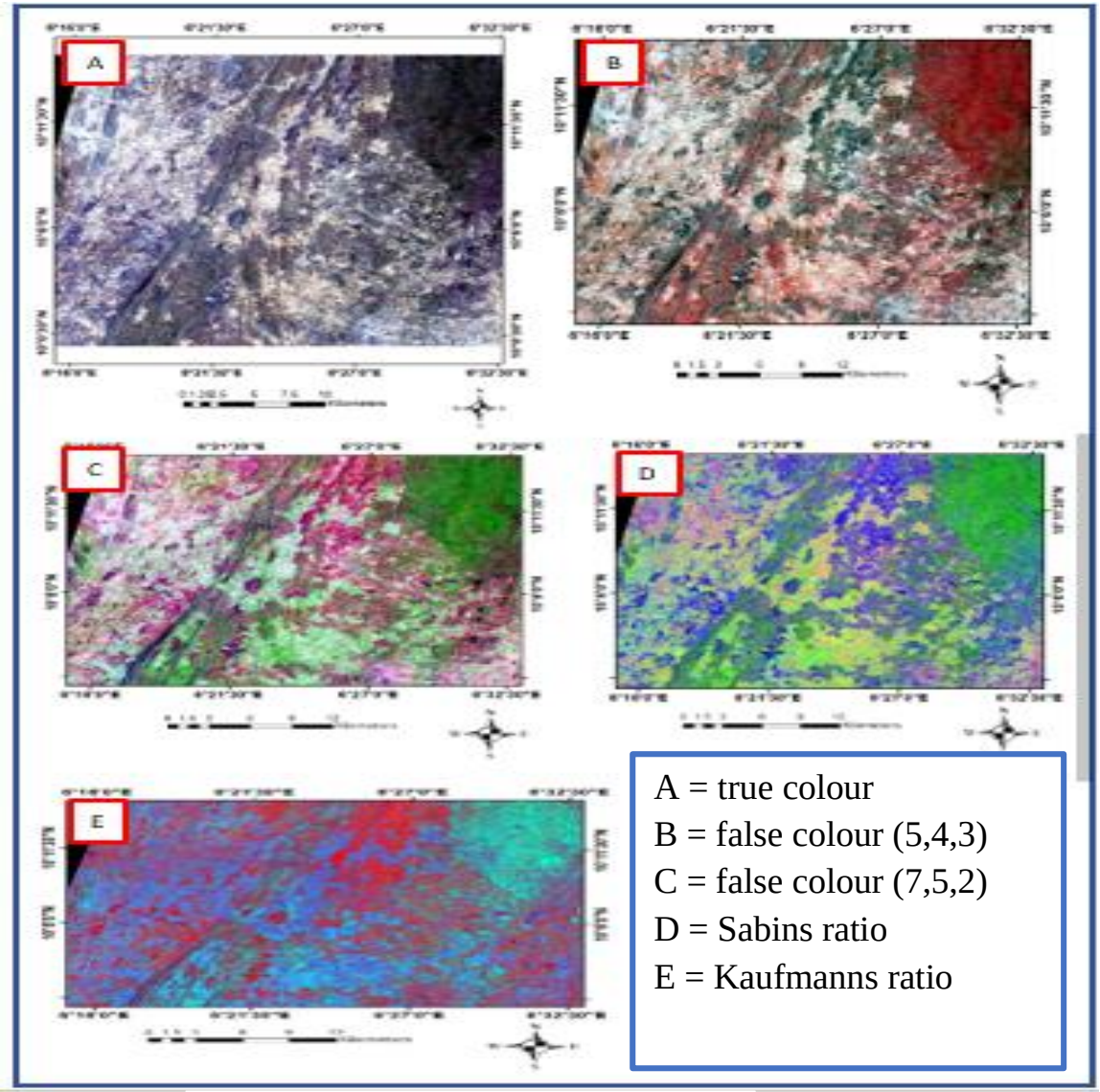

Figure 4.7: Figure 4.2 to 4.6 summary

4.1.3 Principal Component Analysis and Sub Surface Lineament

4.1.3.1 *Presentation of PCA results*

The Principal Component Analysis for the selected Landsat 8 band used that shows the spectral response of relevant substances and the spectral information of minerals as displayed in Figure 4.9, Figure 4.10 A-D display the various PCA of the ratios of (5,4,3), (7,5,2), Kaufmanns, Sabins respectively.

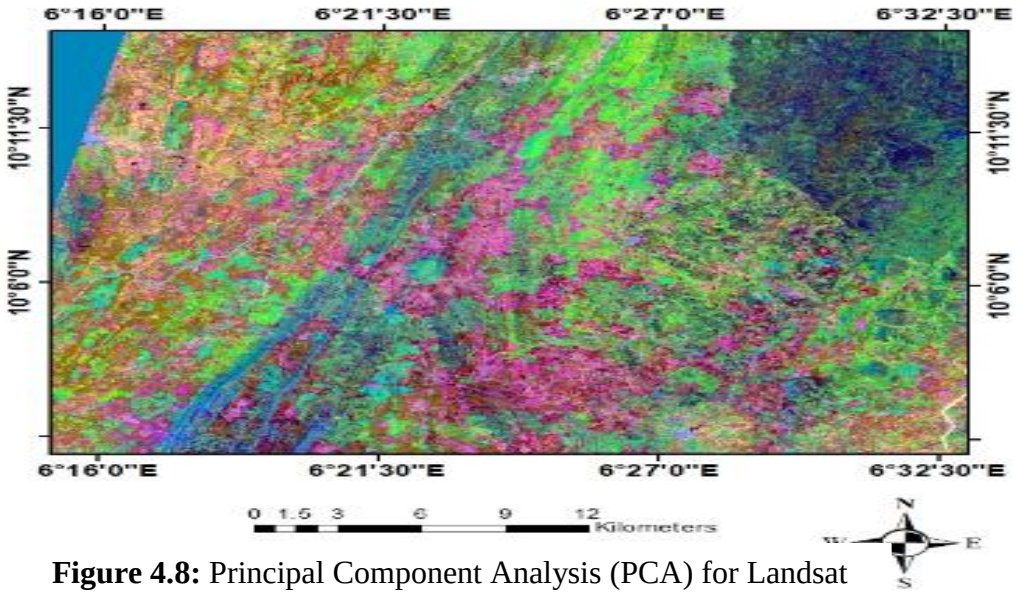

Figure 4.8: Principal Component Analysis (PCA) for Landsat band used

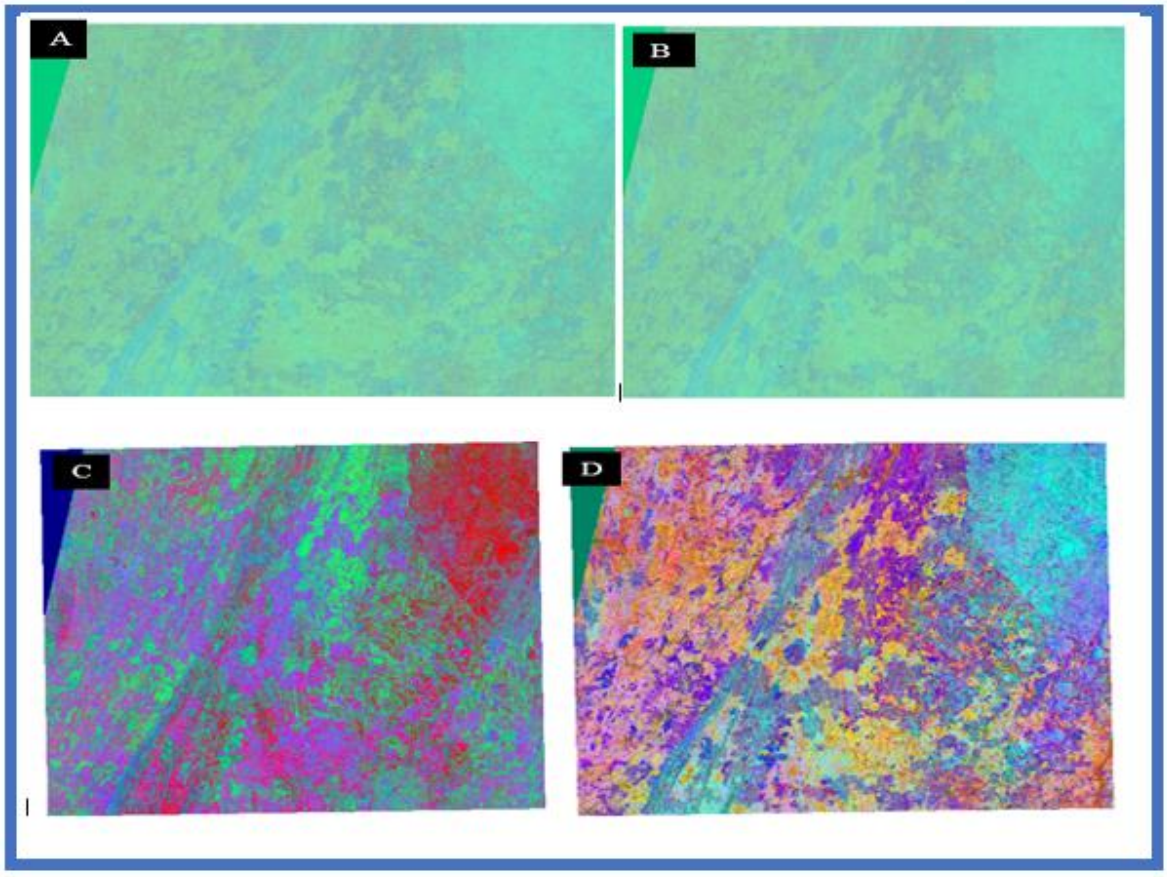

Figure 4.9: PCA for (A) 5,4,3 (B) 7,5,2 (C) Kaufmanns (D) Sabins respectively

Table 4.1 illustrates the 1.00000 along the diagonal, the first to sixth column shows the PCA for each band used. This summarizes the correlation matrix for the six bands used as displayed below;

Table 4.1: The Correlation matrix of Principal Component Analysis (PCA) for bands 2,3,4,5,6,7 of Landsat used.

Layer	1	2	3	4	5	6
2	1.00000	0.99771	0.98847	0.98297	0.97647	0.97275
3	0.99771	1.00000	0.99534	0.98273	0.97986	0.97727
4	0.98847	0.99534	1.00000	0.97830	0.98669	0.98551
5	0.98297	0.98273	0.97830	1.00000	0.98201	0.96833
6	0.97647	0.97986	0.98669	0.98201	1.00000	0.99502
7	0.97275	0.97727	0.98551	0.96833	0.99502	1.00000

For PCA 1, band 6 has the highest value with 0.54479 and band 2 with 0.29787, PCA 2, band 5 with the highest and band 7 with the lowest, PCA 3 has band 3 with high and band 5 lowest, same apply with PCA (4-6) with highest and lowest respectively as shown in Table 4.2.

Table 4.2: Principal component 1,2,3,4,5,6 for the input band1,2,3,4,5,6 which are the eigen vector

Eigen vector	PCA 1	PCA 2	PCA 3	PCA 4	PCA 5	PCA 6
Band 2	0.29787	0.30273	0.42114	0.56653	0.32721	0.46286
Band 3	0.29978	0.23358	0.46422	0.00034	0.04299	-0.79889
Band 4	0.33028	0.01747	0.43746	-0.73395	-0.14012	0.37539
Band 5	0.47610	0.61633	-0.53980	-0.01780	-0.31777	0.02808
Band 6	0.54479	-0.39210	-0.34337	-0.12950	0.63961	-0.07538
Band 7	0.43458	-0.56558	0.08047	0.35110	-0.60114	0.01227

The EV and EV are presented below (Table 4.3), the columns identify the 6 PC layers while the row displays the EV and EV gotten from the bands of the imagery used. This summarizes the values gotten from the EV and EV.

Table 4.3: Eigenvalues and eigenvectors (EV & EV) for the Landsat bands used

Pc layer	1	2	3	4	5	6
EV & EV	257878606.86135	2134108.02539	1161104.70861	220660.40312	132762.67796	8196.48149
Band						
2	0.29787	0.30273	0.42114	0.56653	0.32721	0.46286
3	0.29978	0.23358	0.46422	0.00034	0.04299	-0.79889
4	0.33028	0.01747	0.43746	-0.73395	-0.14012	0.37539
5	0.47610	0.61633	-0.53980	-0.01780	-0.31777	0.02808
6	0.54479	-0.39210	-0.34337	-0.12950	0.63961	-0.07538
7	0.43458	-0.56558	0.08047	0.35110	-0.60114	0.01227

Here (Table 4.4), the first column gives the PC layer information from 1-6, the second column presents the EV, the third column the percent of EV and the last, the accumulated EV. This summarizes all the figures derived from the above mentioned.

Table 4.4: Percent and accumulative eigenvalues for the Landsat bands used

Pc layer	Eigenvalue	Percent of Eigenvalues	Accumulative of Eigenvalues
1	257878606.86135	98.6018	98.6018
2	2134108.02539	0.8160	99.4178
3	1161104.70861	0.4440	99.8617
4	220660.40312	0.0844	99.9461
5	132762.67796	0.0508	99.9969
6	8196.48149	0.0031	100.0000

The covariance matrix is shown in Table 4.5 in which the column signifies the layer of the PC for Sabins ratio while the row, the layer for the bands. This abridges the values derived from the covariance computation.

Table 4.5: Covariance matrix for Sabins PCA

Layer	1	2	3
1	0.02784	0.02909	0.02531
2	0.02909	0.03925	0.02374
3	0.02531	0.02374	0.03641

The Correlation matrix is shown in Table 4.6 in which the column signifies the layer of the PC for Sabins ratio while the row, the layer for the bands. This abridges the values derived from the Correlation matrix computation

Table 4.6: Correlation matrix for Sabins ratio PCA

Layer	1	2	3
1	1.00000	0.87988	0.79506
2	0.87988	1.00000	0.62789
3	0.79506	0.62789	1.00000

The first column from the table below illustrates the PC layer, the second column shows the Eigenvalue, the third column displays the percent of Eigen value and the last represents the accumulative of Eigen value all for Sabins ratio. This table summarizes the percent and the accumulative eigenvalues for Sabins ratio as presented in Table 4.7 below;

Table 4.7: Percent and accumulative eigenvalues for Sabins ratio

Pc layer	Eigenvalue	Percent of eigenvalue	Accumulative of eigenvalues
1	0.08680	83.8641	83.8641
2	0.01414	13.7022	97.5663
3	0.00252	2.4337	100.0000

The covariance matrix for Kaufmann ratio is shown in Table 4.8 below in which the column signifies the layer of the PC for Kaufmann ratio while the row, the layer for the bands. This summarizes the values derived from the covariance computation.

Table 4.8: Covariance matrix for Kaufmann ratio PCA

Layer	1	2	3
1	0.03248	0.01169	0.01328
2	0.01169	0.05678	0.04432
3	0.01328	0.04432	0.03925

The Correlation matrix for Kaufmann's ratio is shown in Table 4.9 below in which the column signifies the layer of the PC for Kaufmann ratio while the row, the layer for the bands. This summarizes the values derived from the Correlation matrix computation.

Table 4.9: Correlation matrix for Kaufmann ratio PCA

Layer	1	2	3
1	1.00000	0.27228	0.37199
2	0.27228	1.00000	0.93880
3	0.37199	0.93880	1.00000

The first column from the table below illustrates the PC layer, the second column shows the Eigenvalue, the third column displays the percent of Eigen value and the last represents the accumulative of Eigen value all for Kaufmann's ratio. This table summarizes the percent and the accumulative eigenvalues for Kaufmann ratio as presented in Table 4.10 below;

Table 4.10: Percent and accumulative eigenvalues Kaufmann ratio

Pc layer	Eigenvalue	Percent of eigenvalues	Accumulative of eigenvalues
1	0.09786	76.1538	76.1538
2	0.02811	21.8742	98.0280
3	0.00253	1.9720	100.0000

4.1.3.2 *Sub-lineament maps result*

Various lineament analysis was done and are presented in Figure 4.11 to 4.14, the Extracted lineament of the study area, Overlaid lineament on the drainage and SRTM, Lineament and the drainage overlaid and the summary respectively. The blue color shows the drainage while the red, the lineament. This summarizes the different estimate from sub-lineament.

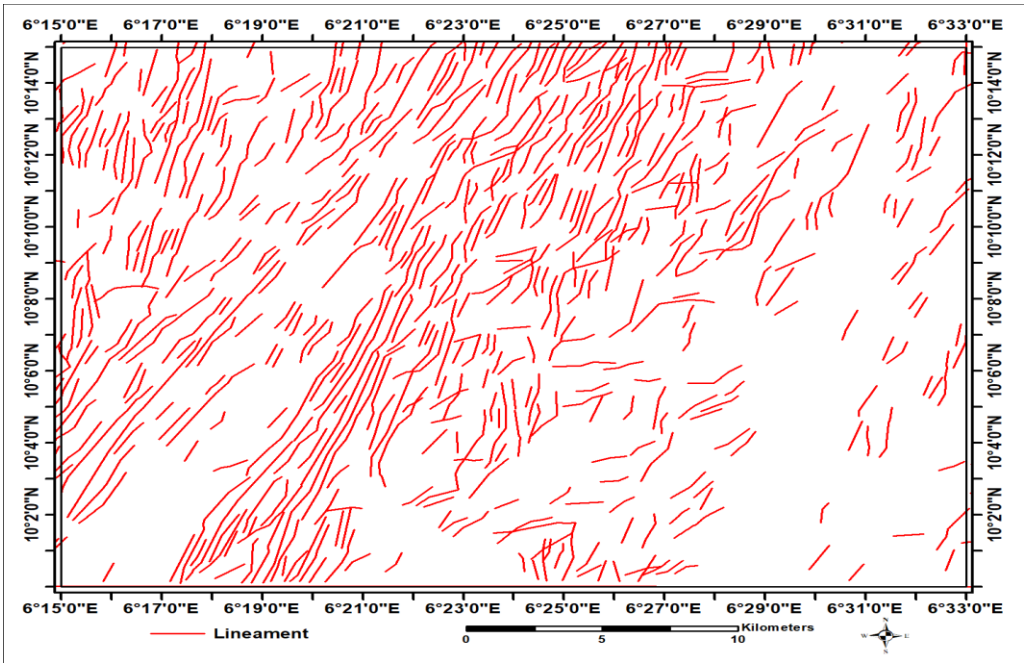

Figure 4.10: Extracted lineament of the study area

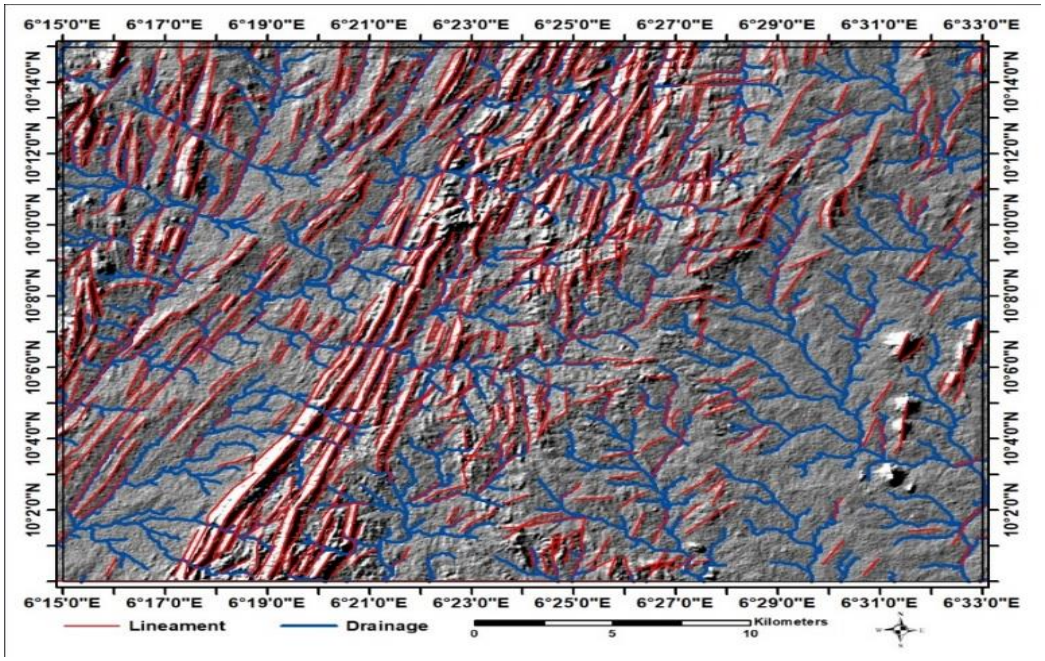

Figure 4.11: Overlaid lineament on the drainage and SRTM

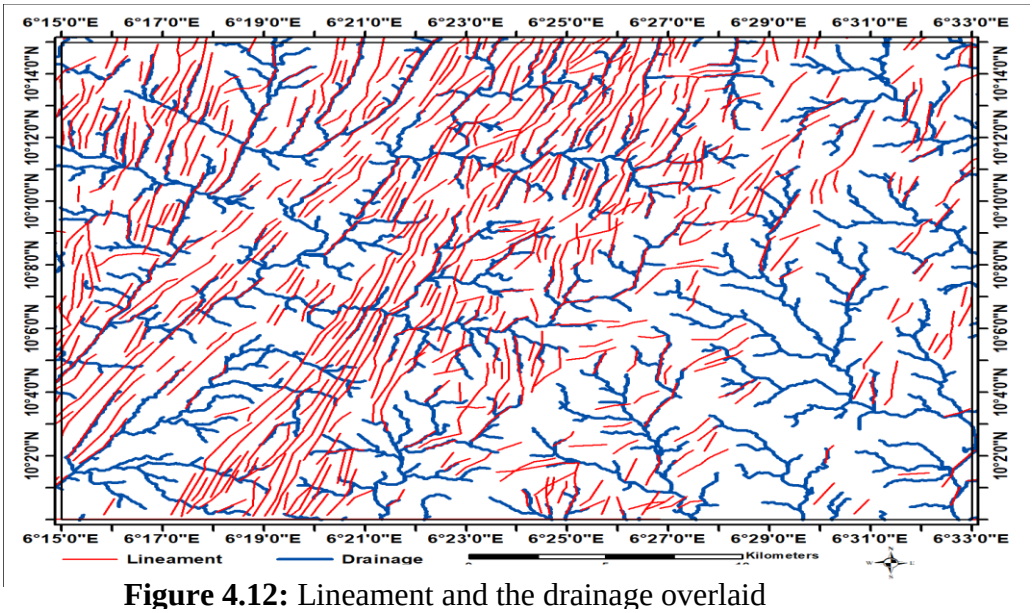

Figure 4.12: Lineament and the drainage overlaid

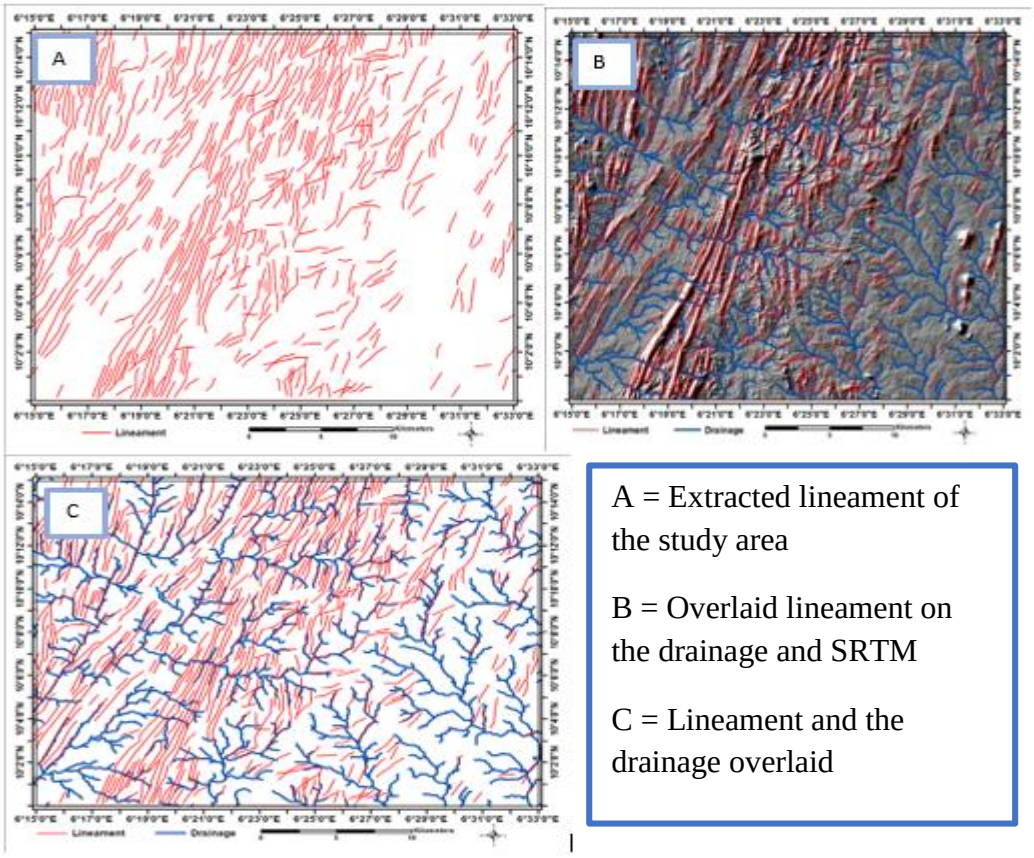

Figure 4.13: Summary of Figure 4.9 to 4.12

4.1.4 Multi criteria analysis for conditions

The multicriteria analysis was done and the result presented in Figure 4.14a-d which shows region of iron oxide, oxidation, hydrothermal alteration and silification respectively. Figure 4.15 a-d, displays the extracted lineament of the study area, gold mineralization on equal weight, overlaid lineament and drainage pattern and weighted gold mineralization zones correspondingly. Figure 4.14 and 4.15 (a-d) summarizes all the result gotten from the multicriteria analysis.

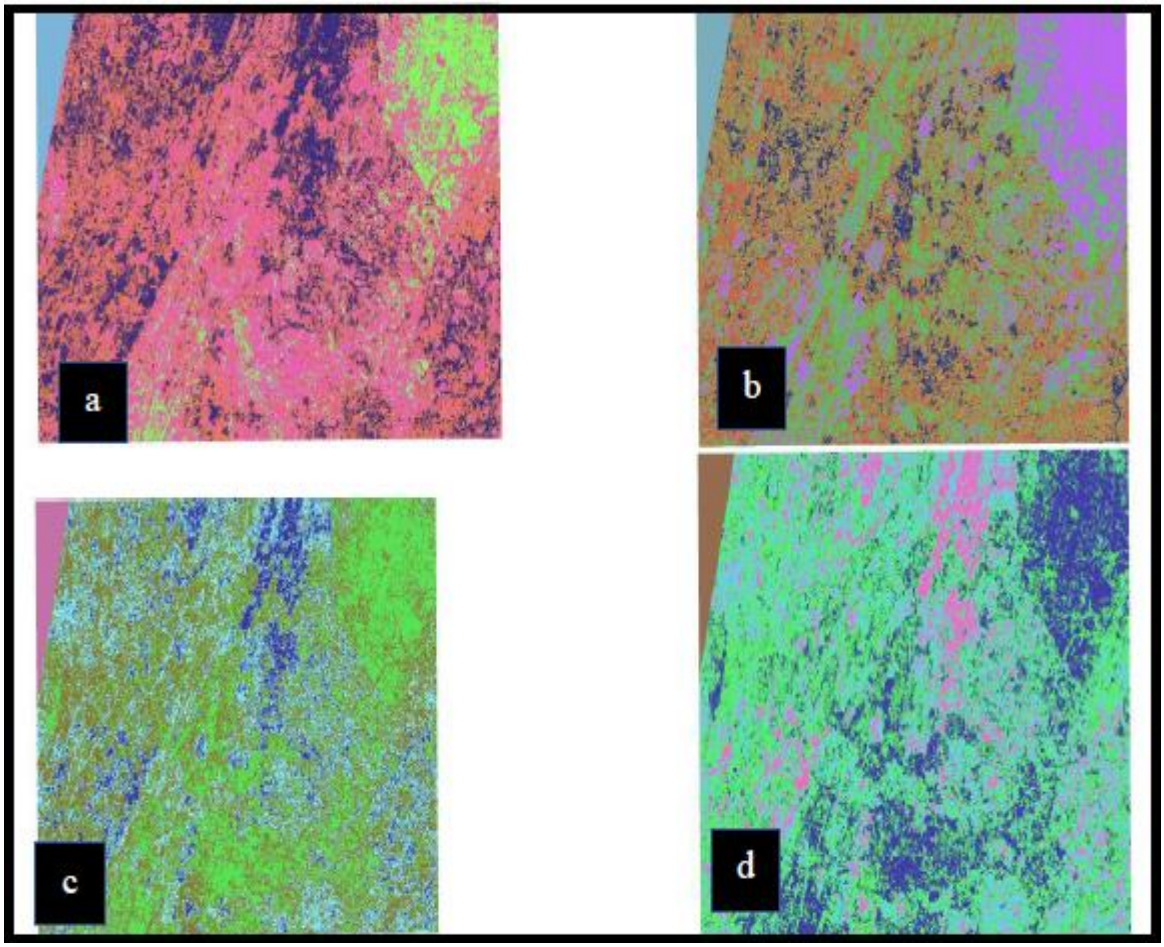

Figure 4.14: Simple raster combination (raster overlay) of Figure 4.1 to 4.7 showing (a) Iron-oxide in light green (b) oxidation in purple (c) Hydrothermal alteration in mint green (d) silification in deep blue

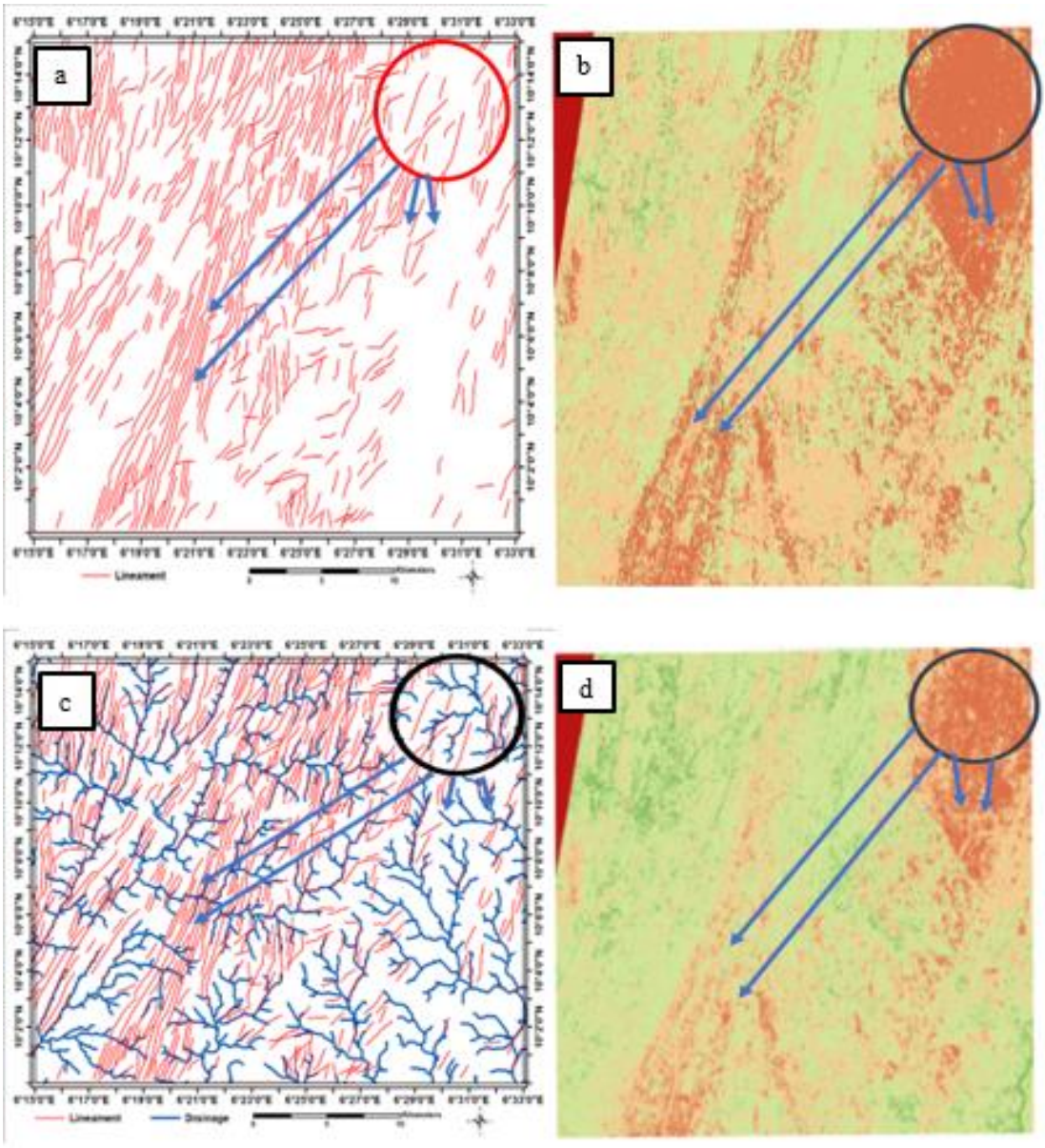

Figure 4.15: (a-d) Extracted lineament of the study area, Gold mineralization (equal weight) Au zones in dark peach, lineament and drainage overlaid and Gold mineralizatior (Oxidation 40, silification 30, Iron oxide 30) respectively.

4.2 Discussion of Results

4.2.1 Hydrothermal alterations

Images enhancing hydrothermal altered rocks using band ratios with distinctive reflection features were produced and presented in Figure 4.1.

In Figure 4.1 (a) Landsat 8 band ratio 4/2 image reveals areas where iron minerals (hematite, goethite, limonite, etc.) are abundant shown in bright tones; (b) Landsat 8 band ratio 6/5 image discriminates ferrous minerals with bright tone. (c) Landsat 8 band ratio (7/5) image reveals clay minerals, as illite, kaolinite and montmorillonite, in bright tones. (d) Landsat 8 band ratio 6/7 image shows alunite and hydrothermal clay minerals in bright tones.

In Figure 4.1(a) bands of Landsat-8, bands 2 and 4 responsive to iron oxides/hydroxides and bands 6 and 7 sensitive to hydroxyl-bearing minerals and carbonates, were also extensively used for hydrothermal alteration mineral mapping in metallogenic provinces (Pour and Hashim, 2015; pour *et al.,* 2019c) in Figure 4.1(d) iron oxide/hydroxide minerals contain diagnostic spectral characteristics coincident with selected bands of different sensors (Sabins 1999; Pour and Hashim, 2015). Hydroxyl-bearing (Al-OH and Fe,Mg-OH) and carbonates minerals were typically identified in the study region through Landsat-7 ETM+ band ratio of band 5/band 7, Landsat-8 band ratio of band 6/band 7 and ASTER band ratio of band 4/band 9, respectively (Pour and Hasim, 2015; Abubakar *et al*, 2019; Pour *et al*, 2019c).
An image incorporating these band ratios will discriminate altered from unaltered outcrop and highlight areas where concentration of these minerals occurs.

Hydrothermal alteration is linked to the underground circulation, which can attract the surface of hot water, loaded with dissolved minerals (Au, Copper, Barite, etc.). This circulation of hydrothermal fluids often occurs in the veins in volcanic zone, near a magma

chamber, or in plutonic zone. It dissolves the minerals present in the rocks crossed El Atillah *et al* 2019. Hydroxyl-bearing minerals present diagnostic spectral absorption features in the shortwave infrared radiation region, and thus this wavelength region is the best to explore and map hydrothermal alteration zones (Pour and Hashim, 2014).

4.2.2 Band combination response for hydrothermally altered rocks

4.2.2.1 *Single band combination*

Landsat 8 OLI was used to display the Natural colour of the study site in Maigiru, Madaka district Rafi local government Niger state Nigeria (Figure 4.2).

Single band combinations were applied in a first approach, in order to analyze the study area and visually interpret the multispectral imagery. Using Landsat 8 OLI imagery, six bands (B2, B3, B4, B5, B6 and B7) some of them enhancing relevant features for mineral exploration. A true colour image was produced with Landsat 8 visible bands 4, 3 and 2 (Figure 4.3). Green colour represent vegetation mostly along, brown and brown represent soil or rock and blue water. With this band combination, it is possible to do an exploratory analysis of the area, identifying rock exposure areas (brown), vegetated areas (green), rivers and lakes (blue) and urbanized areas. In addition, some structural features such as faults and fractures can be identified. Landsat 8 visible bands 4, 3 and 2 which is in contrast with Ombiro *et al* (2021) that combined bands 4,2,3 as True Image Colour

4.2.2.2 *False colour combination*

When composite image is created using a combination of 3 bands (such as infrared bands, shortwave infrared bands and visible bands) in RGB, an image that is produced tends to enhance certain features (Mwaniki *et al* 2015). This, however, depends on the bands selected for compositing. These bands are often assigned using the rocks' or altered minerals' spectral

characteristics. The band combination for identification of altered minerals, according to (Pour and Hashim, 2015; Rmdc, 2015), are: RGB (5,6,7), RGB (7, 5, 2) and RGB (5,4,3). It is for this reason that these band combinations were used to discriminate hydrothermally altered zones within the study area. The results for band combination are shown in Figure 4.3.

False Colour image was created for A, using bands 5, 4 and 3 (R, G, B). This band combination allows a better differentiation between vegetated areas (red areas) and good exposure outcrops (greyish colours). Light blue colour represent urbanized areas.

For a preliminary geological study, a contrast-enhanced RGB combination (SWIR, NIR, and Visible) was created. The most contrasting band combination for lithological features and that provide more detail without additional enhancement should include one visible (2, 3 and 4), one NIR (5) and one SWIR (6 or 7) band (USGS, 2015a). Based on this assumption, a composite using the bands 7, 5, 2 (RGB) was created (Figure 4.4) where it is possible identify outcrops as shades of orange and red, vegetation in light green and water in black.

4.2.2.3 *Sabins ratio*

An image using Sabin's ratio (4/2, 6/7 and 6/5 as RGB) was produced for lithological mapping and hydrothermal alteration zones (Figure 4.5). The ratio 4/2 was used for mapping iron oxides as hematite, limonite and jarosite, and has high reflectance in red region. The ratio 6/7 it's used to map clay minerals as kaolinite, illite and montmorillonite. The ratio 6/5 shows high reflectance in presence of ferrous minerals. In this Figure 4.5, light yellow colour represent outcrops and blue areas represent vegetation, Light green areas highlight hydrothermal alteration in outcrop rocks which is similar to Mateus and Frutuoso, 2015. This occupies like 20% of the study area which by interpretation means the area is hydrothermally

altered. According to Sabins, 1999; Ali and Pour, 2014, Sabins' band ratio is beneficial for lithological mapping and detection of hydrothermal alteration zones. Sabins ratios were displayed as in Figure 4.5 above, strong yellow may represent buildings and other human constructions and light green altered rocks. Colour variations can be seen in different band ratio results which are the primary keys to identify a hydrothermally altered zone.

4.2.2.4 *Kaufmanns ratio*

In Kaufmann ratio (7/5, 5/4, 6/7) Figure 4.6, this band ratio combination highlight meta-sediments as dark green and granite outcrops are represented as rose, vegetation as light blue and water as red. Some red areas can be related to the hydrothermal alteration. Kaufmann band ratio (7/5, 5/4 and 6/7) was also used for separation of vegetation from altered zones (Ali and Pour, 2014). Also, like 15% of the region from Figure 4.6 show that the area is hydrothermally altered. Figure 4.7 displays Figure 4.2 to figure 4.6 in a view.

4.2.3 PCA results analysis

The PCA is part of the group of multidimensional descriptive methods called factorial methods. The PCA proposes, from a rectangular table of data containing the values of *p* quantitative variables for *n* units, geometric representations of these units. These variables make it possible to determine the main components (principal component (PC)) that represent the contribution of the original tapes involving the spectral response of relevant substances and the spectral information of minerals of particular interest as in Figure 4.8 and 4.9 (A - D). It is used to create new uncorrelated components by identifying the axes in the original data that account for the largest amount of variation. This method has always shown the effectiveness of the results related to geological discrimination and mineral exploration. Minerals and substances are represented as dark or bright pixels in PC images, respectively,

according to the sign of the charge of the proper vector (Corumluoglu *et al*., 2015; Vural *et al*., 2017). The satisfactory results obtained by this technique guided El Atillah *et al* 2019 to use this technique at different stages.

Singh and Harrison (1985) states that new principal component images may be more interpretable than the original data as the multispectral dataset's dimensionality is reduced. When considering the Figure 4.8 A&B no much difference could be observed when compared with the PCA images of Figure C&D which by interpretation might mean that FCC have little or no effect in the generation of PC. Furthermore, the newly generated PCA images have more spectral difference, and the existing objects can be extracted effectively. PCA is more applicable for lithological mapping, and each lithological unit is revealed clearly in PC images; based on the selected minerals, the PC is selected, or sometimes, the composition of several PCs is created (Singh and Harrison, 1985). The boundary between two adjacent lithologies may be considered a lineament or sometimes a fault. Therefore, the analyst can easily digitize the edges from PC images.

PCA table analysis

The correlation matrix for the PCA of landsat bands used has all diagonals to be 1.0000 in Table 4.1 with 0.977275 as the lowest. The principal components for the bands and the eigen vectors of bands 2 to bands 7 in table 4.2 shows all positive in PCA 1, negative in PCA 2 band.

Spatially coherent information is clearly observed in the first five components (PC1, PC2, PC3, PC4, and PC5). The last PC band (PC6) contains less variance and so often appears noisy. The first three principal components (PC1, PC2, and PC3) contain about 99.6% of the total variance in the data. PC1 explains 98.61% (Table 4.2) of the total variance (spectral information) and has positive loadings for all bands. The second highest proportion of

variance (0.82%) (Table 4.4) is associated with PC2, which has negative loadings on bands 6 (-0.392) and 7 (-0.566) (Table 4.3&4.4). PC3 explains 0.44% (Table 4.5) of the total variance and has negative loadings from bands 5 (-0.539) and 6 (-0.343) (Table 4.3&4.4). The PC 4 has negative loadings on bands 4 (-0.734) band 5 (-0.018) and band 6 (-0.130) and positive loadings on the other bands (Table 4.3&4.4).

From Table 4.4, It is shown that the first principal component (PC1) consists of the positive elements of all spectral channels of the Landsat 8 image (bands 2, 3, 4, 5, 6, and 7). PC1 amounts to about 98.60 % of the eigenvalue of the total variance for the PCA data.

In Table 4.7 shows that the first principal component (PC1) consists of the positive elements of all spectral band of the sabins ratio of the Landsat 8 image (4/2, 6/7 and 6/5). PC1 amounts to about 83.86 % of the eigenvalue of the total variance for the PCA data.

In Table 4.10 shows that the first principal component (PC1) consists of the positive elements of all spectral band of the Kaufmann's ratio of the Landsat 8 image (7/5, 5/4 and 6/7). PC1 amounts to about 76.15 % of the eigenvalue of the total variance for the PCA data.

4.2.4 Sub-lineament extraction

In general gold mineralization occurs within linear tectonic zones in which relatively high strain magnitudes and available kinematic indicators attest to shearing in transcurrent or thrust systems (Phani, 2014). Permeability induced by structural deformation provided the main access for the hydrothermal fluids which were derived from a source external to the immediate environment of deposition (Phani, 2014). In Figure 4.10, the study area lineament map generated from PCI geomatical with majority in the NE direction.

Amaro and Strieder (1994) have emphasized that any lineament in imagery have topographic relief and/or associated tonal features which are due to the underground 3D structure in the Earth's crust. In such cases, most of those linear features may be considered as topographic

highs or lows when seen in the lightening direction of the image. The patterns and nature of the lineaments are different according to the association of positive, negative or tonal lineaments. The boundary between two adjacent lithologies may be considered a lineament or sometimes a fault. Therefore, the analyst can easily digitize the edges from PC images (Singh and Harrison,1985).

4.2.4.1 *Lineament, drainage and SRTM overlaid*

In Javhar *et al.,* 2019 it was noted that rivers sometime follow the geological structural elements but mostly are the result of erosion processes, which are not necessarily related to deformation. Therefore, it is important to evaluate the contribution of drainage-controlled extracted lineaments in the rose diagram directions of the lineaments. To this end, the drainage network of the study area was extracted from an SRTM digital elevation model (Figure 4.11). Comparing these directions with the lineament directions extracted from the radar data, we see that the contribution of the drainage network on the directions of the extracted lineaments is small because the lineaments' directions have one dominant direction—NW-SE—and are not homogenously distributed in all directions.

Geologic lineaments are important for mineral exploration as they are the potential locations for hosting ore bodies that are deposited by ascending hydrothermal fluids (Kotnise and Chennabasapa, 2015).

4.2.4.2 *Lineament and the drainage overlaid*

The drainage system which develops in an area is strictly dependent on the slope, the nature, and attitude of bedrock and on the regional and local fracture pattern (Travaglia and Dainelli, 2003). Most stream networks are adapted to regional slope and geological structures, picking out the main fractures in the underlying rocks as it has appeared in Figure 4.12. The contact between two lithologies can also appear as a linear feature. This contact may appear as a

change in drainage pattern across the structural features (Brockmann *et al.,* 1997) or the two units may have different spectral properties (Nguye and Ho, 1998).

From the above Figure 4.10, majority of the drainages run NW which do not really correlate with the direction of the lineament which has its majority direction in the NWSW. From this it can be deduced that the lineaments are not majorly caused by drainages but might be by some other underlying factors as stated by Javhar *et al.*, 2019 that rivers sometime follow the geological structural elements but mostly are the result of erosion processes, which are not necessarily related to deformation. Figure 4.13 displays the summary in Figure 4.9 – 4.12 in a view.

4.3 Multi Criteria Analysis for Gold Pattern

Iron oxide region was determined and displayed as light green (Figure 4.14a) and hydrothermal region as well (Figure 4.14c) which corresponds with the work of Aisabokhae and Oresajo, 2018; Putra *et al*., 2017 that say Landsat OLI can be used to calculate the correlation between iron oxide content in the soil and the possibility of hydrothermal alteration. The Landsat 8 OLI TIRS can determine the distribution of iron oxide and hydroxide minerals that dominate the alluvium and ophiolite rocky areas (Darmawan *et al*., 2020). In Figure 4.15(b & d), the regions of Oxidation and Silification were displayed respectively. Oxidation in purple and Silification in deep blue.

From Figure 4.15a which is the lineament map and likewise Figure 4.16c when compared with Figure 4.15(b & d) in the equal weight of oxidation silification and iron oxide and 40:30:30 ratio, it could be deduced that only very few lineament exist in the region of the deep blue circle of Figure 4.15b. though there were existence of lineament in the region where the blue arrows in Figure 4.15(a to d) pointed, which by interpretation could mean that

oxidation, silification and the presence of iron oxides were not in large quantity there and these are strong indicators for the detection of gold minerals. Geological lineaments are the earth's linear features indicating significant tectonic units in the crust associated with the formation of minerals, active faults, groundwater controls, earthquakes, and geomorphology (Ahmadi and Pekkan 2021).

CHAPTER FIVE

5.0 CONCLUSION AND RECOMMENDATIONS

5.1 Conclusion

Bands 6/7 and 7/6 of Landsat 8 OLI with short wave infrared radiation employed in this study identified the hydrothermally altered region of the study area.

Ratio 4/2 highlighted area with abundant iron oxides, ratio 6/5 identified the ferrous minerals, clay minerals were identified from 7/5 ratio, ratio 6/7 identified hydrothermally altered clay. Sabin's ratio (4/2,6/7,6/5) identified altered rocks in light green and Kaufmann's ratio (7/5,5/4,6/7) identified hydrothermally altered regions in red in the study area.

From the lineament map of the study area generated, the sub surface lineament had little effect on the possible gold mineralization within the study area because only a few of the lineament were discovered in the region identified. It was deduced that majority of the area where a great number of lineaments exists have little or no gold mineral present in them though there might be another mineral.

From the simulation studies, under the simulated environmental conditions in the identification of the region of Oxidation, Silification, Iron oxides and hydrothermal alterations with equal and unequal weight assignment, the possible pattern of Gold presence was discovered in the upper NE of the region.

It was affirmed that by computed ratios, remote sensing studies could be used for demarcation of hydrothermal alteration zones which further buttress the point that Landsat 8 image processing methods such as band combination, band ratio, and principal component analysis proved accurate for identifying iron oxides.

From the results obtained and the interpretation of the multi-criteria analysis, it can be deduced that gold mineralization prospectivity mapping using LandSAT 8 OLI is an accurate

means of gold potential zoning. The study further confirms that the use of weighted overlay wherein the results from PCA serve as a-priori weights for conditioning factor significantly improves the result obtained; thus, making the extracted information a better depiction of reality than using equal weights. Consequently, we conclude that Landsat 8 image processing methods such as band combination, band ratio (Sabins and Kaufmann), hydrothermal alterations and principal component analysis are accurate for identifying iron oxides which is an alteration mineral to the presence of Gold mineral.

5.2 Recommendation

Based on the processes of band rationing, identifying hydrothermally altered regions, extraction of subsurface lineament and simulations of some environmental condition such as Oxidation, Silification involved in this research, it hereby recommended that:

1. Bands 6/7, 7/6, 4/2, 7/5, be used in any identification of hydrothermally altered region as well as the Sabins and Kaufmanns ratio.
2. Lineament map of any site prospecting for gold mineral must be firstly generated in other to avoid lineament due to other factors.
3. In other to further clarify the probable location of gold, the simulated environmental condition in identification of region of oxidation, silification, iron oxides and hydrothermal alteration should be considered.
4. there should be a considerations on weighting based on the significance factor of the largest band contributor in both indices (Sabin's and Kaufmann's ratio) as results obtained showed that the variable weight overlay (guided by PCA eigenvalues) was more consistent with the reality of the area than the equal weight overlay, when both were compared with the reality of ongoing mining activities within the vicinity In further studies for quantification of gold within the study area could be carried out.

5.3 Contribution to Research Knowledge

This study revealed and addressed gaps in prospecting for gold using Landsat 8 imageries in Rafi local Government and in doing so, contribute significantly to knowledge. Based on the identified gaps, the research contributions identified are:

I. Possibility of mapping gold mineralization zones using certain mapable characteristics associated with it based on their spectral features.

II. Characteristics such as rock-outcrops, oxidation, silification, iron oxide and invariably hydrothermal alteration as good pointers to gold exploration

III. The percentage contribution of each contributory characteristic can determine the spatial distribution of the mineral

IV. The variable weight overlay (guided by PCA eigenvalues) was more consistent with the reality of the area than the equal weight overlay, when both were compared with the reality of ongoing mining activities within the vicinity.

V. Using Multicriteria Analysis to investigate gold mineralization, oxidation, silification, iron oxide and hydrothermal alteration, the availability of gold can be ascertained.

REFERENCES

Abdelsalam, M. & Stern, R. (2000). Mapping gossans in arid regions with Landsat TM and SIR-C images, the Beddaho Alteration Zone in northern Eritrea, J. Afr. *Earth Sci*. 30 (4) 903–916.

Abdullah, A., Akhir, J. M., & Abdullah, I. (2010a). Automatic Mapping of Lineaments Using Shaded Relief Images Derived from Digital Elevation Model (DEMs) in the Maran-Sungai Lembing Area, Malaysia. *Electronic Journal of Geotechnical Engineering* 15(J): 949-957.

Abdullah, A., Akhir, J. M., & Abdullah, I. (2010b). The Extraction of Lineaments Using Slope Image Derived from Digital Elevation Model: Case Study: Sungai Lembing-Maran area, Malaysia. *Journal of Applied Sciences Research* 6 (11): 1745-1751.

Abubakar, A. J. A., Hashim, M., & Pour, A. B. (2019). Remote sensing satellite imagery for prospecting geothermal systems in an aseismic geologic setting: Yankari Park, Nigeria. *Int. J. Appl. Earth Obs. Geoinf.*, 80, 157–172.

Adiri, Z., El Harti, A., Jellouli, A., Maacha, L., & Bachaoui, E. (2016). Lithological mapping using Landsat 8 OLI and Terra ASTER multispectral data in the Bas Draˆa inlier, Moroccan Anti Atlas. *J. Appl. Remote Sens.* 10(1), 016005 14.

Agar, B. & Coulter, D. (2007). Remote sensing for mineral exploration – A decade perspective 1997-2007, *in* B Milkereit (ed.), *Proceedings of Exploration 07: Fifth Decennial International Conference of Mineral Exploration;* 109-136.

Ahmad, L., Shah, M. T., & Khan, S. (2015). Reflectance spectroscopy and remote sensing data for finding sulfide-bearing alteration zones and mapping geology in Gilgit-Baltistan, Pakistan. *Earth Science Informatics*, 2015: p. 1-9.

Ahmadi, H. & Pekkan, E. (2021). Fault-Based Geological Lineaments Extraction Using Remote Sensing and GIS—A Review. *Geosciences*, *11*, 183. https://doi.org/ 10.3390/geosciences11050183.

Aisabokhae, J. E. & Oresajo, S. B. (2018). Supervised classification of Landsat-8 band ratio images for geological interpretation of Sokoto, Nigeria. South African *Journal of Geomatics*, 7(3), 360-371.

Ajakaiye, D. E., Hall, D. H., Ashiekaa, J. A., & Udensi, E.E. (1991). Magnetic anomalies in the Nigerian continental mass based on aeromagnetic surveys. *Tectonophysics* 192(1):211-230.

Alfouzan, F., Alotaibi, A., Cox, L., & Zhdanov, M. (2020). Spectral Induced Polarization Survey with Distributed Array System for Mineral Exploration: Case Study in Saudi Arabia. *Minerals* 10, 769.

Ali, A. & Pour, A. (2014). Lithological mapping and hydrothermal alteration using Landsat 8 data: a case study in ariab mining district, red sea hills, Sudan. *International Journal of Basic and Applied Sciences, 3*(3), 199–208.

Amadi, A. N. (2012). Geostatistical assessment of ground water quality from coastal aquifers of eastern n/iger Delta, Nigeria. *Geosciences,* 2, 51-59.

Amaro, V. E. & Strieder, A. J. (1994). Analisede fotolineamentos e padroese structural semimagens de satellite. In*: CongressoBrasileiro de Geologia 38, BoletimResumosExpandidos* 1 443-444.

Amer, R., Kusky, T., & El Mezayen, A. (2012). Remote sensing detection of gold related alteration zones in Um Rus area, Central Eastern Desert of Egypt. *Adv. Space Res.* 49, 121–134.

Aminzadeh, B & Samani, F. (2006). Identifying the boundaries of the historical site of Persepolis using remote sensing. *Remote Sens. Environ*. 102 (2006) 52–62.

Anderson, L. A. (1984). Self-potential investigations in the Puhimau thermal area, Kilauea Volcano, Hawaii *SEG Expanded Abstr.* 3 84 DOI:10.1190/1.1894270

Andi A. N., Gumilar U. N., & Pulung A. P. (2017). Interpretation of Groundwater Potential Zones Based on Lineament Pattern Data Analysis in Ambon Island, Moluccas Province, Indonesia, *International Journal of Applied Engineering Research,* Volume 12, Number 17 Pp. 6941-6945.

Anonyme, (2002). Réflexion citoyenne sur l'avenir de la vallée du Bouregreg. 189.

Aransiola, A. B. & Odumosu, J. O. (2021). Prospectivity Mapping for Gold (Au) Mineralization Using LandSAT 8 OLI Data in Part of Niger State, Nigeria. SETIC 2020 International Conference: "Sustainable Housing and Land Management" School of Environmental Technology, Federal University of Technology, Minna.

Argialas, D. P. & Mavrantza, O. D. (2004). Comparison of edge detection and Hough transform techniques for the extraction of geologic features. *Proceedings of the ISPRS Congress* 35(3B), 790–795.

Arisanty, D., Saputra, A. N., Rahman, A. M., Hastuti, K. P., & Rosadi, D. (2021). The Estimation of Iron Oxide Content in Soil based on Landsat 8 OLI TIRS Imagery in Wetland Areas. Pertanika *J. Sci. & Technol*. 29 (4): 2829 – 2843.

Arlegui, L. E. & Soriano, M. A (1998). Characterizing lineaments from satellite images and field studies in the central Ebro basin (NE Spain), *International Journal of Remote Sensing*, 19:16, 3169-3185, DOI: 10.1080/01431698214244

Asl, R. A., Afzal, P., Adib, A., & Yasrebi, A. B. (2015). Application of multifractal modeling for the identification of alteration zones and major faults based on ETM+ multispectral data. *Arabian J. Geosci*. 8, 2997–3006.

Austin, J. R. & Blenkinsop, T. G. (2008). The Cloncurry Lineament: geophysical and geological evidence for a deep crustal structure in the Eastern Succession of the Mount Isa Inlier. *Precambrian Res*. 163 (1–2), 50–68.

Baastad, I., Løke, T., & Kaspersen, P. (2005). ASI - A new airborne hyperspectral imager. Proceed-ings of the 4th EARSeL Workshop on Imaging Spectroscopy - *New Quality in Environmental Studies* (Warsaw, Poland) pp. 107-110

Babiker, I. S., Zeinelabdein, K. A. E., & El-Nadi, A. H. (2015), Geological mapping and gold prospecting of Wadi Umm Beckol-Wadi Akasha Area, Northern Sudan based on remote sensing, *Am. J. Earth Sci.* 2 (6) 172 – 179.

Barrett, T. J. & MacLean, W. H. (1994). Chemostratigraphy and hydrothermal alteration in exploration for VHMS deposits in greenstones and younger volcanic rocks. In Alteration and Alteration Processes Associated with Ore-Forming Systems; Lentz, D.R., Ed.; *Geological Association of Canada:* St. John's, NL, Canada, Volume 11, pp. 433–465.

Berberian, M. (1995). Master "blind" thrust faults hidden under the Zagros folds: Active basement tectonics and surface morphotectonics. *Tectonophysics* 241, 193–224.

Blaschke, T. (2010). Object based image analysis for remote sensing. *ISPRS Journal of Photogrammetry and Remote Sensing,* 62: 2-16.

Bolouki, S. M., Ramazi, H. R., Abbas Maghsoudi, A., Pour, A. B., & Sohrabi, G. (2020). A Remote Sensing-Based Application of Bayesian Networks for Epithermal Gold Potential Mapping in Ahar-Arasbaran Area, NW Iran. *Remote Sens*. 12, 105.

Brockmann, C. E., Fernandez, A., Ballon, R., & Claure, I. I. (1977). 'Analysis of Geological structures based on landsat-1 images,' in *Remote Sensing Applications for Mineral Exploration*, W. I., Smith. Ed, pp. 292-317, Dowden, Hutchison and Ross, Strongsberg, Pa, USA.

Burberry, C. M & McMechan, M. E. (2012). Deep transverse basement structural control of mineral systems in the southeastern Canadian Cordillera. *Can. J. Earth Sci*. 2012, 49, 693–708.

Burberry, C. M., Swiatlowski J. L., Searls M. L., & Filina, I. (2018). Joint and Lineament Patterns across the Midcontinent Indicate Repeated Reactivation of Basement-Involved Faults, *Geoscience*, 8, 215.

Casas, A. M., Cortes, Angel L., Maestro, A., Soriano, M.A., Riaguas, A., & Bernal, J. (2000). "A program for lineament length and density analysis", *Computers and Geosciences*, Vol. 26, No. 9/10, 1011-1022.

Chakraborty, R., Kereszturi, G., Durance, P., Pullanagari, R., Ashraf, S., & Anderson, C. (2020). Biogeochemical exploration of gold mineralization and its pathfinder elements using hyperspectral remote sensing. Conference Paper, December. doi: 10.1109/igarss39084.2020.9323737

Chernicoff, C. J. & Nash, C. R. (2002). Geological interpretation of Landsat TM imagery and aeromagnetic survey data, northern Precordillera region, Argentina. *Journal of South American Earth Sciences,* 14: 813-820.

Christian, M., Kristine, B.N., Christian, R., Hermann, K., Christoph, G., & Maarten, D.W. (2014). Spaceborne mine waste mineralogy monitoring in south Africa, applications for modern push-broom missions: Hyperion/OLI and EnMap/Sentinel-2. *Remote Sens*. 6, 6790–6816.

Chuvieco, E. (2010). Teledetecci_on Ambiental. La observaci_on de la Tierra desde el espacio. Barcelona. Editorial Ariel S.A.

Cinque, A., Patacca, E., Scandone, P., & Tozzi, M. (1993). Quaternary kinematic evolution of the Southern Appennines. Relationships between surface geological features and deep lithospheric structures. *Ann. Geophys*, 36, 249–260.

Clark, R. N., Swayze, G. A., Gallagher, A. J., King, T. V. V., & Calvin, W. M. (1993). The U. S. Geological Survey, Digital Spectral Library. Version 1: 0.2 to 3.0 microns. U.S. *Geological Survey Open File Report* 93-592, 1340 pages.

Cloutis, E. A. (1996). Hyperspectral geological remote sensing: evaluation of analytical techniques, *Int. J. Remote Sens.* 17 (12), 2215–2242.

Cocks, T., Jenssen, R., Stewart, A., Wilson, I., & Shields, T. (1998). The HyMapTM airborne hyper-spectral sensor: the system, calibration and performance. *1st EARSEL Workshop on Imaging Spectroscopy (*Zurich, Switzerland) pp. 37-42

Colvine, A. C. (1988). Archean Lode Gold Deposits in Ontario; OGS Miscellaneous Paper 139; Ontario Ministry of Northern Development and Mines: Greater Sudbury, ON, Canada; Volume 139, ISBN 077294105X. Comparison of LANDSAT ETM and ASTER Imagery. Case Study: Suoimuoi Tropical Karst Catchment, Vietnam. *Remote Sensing for Environmental Monitoring, GIS Applications, and Geology*. Vol. 59830T-1.

Cooke, D. R., Baker, M., Hollings, P., Sweet, G., Chang, Z., Danyushevsky, L., Gilbert, S., Zhou, T., White, N.C., & Gemmell, J.B. (2014). New advances in detecting the distal geochemical footprints of porphyry systems-epidote mineral chemistry as a tool for vectoring and fertility assessments. In Building Exploration Capability for the 21st Century; Kelley, K.D., Golden, H.C., *Eds.; Colt Print Services:* Boulder, CO, USA, pp. 127–152, ISBN 978-1-629491-424.

Corry, C. E. (1981). The role of the self-potential method in the exploration for molybdenite AMAX, Climax Molybdenum Co., Golden, CO, 53 pp 7.

Corumluoglu, O., Vural A., & Asri I. (2015) Determination of Kula Basalts (Geosite) in Turkey using Remote Sensing Techniques". *Journal of Arabian Geosciences*. 8:10105– 10117. (hyperlink "http://spiedl.aip.org/jhtml/doi.jsp" doi: 10.1007/s12517-015-1914-4).

Corwin, R. F & Hoover, D. B. (1979). The self-potential method in geothermal exploration *Geophysics* 44 226–45s

Corwin, R. F. (1984). The self-potential method and its engineering applications; an overview *54th Ann. Int. Meeting Soc. Explor. Geophys. Expanded Abstr. (Soc. Explor. Geophys., Tulsa)* Session: SP1

Cracknell, M. J. (2014). Reading, Geological mapping using remote sensing data: A comparison of five machine learning algorithms, their response to variations in the spatial distribution of training data and the use of explicit spatial information. *Computers & Geosciences.* 63: p. 22-33.

Crosta, A. P. & Rabelo, A., (1993). Assessing of Landsat TM for hydrothermal alteration mapping in central western Brazil. *Proceedings of Ninth Thematic conference geologic remote sensing Pasadinea,* p. 1053-61, California, USA.

Crósta, A.P., Souza Filho, C.R., Azevedo, F., & Brodie, C. (2003). Targeting key alteration 648 minerals in epithermal deposits in Patagonia, Argentina, Using ASTER imagery and principal component analysis. *Int. J. Remote Sens*. 24, 4233–4240.

Cross, A. M. (1988). Detection of circular geologic features using the Hough transform. *International journal of remote sensing*, 9, 1519-1528.

Cruz, C., Noronha, F., Santos, P., Mortensen, J.K., & Lima, A. (2018). Supergene gold enrichment in the Castromil-Serra da Quinta gold deposit, NW Portugal. *Mineral. Mag.* 82, S307–S320.

Darmawan, I. G. B., Yassar, M. F., Elvarani, A. Y., Vira, B. A., & Damayanti, L. (2020). Preliminary study of mining material prospects based on hydrothermal alteration distribution using composite and density slicing of Landsat 8 image in Ulubongka Regency, Central Sulawesi. *Promine,* 8(1), 1-7. https://doi. org/10.33019/promine. V 8i1.1799

De Boissieu, F., Sevin, B., Cudahy, T., Mangeas, M., Chevrel, S., Ong, C., Rodger, A., Maurizot, P., Laukamp, C., & Lau, I. (2018). Regolith-geology mapping with support vector machine: A case study over weathered Ni-bearing peridotites, New Caledonia. *Int. J. Appl. Earth Obs. Geoinf.* 2018, 64, 377–385.

Demattê, J. A. M., Horák-Terra, I., Beirigo, R. M., da Silva Terra, F., Marques, K. P. P., Fongaro, C. T., Silva, A. C., & Vidal-Torrado, P. (2017). Genesis and properties of wetland soils by VIS-NIR-SWIR as a technique for environmental monitoring. *Journal of Environmental Management*, 197, 50-62. https:// doi.org/10.1016/j.jenvman.2017.03.014

Demirkesen, A. C. (2009). Quantifying geological structures of the Nigde province in central Anatolia, Turkey using SRTM DEM data. *Environ. Geol*. 2009, 56, 865–875.

Dervic, K., Sinik, V., & Despotovic, Z. (2019). IX *International Conference Industrial Engineering and Environmental Protection* (IIZS 2019) October 3rd-4th, Zrenjanin, Serbia.

Drury, S. (2001). Image Interpretation in geology, 3rd Ed. Blackwell Science Inc, Malden. 290p.

Drury, S. A. (1987). Image Interpretation in Geology. Allen & Unwin publ., London, 243 p.

Drury, S. A. (1993): Image Interpretation in Geology. 2nd ed., -271 pp., (Chapman and Hall), London.

Drusch, M., Del Bello, U., Carlier, S., Colin, O., Fernandez, V., Gascon, F., Hoersch, B., Isola, C., La-berinti, P., Martimort, P., Meygret, A., Spoto, F., Sy, O., Marchese, F., & Bargellini, P. (2012). Sentinel-2: ESA's Optical High-Resolution Mission for GMES Operational Services. *Remote Sensing of Environment*, 120, 25-36

Dunn, S. C. & Von der Heyden, B. P. (2021). Gold remobilization in gossans of the Amani area, southwestern Tanzania. *Ore Geology Reviews* 131, 104033

Dunn, S. C., Von der Heyden, B. P., Bracciali, L., & St.Pierre, B. (2019). Geology and U-Pb geochronology of the Amani Region, southwestern Tanzania. *J. African Earth Sci*. 162, 35. https://doi.org/10.1016/j.jafrearsci. .103729.

Eastman, J. R. & Filk, M. (1993). Long sequence time series evaluation using standardized principal components. *Photogrammetric Engineering and Remote Sensing*. 59(6) 991{996.

Ejepu, J. S., Unuevho, C. I., Ako, T. A., & Abdullahi, S. (2018). Integrated geosciences prospecting for gold mineralization in Kwakuti, North-Central Nigeria. *Journal of Geology and Mining Research* Vol. 10(7), pp. 81-94. DOI: 10.5897/JGMR2018.0296.

El Atillah, A., El Morjani, Z. E., &, M. (2019). Use of the sentinel-2a multispectral image for litho-structural and alteration mapping in Al glo'a map sheet (1/50,000) (Bou azzer–el graara inlier, central anti-atlas, Morocco). *Artificial Satellites*, Vol. 54, No. 3 – 2019 DOI: 10.2478/arsa-2019-0007

Embley, R. W., Jonasson, I. R., Perfit, M. R., Franklin, J. M., Tivey, M. A., Malahoff, A., Smith, M. F., & Francis, T. J. G. (1988). Submersible investigation of an extinct hydrothermal system on the Galapagos Ridge; sulfide mounds, stockwork zone, and differentiated lavas. *Can. Mineral.* 26, 517–539.

Estornell, J., Jesus M. M., Sebastia, T. M., & Mengual, J. (2013). Principal component analysis applied to remote sensing. *Modelling in Science Education and Learning* Volumen 6(2), No. 7. Instituto Universitario de Matematica Pura y Aplicada

Fagbohun, B. J., Adeoti, B., & Aladejana, O. O. (2017). Litho-structural analysis of eastern part of Ilesha schist belt, Southwestern Nigeria. *J. Afr. Earth Sci.* 133, 123–137.

Francis, P. & Rothery, D. (1987). Using the Landsat Thematic Mapper to detect and monitor active volcanoes: An example from lascar volcano, northern Chile. *Geology* 15, 614–617.

Fripp, R. E. P. (1979). "Strata bound gold deposit in Archaean banded iron formation", Rhodesia *Econ. Geol.* V.71, P. 58-75, http://dx.doi.org/10.2113/gsecongeo.71.1.58

Fu, J., Jia, S., & Wang, E. (2020). Combined Magnetic, Transient Electromagnetic, and Magnetotelluric Methods to Detect a BIF-Type Concealed Iron Ore Body: A Case Study in Gongchangling Iron Ore Concentration Area, Southern Liaoning Province, China. *Minerals* 10, 1044.

Fundamentals of Remote Sensing (2012). *Canada Centre for Remote Sensing*. Accessed 23th October. http://www.nrcan.gc.ca/earth-sciences/geography boundary/remotesensing/fundamentals/1814

Gabr, S., Ghulam, A., & Kusky, T. M. (2010). Detecting areas of high-potential gold mineralisation using ASTER data. *Ore Geology Reviews,* 38: 59-69.

Gates, A. E. & Costa, R. E. (1998). Multiple Reactivation of Rigid Basement block margins, examples in the northern Reading Prong, USA. In Basement Tectonics 12; *Proceedings of the International Conferences on Basement Tectonics*; Hogan, J.P., Gilbert, M.C., Eds.; Springer: Dordrecht, The Netherlands, pp. 123–153.

Ge, W., Cheng, Q., Tang, Y., Jing, L., & Gao, C. (2018). Lithological Classification Using Sentinel-2A Data in the Shibanjing Ophiolite Complex in Inner Mongolia, China. *Remote Sens*. 10, 638

Ghazali, S., Aasif, S., Farooqi, A., Shah, V. A., Teli, M. N., & Dada, M. A. (2015). Gold prospecting using Remote Sensing 'A case study of Sudan'. *International Journal of Engineering Research and Development* e-ISSN: 2278-067X, p-ISSN: 2278-800X, www.ijerd.com Volume 11, Issue 09 (September 2015), PP.01-05

Gifkins, C. C., Herrmann, W., & Large, R. R. (2005). *Altered Volcanic Rocks: A Guide to Description and Interpretation*; Centre for Ore Deposit Research, University of Tasmania: Hobart, Australia.

Goetz, A. F. H., Rock, B. N., & Rowan, L. C. (1983). Remote sensing for exploration, Overview *Econ. Geol*. 78 (1983) 573–590.

Geological Research Authority of Sudan (GRAS) (1989). Base metal in the Sudan, GRAS Rep. Sudan.

Gupta, R.P. (1991). Remote Springer- verlag *Geology*. – 356 pp., Berlin-Heidelberg (Springer).

Haldar, S.K. (2018). Mineral Exploration Principles and Applications, 2nd ed. Elsevier.

Han, T. & Nelson, J. (2015). Mapping hydrothermally altered rocks with Landsat 8 imagery: A case study in the KSM and Snow field zones, northwestern British Columbia. In: Geological Fieldwork 2014, British Columbia Ministry of Energy and Mines, *British Columbia Geological Survey* Paper, pp.103-112.

Hashim, M. (2013). Automatic lineament extraction in a heavily vegetated region using Landsat Enhanced Thematic Mapper (ETM+) imagery. *Advances in Space Research*, 51: p. 874–890

Hewson, R. D., Cudahy, T. J., Mizuhiko, S., Ueda, K., & Mauger, A. J. (2005). Seamless geological map generation using ASTER in the Broken Hill-Curnamona province of Australia. *Remote Sensing of Environment*, 99: 159-172.

Herrington, R.J. & Stanley C.J. (2015). Gold deposits, the natural history museum, London, UK. *Geology* – iv,1-6.

Hung, Q. L., Batelaan, O., & De Smedt, F. (2005). Lineament extraction and analysis, comparison of LANDSAT ETM and ASTER imagery. Case study: Suoimuoi tropical karst catchment, Vietnam. in *SPIE Remote Sensing for Environmental Monitoring, GIS Applications, and Geology*. Proc. of SPIE Vol. 5983 59830T-1

Hunt, G. R. & Ashley, R. P. (1979). Spectra of altered rocks in the visible and near-infrared. *Econ. Geol.* 74, 1613–1629.

Hunt, G. R. (1977). Spectral signatures of particulate minerals in the visible and near-infrared. *Geophysics*, 42, 501–513.

Huntington, J. (1998). Space dependent technologies – *Remote sensing in mineral exploration*. Academy Symposium "Technology – Australia's Future: New Technology for Traditional Industries", November, 99: 159-172.

Ihbach, F., Kchikach, A., Jaal, M., Elazzab, D., Yazami, O. K., Jourani, E., Ruano, J. A. P., Olaiz, O. A., & Dávila, L. V. (2020). Geophysical Prospecting for Groundwater Resources in Phosphate Deposits (Morocco). *Minerals*, 2020, 10, 842

Irons, J. R, Dwyer, J. L., & Barsi, J. A. (2012). The next Landsat satellite: The Landsat Data Continuity Mission. *Remote Sensing of Environment*, 122, 11-21.

Jambor, J. L. & Blowes, D. W. (Eds.) (1994). Short course Handbook on Environmental Geochemistry of Sulfide Mine-wastes. *Mineralogical Association of Canada, Nepean*, 22: 438 pp.

Javhar, A., Chen X., Bao A., Jamshed A., Yunus, M., Jovid, A., & Latipa, T. (2019). Comparison of Multi-Resolution Optical Landsat-8, Sentinel-2 and Radar Sentinel-1 Data for Automatic Lineament Extraction: A Case Study of Alichur Area, SE Pamir Remote Sens. 11, 778

Jenson, J. R. (2000). An earth resource perspective. *Remote sensing of the environment* Prentice-Hall Publ., New Jersy, 544p.

Jensen, F.V. (1996). An Introduction to Bayesian Networks; *UCL Press: London, UK;* Volume 210, pp. 1–178.

Jeong, Y., Yu, J., Koh, S. M., Heo, C. H., & Lee, J. (2016). Spectral characteristics of minerals associated with skarn deposits: A case study of Weondong skarn deposit, South Korea. *Geosci. J.* 20, 167–182.

Jia, X. & Richards, J. A. (1999). Segmented Principal Components Transformation for Efficient Hyperspectral Remote-Sensing Image Display and Classification. *IEEE Transactions on Geoscience and Remote Sensing*. 37(1). pp. 538{542.

Kargi, H. (2007). Principal components analysis for borate mapping, *Int. J. Remote Sens.* 28 (8) 1805–1817.

Kariuki, P. C., Woldai, T., & Van der Meer, F. (2004). The role of remote sensing in mapping swelling soils. *Asian Journal of Geo-informatics*, 5: 43-53

Kaufmann, H, Segl, K., Chabrillat, S., Hofer, S., Stuffler, T., Mueller, A., Richter, R., Schreier, G., Haydn, R., & Bach, H. (2006). EnMAP a hyperspectral sensor for environmental mapping and analysis. In: *IEEE International Conference on Geoscience and Remote Sensing, (IGARSS)*, 1617-1619

Kiberu, J. (2002). Induced polarization and resistivity measurements on a suite of near surface soil samples and their empirical relationship to selected measured engineering parameters *MSC.* Thesis *International Institute for Geo-information Science and Earth Observation* (ITC), Enschede, The Netherlands p 119

Kishida, A. & Kerrich, R. (1987). Hydrothermal alteration zoning and gold concentration at the Kerr-Addison Archean lode gold deposit, Kirkland Lake, Ontario. *Econ. Geol*. 82, 649–690.

Kotnise, 1. G. H. & Chennabasappa, S. (2015). Application of Remote Sensing Techniques in Identification of Lithological Rock Units in Southern Extension of Kolar Schist Belt from Chigargunta, Chittoor District, Andhra Pradesh to Maharajagadai, Krishnagiri District, Tamil Nadu. *International Journal of Innovative Science, Engineering & Technology*, Vol. 2 Issue 11, November.

Krishnamurthy, Y. V. N., & Sreenivasan, G. (2005). Remote Sensing Technology for Exploration of Mineral Deposits with Special Reference to Bauxite and Related Minerals. ISCOBA Conference Paper.

Large, R. R., Gemmell, J. B., Paulick, H., & Huston, D. L. (2001). The alteration box plot: A simple approach to understanding the relationship between alteration mineralogy and lithogeochemistry associated with volcanic-hosted massive sulfide deposits. *Econ. Geol*. 96, 957–971.

Lawley, C. J. M., Dubé, B., Mercier-Langevin, P., Kjarsgaard, B., Knight, R., & Vaillancourt, D. (2015). Defining and mapping hydrothermal footprints at the BIF-hosted Meliadine gold district, Nunavut, Canada. *J. Geochem. Explor*. 155, 33–55.

Leitch, C. H. B., & Lentz, D. R. (1994). The Gresens approach to mass balance constrains of the alteration systems: Methods, pitfalls, examples. In Alteration and Alteration Processes Associated with Ore-Forming Systems; Ed.; *Geological Assocociation of Canada*: St. John's, NL, Canada, Volume 11, pp. 161–192.

Li, N. (2010). Textural and rule-based lithological classification of remote sensing Data, and geological mapping in Southwestern Prieska Subbasin, Transvaal Supergroup, South Africa. In: Thesis presented in at the *Faculty of Earth Sciences* the Ludwig Maximilian University of Munich, Germany, 155, 33–55.

Loughlin, W. P. (1991). Principal component analysis for alteration mapping. *Photogramm. Eng. Remote Sens*. 57, 1163–1169.

Macnae, J. C. (1979). Kimberlites and exploration geophysics *Geophysics* 44 1395–416

Maged, M. & Mazlan H. (2010). Lineament Mapping Using Multispectral Remote Sensing Satellite Data, *International Journal of the Physical Sciences* Vol. 5(10), pp. 1501-1507, 4 September, 2010.

Markham, B. L. & Helder, D. L. (2012). Forty-year calibrated record of earth-reflected radiance from Landsat: A review. *Remote Sensing of Environment,* 122, pp. 30–40

Markiewicz, R. D., Davenport, G. C., & Randall, J. A. (1984). The use of self-potential surveys in geotechnical investigations *54th Ann. Int. Meeting, Soc. Explor. Geophys., Expanded Abstr. (Soc. Explor. Geophys., Tulsa)* Session: SP6

Mars, J. L. (2013). Hydrothermal alteration maps of the central and southern basin and range province of the United States compiled from Advanced Spaceborne Thermal Emission and Reflection Radiometer (ASTER) data. *Cancer Genet.* 208, 364.

Mars, J.C. & Rowan, L.C. (2010). Spectral assessment of new ASTER SWIR surface reflectance data products for spectroscopic mapping of rocks and minerals. Remote Sens. Environ. 114, 2011–2025.

Masoud, A. A. & Koike, K. (2006). Tectonic architecture through LANDSAT-7 ETM+/SRTM DEM-derived lineaments and relationship to the hydrogeologic setting in Siwa Region, NW Egypt. *J. Afr. Earth Sci.* 45 (4–5), 467–477.

Masoud, A. A. & Koike, K. (2011_a). Auto-detection and integration of tectonically significant lineaments from SRTM DEM and remotely-sensed geophysical data. *ISPRS J. Photogramm. Remote Sens.* 66 (6), 818–832.

Masoud, A. A. & Koike, K. (2011_b). Morphotectonics inferred from the analysis of topographic lineaments auto-detected from DEMs: application and validation for the Sinai Peninsula, Egypt. *Tectonophysics* 510 (3–4), 291–308.

Masoumi, F., Eslamkish, T., Abkar, A. A., Honarmand, M., & Harris, J. R. (2017a). Integration of spectral, thermal, and textural features of ASTER data using random forests classification for lithological mapping. *J. Afr. Earth Sci.* 129, 445–457.

Masoumi, F., Eslamkish, T., Honarmand, M., & Abkar, A. A. (2017b). A comparative study of Landsat-7 and Landsat-8 data using image processing methods for hydrothermal alteration mapping. *Resour. Geol*, 67, 72–88.

Mateus, R., & Frutuoso, C. (2015). Mapping hydrothermal gold mineralization using Landsat 8 data. A case of study in Chaves license, Portugal, 25.

Mathew, T. G. & Ariffin K. S. (2018). Remote Sensing Technique for Lineament Extraction in Association with Mineralization Pattern in Central Belt Peninsular Malaysia, AMCIOP Conf. Series: *Journal of Physics*: Conf. Series1082, 012092.

Mathieu, L. (2016). Quantifying hydrothermal alteration with normative minerals and other chemical tools at the Beattie Syenite, Abitibi greenstone belt, Canada. *Geochem. Explor. Environ. Anal*. 16, 233–244.

Mathieu, L. (2018). Quantifying Hydrothermal Alteration: A Review of Methods. *Geosciences*, 8, 245; doi:10.3390/geosciences8070245

Meera, F. V. D., Christoph, H., Frank, R. V., Herald, W. V., Charlotte, W., & Caroline, W. (2014). Geologic remote sensing for geothermal exploration: A review. *International Journal of Applied Earth Observation and Geoinformation*, 33: p. 255–269.

Metelka, V., Baratoux, L., Jessell, M. W., Barth, A., Jezek, J., & Naba, S. (2018). Automated regolith landform mapping using airborne geophysics and remote sensing data, Burkina Faso, west Africa. *Remote Sens. Environ*, 204, 964–978.

Mia, M.B. & Fujimitsu, Y. (2012). Mapping hydrothermal altered mineral deposits using Landsat 7 ETM+ image in and around Kuju volcano, Kyushu, Japan, *Journal of Earth System Science, 121(4)*, 1049–1057.

Mike, A. (2005). JPL / NASA-GLCF, Airbus Defence and Space – Intelligence, Oil, Gas and Mining, Surface Geology for Mineral Exploration. michael.hall1@airbus.com.

Milbury, A. E. C., Smrekar, S. E., Raymond, C. A., & Schubert, G. (2007). Lithospheric structure in the east region of Mars'dichotomy boundary. *Planet. Space Sci*. 55 (3), 280–288.

Modabberi, S., Ahmadi, A., & Tangestani, M. H. (2017). Sub-pixel mapping of alunite and jarosite using ASTER data: a case study from north of Semnan, north central Iran, *Ore Geol. Rev*. 80. 429–436.

Mohamed, E., Saleh, A., Belal, A., & Gad, A. A. (2017). Application of near-infrared reflectance for quantitative assessment of soil properties. Egypt. *J. Remote Sens. Space Sci*. 237–246.

Molliex, S., Bellier, O., Terrier, M., Lamarche, J., Martelet, G., & Espurta, N. (2010). Tectonic and sedimentary inheritance on the structural framework of Provence (SE France): Importance of the Salon-Cavaillon fault. *Tectonophysics* 501, 1–16.

Moradi, M., Basiri, S., Kananian, A., & Kabiri, K. (2015). Fuzzy logic modeling for hydrothermal gold mineralization mapping using geochemical, geological, ASTER imageries and other geo-data, a case study in Central Alborz, Iran. *Earth Sci Inform*, 8, pp. 197-205

Morgan, V. (1989). Mass transfer and REE mobility during fenitization at Alno, Sweden. *Contrib. Mineral. Petrol*. 103, 25–34.

Moreels, P. & Smrekar, S. E. (2003). Watershed identification of Polygonal Patterns in Noisy SAR images, *IEEE Transactions on Image Processing*, 12, pp. 740-750

Mostafa, M. E. & Bishta, A. Z. (2005). Significance of lineament patterns in rock unit classification and designation: A pilot study on the Gharib-Dara area, northern Eastern Desert, Egypt. *Int. J. Remote Sens.* 26, 1463–1475.

Mwaniki, M. W., Moeller, M. S., & Schellmann, G. (2015). A comparison of Landsat 8 (OLI) and Landsat 7 (ETM+) in mapping geology and visualising lineaments: A case study of central region Kenya. *ISPRS - International Archives of the Photogrammetry, Remote Sensing and Spatial Information Sciences*, XL-7/W3, 897–903.

NASA, (2011). Goddard Space Flight Centre. Landsat 7 Science Data Users Handbook. Available online: http://landsathandbook.gsfc.nasa.gov/inst_cal/prog_sect8_2.html

Navarro, G., Caballero, I., Silva, G., Parra, P. C., Vázquez, Á., & Rui, C. (2017). Evaluation of forest fire on madeira island using Sentinel-2a MSI imagery. *Int. J. Appl. Earth Obs. Geoinf*. 58, 97–106.

Nguye, P. T. & Ho, D. (1988). Multiple source data processing in remote sensing, J. P. Muller, Ed, pp 153-176, *Taylor and Fransis*, Philadelphia, Pa, USA.

Ninomiya, Y. & Fu, B. (2016). Regional lithological mapping using ASTER-TIR data: Case study for the Tibetan Plateau and the surrounding area. *Geosciences* 6, 39.

Noori, L., Pour, B. A., Askari, G., Taghipour, N., Pradhan, B., Lee, C. W., & Honarmand, M. (2019). Comparison of different algorithms to map hydrothermal alteration zones using ASTER remote sensing data for polymetallic vein-type ore exploration: Toroud–Chahshirin Magmatic Belt (TCMB), North Iran. *Remote Sens*, 11, 495.

Nouri, R. (2015). Structural controls on the Distribution of Hydrothermal Alteration Zones and Mineralization in Dastjerdeh Area Based on Remote Sensing Data, NW Iran. Dept. of Geology, North Tehran Branch, Islamic University, Tehran, Iran Published by *Scientific Research*, 58, 97–106.

Nouri, R., Jafari, M. R., Arain, M., & Feizi, F. (2012). Hydrothermal Alteration Zones Identification based on Remote Sensing Data in the Mahin Area, West of Qazvin Province, Iran. *Journal of World Academy of Science, Engineering and Technology*, 6.

Nuhu, A. A. (2014). Heavy Metal Pollution: The Environmental Impact of Artisanal Gold Mining on Bagega Village of Zamfara State, Nigeria. *Research Journal of Pharmaceutical, Biological and Chemical Sciences* 5.6: 306-313.

Odumosu, J. O., Nwadialor, I. J., Alamba, D., Oluwatobi, O. A. (2022). Spectral Analysis of Lead Tailings in Top Soils. Tropical Journal of the Built Environment, 3 (2). Pgs 98 – 113.

Olasehinde, P. I. (1999). An Integrated Geologic and Geophysical Exploration Techniques for Groundwater in the Basement Complex of West Central Part Part of Nigeria. *Journal of Nigeria Association of Hydrogeologist* (Water Resources), 10 (1), 46-49.

O'Leary, D. W., Friedman, J. D., & Pohn, H. A. (1976). Lineament, linear, lineation: Some proposed new standards for old terms, *Geological Society America Bulletin*, Vol.87, 1463-1469.

Ombiro, S. O., Olatunji, A. S., Mathu, E. M., & Ajayi, T. R. (2021). Application of remote sensing in mapping hydrothermally altered zones in a highly vegetative area - A case study of Lolgorien, Narok County, Kenya. *Indian journal of science and technology* 14(9): 810-825.

Omer, E. A. H. & Zeinelabdein, K. A. E. (2018). Digital image processing of Landsat 8 and spectral analysis of ASTER data for mapping alteration minerals, Southern Hamisana, NE Sudan, *Al Neelain J. Geosci*. 2 (1) 10–20.

Perry, J. & Vincent, R. K. (2009). ASTER Brightness and Ratio Codes for Minerals: Application to Lithologic Mapping in the West-Central Power River Basin, Wyoming. *Reviews in Economic Geology*, v. 16, p. 143-168.

Pesaresi, M., Corbane, C., Julea, A., Florczyk, A. J., Syrris, V., & Soille, P. (2016). Assessment of the added-value of Sentinel-2 for detecting built-up areas. *Remote Sens.* 8, 299.

Phani, R. P. (2014). A GIS based correlation Between Lineaments and Gold occurrences of Ramagiri- Penakacherlaschist Belt, Eastern Dharwar Craton, India. *International Journal of Geology, Earth & Environmental Sciences* ISSN: 2277-2081

Phillips, G. N. & Powell, R. (2010). Formation of gold deposits: A metamorphic devolatilization model. J.Metamorph. *Geol*. 28, 689–718;

Pour, A., & Hashim, M., (2015). Hydrothermal alteration mapping from Landsat-8 data, Sar Chesmeh copper mining district, south-eastern Islamic Republic of Iran. *Journal of Taibah University for Science*, 9, 155-166.

Pour, A. B. & Hashim, M. (2011a). Application of advanced spaceborne thermal emission and reflection radiometer (ASTER) data in geological mapping. *International Journal of the Physical Sciences*, 33 (6): 7657-7668.

Pour, A. B. & Hashim, M. (2011b). Identification of hydrothermal alteration minerals for exploring of porphyry copper deposits using ASTER data, SE Iran. *Journal of Asian Earth Sciences*, 42: 1309-1323.

Pour, A. B. & Hashim, M. (2012a). The application of ASTER remote sensing data to porphyry copper and epithermal gold deposits. *Ore Geology Reviews*, 44: 1-19.

Pour, A. B. & Hashim, M. (2012b). Identifying areas of high economic-potential copper mineralisation using ASTER data in the Urumieh-Dokhtar Volcanic Belt, Iran. *Advances in Space Research*, 49: 753-769.

Pour, A. B. & Hashim, M. (2014). Structural geology mapping using PALSAR data in the Bau gold mining district, Sarawak, Malaysia. *Adv. Space Res.*54, 644–654.

Pour, A. B. & Hashim, M., (2011). Identification of hydrothermal alteration minerals for exploring of porphyry copper deposit using ASTER data, SE Iran. *J. Asian Earth Sci.* 42, 1309–1323.

Pour, A. B., Hashim, M. (2012). Identifying areas of high economic potential copper mineralization using ASTER data in the Urumieh- Dokhtar Volcanic Belt, Iran. *Adv. Sp. Res*. 49, 753–769.

Pour, A. B., Hashim, M., Hong, J. K., & Park, Y. (2019a). Lithological and alteration mineral mapping in poorly exposed lithologies using Landsat-8 and ASTER satellite data: North-eastern Graham Land, Antarctic Peninsula. *Ore Geol. Rev*., 108, 112–133.

Pour, A. B., Park, Y., Crispini, L., Läufer, A., Hong, J. K., Park, T. Y. S., Zoheir, B., Pradhan, B., Muslim, A. M., & Hossain, M. S. (2019b). Mapping listvenite occurrences in the damage zones of northern victoria land, Antarctica using ASTER Satellite Remote Sensing Data. *Remote Sens*, 11, 1408.

Pour, A. B., Park, Y., Park, T. S., Hong, J. K., Hashim, M., Woo, J., & Ayoobi, I. (2019c). Evaluation of ICA and CEM algorithms with Landsat-8/ASTER data for geological mapping in inaccessible regions. *Geocarto Int*., 34, 785–816.

Pournamdari, M., Hashim, M., & Pour, A. B. (2014). Application of ASTER and Landsat TM data for geological mapping of Esfandagheh ophiolite complex, southern Iran. Resour. *Geol.* 2014, 64, 233–246.

Putra, I. D., Nasution, R. A. F., & Harijoko, A. (2017). Aplikasi Landsat 8 OLI/TIRS dalam mengidentifikasi alterasi hidrotermal skala regional: studi kasus Daerah Rejang Lebong dan sekitarnya, Provinsi Bengkulu (Landsat 8 OLI/TIRS application in identifying regional scale hydrothermal alterations: A case study). Proseding Seminar Nasional Kebumian, 10, 1812-1826.

Rahnama, M. & Gloaguen, T. (2014). TecLines: A MATLAB-Based Toolbox for Tectonic Lineament Analysis from Satellite Images and DEMs, Part 1: Line Segment Detection and Extraction. *Remote Sensing,* 6: p. 5938-5958.

Rajesh, H. M. (2004). Application of remote sensing and GIS in mineral resource mapping – An overview. *Journal of Mineralogical and Petrological Sciences,* 99: 83-103.

Raju, P. & Kumar, K. (2020). Magnetic Survey for Iron-Oxide-Copper-Gold (IOCG) and Alkali Calcic Alteration Signatures in Gadarwara, M.P, India: Implications on Copper Metallogeny. *Minerals* 10, 671.

Ramadan, T. M. & Sultan, A. S. (2004). Integration of remote sensing, geological and geophysical data for the identification of massive sulphide zones at Wadi Allaqi area *Middle East J., Ain Shams Univ., Earth Sci. Ser.* 18 165–74

Ramli, M., Yusof, N., Yusoff, M., Juahir, H., & Shafri, H. (2010). Lineament mapping and its application in landslide hazard assessment: a review. *Bull. Eng. Geol. Environ*. 69, 215–233.

Rana, N., Chakravarthy, C. P., Nair, R., & Kannan, L. G. (2016). *Identification of lineaments using Google tools.* Recent Advances in Rock Engineering.

Rekhibi, S., Wadi, M., & Said, A. (2015). Remote Sensing & GIS Techniques for Gold Exploration. *Int'l Conf. on Advances in Science, Engg., Technology & Natural Resources (ICASETNR-15)* Aug. 27-28, Kota Kinabalu (Malaysia)

Richards, J. P. (2000). "Lineaments Revisited", *SEG newsletter*, 42, 14–21, 2000.

Rivard, B., Singhory, V., Cloutis, E., & Borstad, G. (2002). Canadian Hyperspectral Users and Science Team, Canadian Space Agency. User Requirements Report for Mineral Exploration

Rmdc, F. (2015). Mapping hydrothermal gold mineralization using Landsat 8 data. A case of study in Chaves license, Portugal. Portugal: Departamento de Geociências, Ambiente e Ordenamento do Território.

Rowland, J. V. & Sibson, R. H. (2004). Structural controls on hydrothermal flow in a segmented rift system, Taupo Volcanic Zone, New Zealand. *Geofluids* 4, 259–283.

RRSSC (2004). Remote sensing studies for gold exploration in parts of Bellary and Chitradurga districts (Sandur Block), Karnataka – Phase I & Phase II Activity. *Technical Report, Regional Remote Sensing Service Centre,* Nagpur, 38p.

Sabins, F. F. (1987). Remote sensing – Principles and Interpretation. *W.H. Freeman & Co.*, 2 edn., 449 p.

Sabins, F. (1997). Remote Sensing: *Principles and interpretation*, 2nd edn (New York, NY: Freeman).

Sabins, F. F. (1999). Remote sensing for mineral exploration. *Ore Geology Review* 14 (1999) 157–183.

Sadiya, T. B., Halilu, A. S., Asmah, T. F., Agu, N. V., Nsofor, C. J., Sanusi, M., Aliyu I., & Ibrahim, I. (2015). Hydrothermal Alteration Mapping in Ijio, Oyo State, Nigeria using Satellite Imagery & Remote Sensing Technique. *SSRG International Journal of Geo informatics and Geological Science* (SSRG-IJGGS) – volume 2 Issue 1, 1-8.

Said, A., Baby, P., Chardon, D., & Ouali, J. (2011). Structure, paleogeographic inheritance, and deformation history of the southern Atlas foreland fold and thrust belt of Tunisia. *Tectonics* 30.

Saliti, S., Van Ruitenbeek, F. J. A., Van der Meer, F. D., Tangestani, M. H., & Van der Werff, H. (2011). Lithological mapping and fuzzy set theory: Automated extraction of lithological boundary from ASTER imagery by template matching and spatial accuracy assessment. *International Journal of Applied Earth Observation and Geoinformation*, 13: 753-765.

San, Y., Sumer, E. O., & Gurcay, B. (2004). Comparison of Band ratioing and spectral indices methods for detecting alunite and kailinite minerals using ASTER data in Biga region, Turkey, Geo-Imagery Bridging Continents. *XXth ISPRS Congress*, Istanbul, Turkey.

Sarala, C. (2012). Identification of groundwater prospects for Palleru Sub Basin using remote sensing and GIS. *International Journal of Engineering Science and Advanced Technology*, 2012. 2(5): p. 1454 – 1460.

Scheiber, T., Fredin, O., Viola, G., Jarna, A., Gasser, D., & Lapinska-Viola. (2015). Manual extraction of bedrock lineaments from high-resolution LiDAR data: methodological bias and human perception. *GFF-Uppsala* -137(4):1-11.

Segal, D. B. (1983). Use of Landsat Multispectral Scanner Data for Definition of Limonitic Exposures in Heavily Vegetated Areas. *Econ. Geol.*, 78, pp. 711-722, EL Paso, Texas.

Shephard-Thorn, E. R., Lake, R. D., Atitullah, M. E., & Gray, D. A. (1972). Basement control of structures in the Mesozoic rocks in the Strait of Dover region, and its reflexion in certain features of the present land and submarine topography. *Phil. Trans. R. Soc. Lond.* A, 272, 99–110.

Sherman, D. M. & Waite, T. D. (1985). Electronic spectra of Fe3+ oxides and oxide-hydroxides in the near IR to near UV. Am. *Mineral* 70, 1262–1269.

Shin, H., Yu, J., Kim, J., Yang, D., & Lee, G. (2015). Mapping the moisture content of coastal sediments using aster data for spectroscopic and mineralogical analyses: A case study in South Korea. *IEEE Geosci. Remote Sens.* Lett. 6, 488–497.

Shin, J. H., Yu, J., Kim, S., Koh, S. M., & Park, G. (2016). Spectral characteristics of heavy metal contaminated soils in the vicinity of Boksu mine. *J. Miner. Soc. Korea* 29, 89–101.

Shippert, P. (2002). Introduction to hyperspectral image analysis. *Online Jour. Space Communication, Issue.No.3.* (http://satjournal.tcom.ohiou.edu/issue03).

Shirmard H., Farahbakhsh, E., Pour, A. B., Muslim, A. M., Müller, R. D., & Chandra, R. (2020) Integration of Selective Dimensionality Reduction Techniques for Mineral Exploration Using ASTER Satellite Data. *Remote Sens,* 12, 1261.

Sillitoe, R. H. (2010). Porphyry copper systems. *Econ. Geol.* 105, 3–41.

Singh, A. & Harrison, A. (1985). Standardized principal components. *Int. J. Remote Sens.* doi:10.1080/01431168508948511.

Smith, R.J. (2002). Geophysics of Iron Oxide Copper-Gold Deposits (Hydrothermal Iron Oxide Copper–Gold and Related Deposits: *A Global Perspective* vol 2) ed T M Porter (Adelaide: PGC Publishing) pp 357–67

Son, Y. S., Kang, M. K., & Yoon, W. J. (2014). Lithological and mineralogical survey of the Oyu Tolgoi region, southeastern Gobi, Mongolia using ASTER reflectance and emissivity data. *Int. J. Appl. Earth Obs. Geoinf.* 26, 205–216.

Song, L., Jian, J., Tan, D. J., Xie, H. B., Luo, Z. F., & Gao, B. (2015). Estimate of heavy metals in soil and streams using combined geochemistry and field spectroscopy in wan-sheng mining area, Chongqing, china. *Int. J. Appl. Earth Obs. Geoinf.* 34, 1–9.

Soto-Pinto, C., Arellano-Baeza, A., & Sánchez, G. (2013). A new code for automatic detection and analysis of the lineament patterns for geophysical and geological purposes (ADALGEO). *Comput. Geosci.* 57, 93–103.

Sternberg, B. K. & Oehler, D. Z. (1990). Induced polarization in hydrocarbon surveys: Arkoma basin case histories Induced Polarisation*: Applications and Case Histories* vol 4, ed S H Ward (USA: Society of Exploration Geophysicists)

Sukumarb, M., Venkatesan, N., & Babu, C. N. K. (2014). A Review of Various Lineament Detection techniques for high resolution images. *International Journal of Advanced Research in Computer Science and Software Engineering*, 4, 72-78.

Suzen, M. L. & Toprak, V. (2010). Filtering of satellite images in geological lineament analyses: An application to a fault zone in Central Turkey, *International Journal of Remote Sensing*, 19:6, 1101-1114, DOI: 10, 108/01424698215621.

Tangestani, M. H., Jaffari, L., Vincent, R. K., & Sridhar, B. M. (2011). Spectral characterization and ASTER-based lithological mapping of an ophiolite complex: A case study from Neyriz ophiolite, SWIran. *Remote Sens. Environ*. 115, 2243–2254.

Taoufik, M., Baghdad, B., El Hadi, H., & Laghlimi, M. (2016). Structural Interpretation of Lineaments by Remote Sensing and GIS using Landsat 8 Data: A Case Study of Akreuch Area (Morocco). *European Journal of Scientific Research* ISSN 1450-216X / 1450-202X Vol. 138 No 3, pp.216-224.

Taylor, R. G. (2011). Gossans and Leached Cappings. *Springer-Verlag, Berlin Heidelberg*, Pp146. ISBN 978-3-642-22050-0.

Thompson, A. J. B., Hauff, P. L., & Robitaille, A. J. (1999). Alteration mapping in exploration: Application of short wave infrared (SWIR) spectroscopy. *Soc. Econ. Geol. Newsl.* 1999, 30, 16–27.

Travaglia, C. & Dainelli, N. (2003). Groundwater Search by remote sensing: a methodological Approach, FAO, *Environment and Natural Resources service sustainable development department*, Rome, Italy. P 34.

Tripathi, N., Gokhale, K., & Siddiqu, M. (2000). Directional morphological image transforms for lineament extraction from remotely sensed images. *Int. J. Remote Sens*. 21, 3281–3292.

Ungar, S. G, Pearlman, J. S., Mendenhall, J. A., & Reuter, D. (2003). Overview of the Earth Observing One (EO-1) mission. *IEEE Transactions on Geoscience and Remote Sensing*, 41, 1149-1159

USGS, (2015a). *Landsat 8 (L8) Data Users Handbook*. Version 1.0, pp. 105

USGS, (2015b). *Using the USGS Landsat8 Product*: http://landsat.usgs.gov/Landsat8_Using_Product.php. Accessed Aug., 2015

USGS, (2015d). *Landsat Missions Timeline:* http://landsat.usgs.gov//about_mission_history.php. Accessed Aug., 2015

Van der Meer, F., Van der Werff, H. M. A., Van Ruitenbeek, J. A., Hecker, C. A., Bakker, W. H., Noomen, M. F., Van der Meijde, M., Carranza, J. M., de Smeth, B., & Woldai, T. (2012). Multi- and hyperspectral geologic remote sensing: An overview. *International Journal of Applied Earth Observation and Geoinformation*, 1 (14): 112-128.

Van der Meer, F., Van derWerff, H., & Van Ruitenbeek, F. (2014). Potential of ESA's Sentinel-2 for geological applications. *Remote Sens. Environ*. 2014, 148, 124–133.

Van der Werff, H. & Van der Meer, F. (2015). Sentinel-2 for mapping iron absorption feature parameters. *Remote Sens*. 7, 12635–12653.

Velasco, F., Herrero, J. M., Su´arez, S., Yusta, I., Alvaro, A., & Tornos, F. (2013). Supergene features and evolution of gossans capping massive sulphide deposits in the Iberian Pyrite Belt. *Ore Geol. Rev*. 53, 181–203. https://doi.org/10.1016/J.OREGEOREV.01.008.

Vural, A., Corumluoglu O., & Asri I. (2017) Remote Sensing Technique for Capturing and Exploration of Mineral Deposit Sites in Gümüshane Metallogenic Province, Ne

Turkey. *Journal of Geological Society of India*. 90 (5):625-633. (HYPERLINK "http://spiedl.aip.org/jhtml/doi.jsp" doi: 10.1007/s1259).

Walker, R. T. (2006). 'A Remote sensing study of active folding and faulting in southern Kerman province, southeast Iran'. *Journal of structural Geology*, vol. 28, no. 4 pp. 654-668.

Wang, J., Howarth, I. E. E. E., & Philip J. (1990). "Use of the Hough Transform in Automated Lineament Detection", *IEEE Transactions on Geoscience and Remote Sensing*, Vol. 28, No. 4, 561-566.

Warner, T. A. (1997). Integration of remotely sensed geobotanical and structural methods for hydrocarbon exploration in West-central West Virginia. *Final report for DOE sponsored Research Contract* DE-FG21-95MC32159. Morgantown, WV, 55pp.

Welch, R. & Ehlers, W. (1987). Merging multi-resolution SPOT HRV and Landsat TM Data. *Photogrammetric Engineering and Remote Sensing*. 53 (3) (1987) 301–303.

West, W. (2014). Absorption of Electromagnetic radiation, www.accessscience.com.

Witt, W. K. (1992). Porphyry intrusions and albitites in the Bardoc-Kalgoorlie area, Western Australia, and their role in Archean epigenetic gold mineralization. *Can. J. Earth Sci*. 1992, 29, 1609–1622.

Yesares, L., Aiglsperger, T., S´aez, R., Almod´ovar, G. R., Nieto, J. M., Proenza, J. A., G´omez, C., & Escobar, J.M. (2015). Gold Behavior in Supergene Profiles Under Changing Redox Conditions: The Example of the Las Cruces Deposit, Iberian Pyrite Belt. *Econ. Geol.* 110, 2109–2126. https://doi.org/10.2113/econgeo.110.8.2109.

Yousefi, S. J., Ranjbar, H., Alirezaei, S., Lentz, D. R., & Dargahi, S. (2018). Comparison of hydrothermal alteration patterns associated with porphyry Cu deposits hosted by granitoids and intermediate-mafic volcanic rocks, Kerman Magmatic Arc, Iran: application of geological, mineralogical and remote sensing data, *J. Afr. Earth Sci*. 142, 112–123.

Yu, L., Porwal, A., Holden, E. J., & Dentith, M. C. (2012). Towards automatic lithological classification from remote sensing data using support vector machines. *Comput. Geosci.* 45, 229–239.

Yungul, S. (1950). Interpretation of spontaneous polarization anomalies caused by spheroidal ore bodies *Geophysics* 15 237–46

Zeinelabdein, K. A. E., El-Nadi, A. H. H., & Babiker, I. S. (2020). Prospecting for gold mineralization with the use of remote sensing and GIS technology in North Kordofan State, central Sudan. *Scientific African* 10 e00627.

Zhang, X. & Li, P. (2014). Lithological mapping from hyperspectral data by improved use of spectral angle mapper. *Int. J. Appl. Earth Obs. Geoinf.* 31, 95–109.

Zhang, X., Pazner, M., & Duke, N. (2007). Lithologic and mineral information extraction for gold exploration using ASTER data in the south chocolate mountains (California). *ISPRS J. Photogramm. Remote Sens*. 2007, 62, 271–282.

Zhang, Y., Wang, B., Lin, G., Ouyang, Y., Wang, T., Xu, S., Song, L., & Wang, R. (2020). Three-Dimensional P-wave Velocity Structure of the Zhuxi Ore Deposit, South China Revealed by Control-Source First-Arrival Tomography. *Minerals* 10, 148.

Zhdanov, M. S., Alfouzan, F. A., Cox, L., Alotaibi, A., Alyousif, M., Sunwall, D., & Endo, M. (2018). Large-Scale 3D Modeling and Inversion of Multiphysics Airborne Geophysical Data: A Case Study from the Arabian Shield, Saudi Arabia. *Minerals* 8, 271.

Zoheir, B., El-Wahed, M. A., Pour, A. B., & Abdelnasser, A. (2012a). Orogenic gold in transpression and transtension zones: Field and remote sensing studies of the barramiya–mueilha sector, Egypt. *Remote Sens.*, 11, 2122.

Zoheir, B., Emam, A., Abdel-Wahed, M., & Soliman, N. (2012b). Multispectral and radar data for the setting of gold mineralization in the South Eastern Desert, Egypt. *Remote Sens.*, 11, 1450.

APPENDICES

APPENDIX A

Appendix A:

5_4_3 Landsat

Data file produced by Principal Components

Input raster(s):

#
C:\Users\user\Desktop\mymtechthesis\m.techimagery\FINALFINALIMAGERY\MAIGIRU_AREA.dat\Coastal aerosol (0.443000 Micrometers)

C:\Users\user\Desktop\my mtech thesis\m.tech imagery\FINAL FINAL IMAGERY\MAIGIRU_AREA.dat\Blue (0.482600 Micrometers)

C:\Users\user\Desktop\my mtech thesis\m.tech imagery\FINAL FINAL IMAGERY\MAIGIRU_AREA.dat\Green (0.561300 Micrometers)

C:\Users\user\Desktop\my mtech thesis\m.tech imagery\FINAL FINAL IMAGERY\MAIGIRU_AREA.dat\Red (0.654600 Micrometers)

C:\Users\user\Desktop\my mtech thesis\m.tech imagery\FINAL FINAL IMAGERY\MAIGIRU_AREA.dat\Near Infrared (NIR) (0.864600 Micrometers)

C:\Users\user\Desktop\my mtech thesis\m.tech imagery\FINAL FINAL IMAGERY\MAIGIRU_AREA.dat\SWIR 1 (1.609000 Micrometers)

C:\Users\user\Desktop\my mtech thesis\m.tech imagery\FINAL FINAL IMAGERY\MAIGIRU_AREA.dat\SWIR 2 (2.201000 Micrometers)

C:\Users\user\Desktop\my mtech thesis\m.tech imagery\FINAL FINAL IMAGERY\MAIGIRU_AREA.dat\Coastal aerosol (0.443000 Micrometers)

C:\Users\user\Desktop\my mtech thesis\m.tech imagery\FINAL FINAL IMAGERY\MAIGIRU_AREA.dat\Blue (0.482600 Micrometers)

C:\Users\user\Desktop\my mtech thesis\m.tech imagery\FINAL FINAL IMAGERY\MAIGIRU_AREA.dat\Green (0.561300 Micrometers)

C:\Users\user\Desktop\my mtech thesis\m.tech imagery\FINAL FINAL IMAGERY\MAIGIRU_AREA.dat\Red (0.654600 Micrometers)

C:\Users\user\Desktop\my mtech thesis\m.tech imagery\FINAL FINAL IMAGERY\MAIGIRU_AREA.dat\Near Infrared (NIR) (0.864600 Micrometers)

C:\Users\user\Desktop\my mtech thesis\m.tech imagery\FINAL FINAL IMAGERY\MAIGIRU_AREA.dat\SWIR 1 (1.609000 Micrometers)

C:\Users\user\Desktop\my mtech thesis\m.tech imagery\FINAL FINAL IMAGERY\MAIGIRU_AREA.dat\SWIR 2 (2.201000 Micrometers)

C:\Users\user\Desktop\my mtech thesis\m.tech imagery\FINAL FINAL IMAGERY\MAIGIRU_AREA.dat\Coastal aerosol (0.443000 Micrometers)

C:\Users\user\Desktop\my mtech thesis\m.tech imagery\FINAL FINAL IMAGERY\MAIGIRU_AREA.dat\Blue (0.482600 Micrometers)

C:\Users\user\Desktop\my mtech thesis\m.tech imagery\FINAL FINAL IMAGERY\MAIGIRU_AREA.dat\Green (0.561300 Micrometers)

C:\Users\user\Desktop\my mtech thesis\m.tech imagery\FINAL FINAL IMAGERY\MAIGIRU_AREA.dat\Red (0.654600 Micrometers)

C:\Users\user\Desktop\my mtech thesis\m.tech imagery\FINAL FINAL IMAGERY\MAIGIRU_AREA.dat\Near Infrared (NIR) (0.864600 Micrometers)

C:\Users\user\Desktop\my mtech thesis\m.tech imagery\FINAL FINAL IMAGERY\MAIGIRU_AREA.dat\SWIR 1 (1.609000 Micrometers)

C:\Users\user\Desktop\my mtech thesis\m.tech imagery\FINAL FINAL IMAGERY\MAIGIRU_AREA.dat\SWIR 2 (2.201000 Micrometers)

The number of components = 21

Output raster(s):

C:\Users\user\Desktop\my mtech thesis\m.tech imagery\FINAL FINAL IMAGERY\543LANDSA

APPENDIX B:

Appendix Bi:

7_5_2 LANDSAT

Data file produced by Principal Components

Input raster(s):

C:\Users\user\Desktop\my mtech thesis\m.tech imagery\FINAL FINAL IMAGERY\MAIGIRU_AREA.dat\Coastal aerosol (0.443000 Micrometers)

C:\Users\user\Desktop\my mtech thesis\m.tech imagery\FINAL FINAL IMAGERY\MAIGIRU_AREA.dat\Blue (0.482600 Micrometers)

C:\Users\user\Desktop\my mtech thesis\m.tech imagery\FINAL FINAL IMAGERY\MAIGIRU_AREA.dat\Green (0.561300 Micrometers)

C:\Users\user\Desktop\my mtech thesis\m.tech imagery\FINAL FINAL IMAGERY\MAIGIRU_AREA.dat\Red (0.654600 Micrometers)

C:\Users\user\Desktop\my mtech thesis\m.tech imagery\FINAL FINAL IMAGERY\MAIGIRU_AREA.dat\Near Infrared (NIR) (0.864600 Micrometers)

C:\Users\user\Desktop\my mtech thesis\m.tech imagery\FINAL FINAL IMAGERY\MAIGIRU_AREA.dat\SWIR 1 (1.609000 Micrometers)

C:\Users\user\Desktop\my mtech thesis\m.tech imagery\FINAL FINAL IMAGERY\MAIGIRU_AREA.dat\SWIR 2 (2.201000 Micrometers)

C:\Users\user\Desktop\my mtech thesis\m.tech imagery\FINAL FINAL IMAGERY\MAIGIRU_AREA.dat\Coastal aerosol (0.443000 Micrometers)

C:\Users\user\Desktop\my mtech thesis\m.tech imagery\FINAL FINAL IMAGERY\MAIGIRU_AREA.dat\Blue (0.482600 Micrometers)

C:\Users\user\Desktop\my mtech thesis\m.tech imagery\FINAL FINAL IMAGERY\MAIGIRU_AREA.dat\Green (0.561300 Micrometers)

C:\Users\user\Desktop\my mtech thesis\m.tech imagery\FINAL FINAL IMAGERY\MAIGIRU_AREA.dat\Red (0.654600 Micrometers)

C:\Users\user\Desktop\my mtech thesis\m.tech imagery\FINAL FINAL IMAGERY\MAIGIRU_AREA.dat\Near Infrared (NIR) (0.864600 Micrometers)

C:\Users\user\Desktop\my mtech thesis\m.tech imagery\FINAL FINAL IMAGERY\MAIGIRU_AREA.dat\SWIR 1 (1.609000 Micrometers)

C:\Users\user\Desktop\my mtech thesis\m.tech imagery\FINAL FINAL IMAGERY\MAIGIRU_AREA.dat\SWIR 2 (2.201000 Micrometers)

C:\Users\user\Desktop\my mtech thesis\m.tech imagery\FINAL FINAL IMAGERY\MAIGIRU_AREA.dat\Coastal aerosol (0.443000 Micrometers)

C:\Users\user\Desktop\my mtech thesis\m.tech imagery\FINAL FINAL IMAGERY\MAIGIRU_AREA.dat\Blue (0.482600 Micrometers)

C:\Users\user\Desktop\my mtech thesis\m.tech imagery\FINAL FINAL IMAGERY\MAIGIRU_AREA.dat\Green (0.561300 Micrometers)

C:\Users\user\Desktop\my mtech thesis\m.tech imagery\FINAL FINAL IMAGERY\MAIGIRU_AREA.dat\Red (0.654600 Micrometers)

C:\Users\user\Desktop\my mtech thesis\m.tech imagery\FINAL FINAL IMAGERY\MAIGIRU_AREA.dat\Near Infrared (NIR) (0.864600 Micrometers)

C:\Users\user\Desktop\my mtech thesis\m.tech imagery\FINAL FINAL IMAGERY\MAIGIRU_AREA.dat\SWIR 1 (1.609000 Micrometers)

C:\Users\user\Desktop\my mtech thesis\m.tech imagery\FINAL FINAL IMAGERY\MAIGIRU_AREA.dat\SWIR 2 (2.201000 Micrometers)

The number of components = 21

Output raster(s):

C:\Users\user\Desktop\my mtech thesis\m.tech imagery\FINAL FINAL IMAGERY\LATEST PCA\752LANSAT

APPENDIX C

Appendix Ci:

KAUFMANN LANDSAT PCA

Data file produced by Principal Components

Input raster(s):

C:\Users\user\Desktop\my mtech thesis\m.tech imagery\FINAL FINAL IMAGERY\bands for pca in arcgis\7_5_landsat\Ratio (SWIR 2 (2.2010):MAIGIRU_AREA.dat / Near Infrared (NIR) (0.8646):MAIGIRU_AREA.dat)

C:\Users\user\Desktop\my mtech thesis\m.tech imagery\FINAL FINAL IMAGERY\bands for pca in arcgis\5_4_landat\Ratio (Near Infrared (NIR) (0.8646):MAIGIRU_AREA.dat / Red (0.6546):MAIGIRU_AREA.dat)

C:\Users\user\Desktop\my mtech thesis\m.tech imagery\FINAL FINAL IMAGERY\bands for pca in arcgis\6_7_landsat\Ratio (SWIR 1 (1.6090):MAIGIRU_AREA.dat / SWIR 2 (2.2010):MAIGIRU_AREA.dat)

The number of components = 3

Output raster(s):

C:\Users\user\Documents\ArcGIS\Default.gdb\Princip_9

APPENDIX D

Appendix Di:

Sabins Landsat PCA

Data file produced by Principal Components

Input raster(s):

C:\Users\user\Desktop\my mtech thesis\m.tech imagery\FINAL FINAL IMAGERY\bands for pca in arcgis\4_2_landsat\Ratio (Red (0.6546):MAIGIRU_AREA.dat / Blue (0.4826):MAIGIRU_AREA.dat)

C:\Users\user\Desktop\my mtech thesis\m.tech imagery\FINAL FINAL IMAGERY\bands for pca in arcgis\6_7_landsat\Ratio (SWIR 1 (1.6090):MAIGIRU_AREA.dat / SWIR 2 (2.2010):MAIGIRU_AREA.dat)

C:\Users\user\Desktop\my mtech thesis\m.tech imagery\FINAL FINAL IMAGERY\bands for pca in arcgis\6_5_landsat\Ratio (SWIR 1 (1.6090):MAIGIRU_AREA.dat / Near Infrared (NIR) (0.8646):MAIGIRU_AREA.dat)

The number of components = 3

Output raster(s):

C:\Users\user\Documents\ArcGIS\Default.gdb\Princip_8